7-18-2017 12:00 AM

Using Bolide Airwaves To Estimate Meteoroid Source Characteristics And Window Damage Potential

Nayeob Gi, *The University of Western Ontario*

Supervisor: Dr. Peter Brown, *The University of Western Ontario*
A thesis submitted in partial fulfillment of the requirements for the Master of Science degree in Geophysics

Recommended Citation

Gi, Nayeob, "Using Bolide Airwaves To Estimate Meteoroid Source Characteristics And Window Damage Potential" (2017). *Electronic Thesis and Dissertation Repository*. 4688.
https://ir.lib.uwo.ca/etd/4688

Abstract

We examined the far-field infrasonic signals produced by 78 bolides simultaneously detected by U.S. government sensors to determine the mechanisms responsible for interstation spreads in infrasound signal period. These signal period spreads lead to large variances in source energy estimates. Our analysis suggests that while acoustic source height contributes to some extent to the variance in signal periods, the range from the source to the station and in particular station noise plays a more significant role.

By simulating the near-field weak shocks from a suite of well-observed energetic fireballs, we have empirically estimated how often fireball shocks produce overpressure (ΔP) at the ground sufficient to damage windows. Our study suggests that the effective threshold energy for fireballs to produce heavy window damage (where standard windows would have a breakage probability between 0.4 - 7%) corresponding to $\Delta P > 500$ Pa is ~5 - 10 kilotons (kT) of TNT equivalent (where 1 kT is 4.185×10^{12} J). Such fireballs occur globally once every one to two years. The expected frequency of bolide shock waves producing heavy window damage in urban areas is once every ~5000 years. Similarly, we find that light window damage (where standard windows would have a breakage probability between 0.01 - 0.7%) for $\Delta P > 200$ Pa is expected every ~600 years. Hence the largest annual bolide events, should they occur over a major urban centre with a large number of windows, can be expected to produce economically significant window damage.

Keywords: bolide, flux, yield, infrasound, ablation, airblasts, shock waves

Co-Authorship Statement

This thesis dissertation is prepared in integrated article format based on the following two papers that are either published or submitted in a peer-reviewed journal:

Chapter 3: Gi, N. and Brown, P. (2017) Refinement of Bolide Characteristics from Infrasound measurements, *Planetary and Space Science*. 143:169-181. doi:10.1016/j.pss.2017.04.021.

Chapter 4: Gi, N. and Brown, P. (2017) The frequency of window damage caused by bolide airbursts, *Meteoritic & Planetary Science* (submitted).

The thesis and composed papers were completed under the supervision of Dr. Peter Brown. I generated the global bolide infrasound database, performed the infrasound signal measurements used in the data analysis of Chapter 3. I implemented the raytracing and weak shock model discussed in Chapter 3 and the TPFM model discussed in Chapter 4. Dr. Brown provided ongoing guidance, suggestions, and improvements to the manuscripts and assisted with manuscript revisions.

Acknowledgments

I would like to express my sincere gratitude and appreciation to my supervisor, Dr. Peter Brown for providing me with guidance, advice, and support throughout the course of my research work. I was very fortunate to join the Western Meteor Physics Group and to work under his supervision as he is very passionate, knowledgeable and caring. The knowledge and experience I gained during the two years of my Master's program will greatly benefit my future.

I thank all past and present Meteor Physics Group members for their help and valuable advice. A special thanks to Dr. Elizabeth Silber and (soon to be Dr.) Dilini Subasinghe who helped me to solve many problems that I faced during this research.

Also I would like to thank the administrative staff in the Department of Earth Sciences and the Department of Physics and Astronomy for their help.

I would like to express my appreciation to Dr.Valentina Radic at the University of British Columbia, with whom I first started my research career, and to Dr. William Ward at University of New Brunswick who gave me an opportunity to continue my research journey, for their immense roles in developing my knowledge and research skills.

My gratitude also goes to Natural Resources Canada, the Canada Research Chair program and the Natural Sciences and Engineering Research Council of Canada for financially supporting this research. This work was also supported through NASA co-operative agreement NNX15AC94A .

Last but not least, I thank my family for all of their love, encouragement and support.

Contents

List of Figures

List of Tables

List of Appendices

Chapter 1

Introduction

1.1 Meteor Physics

1.1.1 Basic Background

Objects having orbits close to that of the Earth (perihelion distances $q < 1.3$ AU) are called near-Earth objects (NEOs). An NEO is categorized as a potentially hazardous asteroid (PHA) for Earth when its minimum orbit intersection distance (distance between the closest points of the osculating orbits of two objects) is less than 0.05 AU and it has an absolute magnitude (H) of 22 or less (i.e. mean diameter > 140 m). NEOs represent a critical subject of planetary research as they can provide crucial information regarding the formation and early evolution of the solar system, the orbital evolution of asteroids and comets, and they are valuable in quantifying the frequency of impacts to the Earth.

As of June 2017, the cumulative number of known NEOs is about 15,000 and there are about 2,000 PHAs (JPL CNEOS[1]). Over 90% of NEOs larger than one kilometer have been discovered, however the actual number of small (meter-decameter) sized objects is not well-known.

On February 15, 2013, a small (about 20 meters in diameter) sized asteroid impacted the

---

[1] https://cneos.jpl.nasa.gov/stats/

Earth over Chelyabinsk, Russia (Brown et al., 2013). With a total impact energy equivalent to 500 kT of TNT (1 kT = 4.184×10^{12} J), this event was the largest impact recorded since the 1908 Tunguska event (Borovička et al., 2013; Brown et al., 2013; Popova et al., 2013). As a result of the fireball shock wave, over one thousand people were injured and several thousand buildings were damaged (Popova et al., 2013). This incident emphasized that small NEOs can produce significant damage on a local scale and focused public attention on the potential hazards of small NEO impacts with Earth.

One way of understanding the NEO population and measuring both the number of such objects and their physical characteristics is by detecting them when they hit the atmosphere. It is estimated that a 1 m diameter NEO collides with the Earth every two weeks, while a 4 m diameter object hits the Earth roughly once per year (Brown et al., 2002). Such an object ablates in the Earth's atmosphere, and produces a meteor.

More specifically, this interaction with the Earth's atmosphere excites and ionizes the meteoric atoms which create a plasma that surrounds the original body. As the electrons drop back into a lower energy ground state, photons are released forming the luminous phenomenon referred to as a meteor (Borovička et al., 2015). A bolide or fireball is an extremely bright meteor, brighter than that of the planet Venus which has an astronomical magnitude -4 (Borovička et al., 2015; Ceplecha et al., 1998). The brightest stars in the sky have astronomical magnitudes of -2, while the faintest stars visible to the naked eye from a dark site are close to +6.

If cameras on the ground can detect the meteor optically, its orbit and atmospheric fragmentation behaviour can be reconstructed and much may be learned about the internal structure of the original meteoroid (e.g. Borovička et al. 2015). Similarly, if radar detects the ionization trail left by the meteoroid, details of the orbit and original object may be inferred (Ceplecha et al., 1998).

However, for rare, comparatively large objects (a meter and larger) which hit the Earth only a few times per year, the vast majority burn up over oceans or uninhabited areas so it is very rare that any ground-based optical or radar registrations of such events are secured. In contrast, the shock waves universally produced by the passage of these large objects may be detected over global-scale distances. As a result, a significant fraction of all such large NEOs impacting the Earth are detectable by high sensitivity, low frequency microphones (called microbarometers).

While such low frequency sound (called infrasound) signals from bolides contain less information about the impact than optical or radar measurements, the impact location and impact energy have been estimated from infrasound bolide records in the past (Ens et al., 2012).

In this thesis, I focus on three main questions:

1. Can other characteristics of the NEO impact, such as its disintegration height, entry angle, and speed be inferred from the far-field attenuated shock waves of such impacts?

2. What is the underlying cause of the interstation variation in infrasound signal period which leads to large variability in energy estimates for bolide (and other atmospheric) explosions?

3. How often do the near-field shocks from NEOs produce overpressures large enough to just barely cause damage at the ground (i.e. break windows)?

1.1.2 The Physics of Meteoroid Entry

As defined by the International Astronomical Union in 2017, meteoroids are objects travelling in space with sizes roughly between 30 μm and 1 m. Objects larger than 1 m are typically asteroidal in origin, but the size and nomenclature cutoff remain somewhat vague. I refer to any object hitting the Earth as a meteoroid, such objects having been near-Earth objects prior to impact as they orbit the sun.

Meteoroids or NEOs on closed orbits around the sun can impact Earth with velocities between 11 and 72 km/s. As they enter the Earth's atmosphere, they decelerate and start to heat up due to high-energy collisions with atmospheric molecules. The motion (deceleration) of the meteoroid is described as (Ceplecha et al., 1998):

$$\frac{dv}{dt} = -\frac{\Gamma A_s \rho_a v^2}{m^{1/3} \rho_m^{2/3}}, \tag{1.1}$$

where

$$A_s = S m^{-2/3} \rho_m^{2/3} \tag{1.2}$$

is the dimensionless shape factor (A_s=1.21 for a sphere), S is the frontal cross-sectional area of the meteoroid (m^2), m is the initial mass of the meteoroid (kg), ρ_m is the density of the meteoroid (kg/m^3), ρ_a is the atmospheric density (kg/m^3), v is the initial velocity of the meteoroid (m/s), t is the time (s), and Γ is the drag coefficient (the fraction of momentum transferred to the meteoroid from the oncoming air molecules). The hypersonic passage through the atmosphere creates immense pressure, as the body loses its kinetic energy both from atmospheric drag and mass loss due to aerodynamic heating. Eq. 1.1 represents Newton's second law ($F = ma$) which expresses conservation of momentum.

As the body collides with air particles, it will lose mdv/dt units of momentum per second while the air particles gain $\Gamma vdm/dt$ units of momentum per second. Here, $dm = A(m/p_m)^{2/3} p_a vdt$ which is the mass of air intercepted by the body. Equating the momentum loss by the body and the momentum gained by the air particles yields the deceleration equation (Eq. 1.1).

Due to the collisions with air particles, the kinetic energy of the meteoroid is converted to heating the atmosphere, light and shock production, meteoroid ablation, dissociation and ionization. Fig. 1.1 is an example of energy partitioning showing the total power balance as a function of time for the Neuschwanstein meteorite fall (ReVelle, 2005). Once the compressive stresses induced by the high aerodynamic pressures on the body exceed its yield strength, the body begins to rapidly fragment. The aerodynamic heating results in melting, vaporization and a high rate of ablation. The rate of mass loss is assumed to be proportional to the kinetic energy transferred to the intercepted air mass. Thus, the conservation of kinetic energy also known as the ablation (mass-loss) equation of a meteoroid is expressed as

$$\frac{dm}{dt} = -\frac{\Lambda A_s \rho_a v^3 m^{2/3}}{2\xi \rho_m^{2/3}}, \tag{1.3}$$

where Λ is the heat transfer coefficient and ξ is the ablation energy of the meteoroid (the energy required to melt/vaporize one unit of meteoroid mass dm).

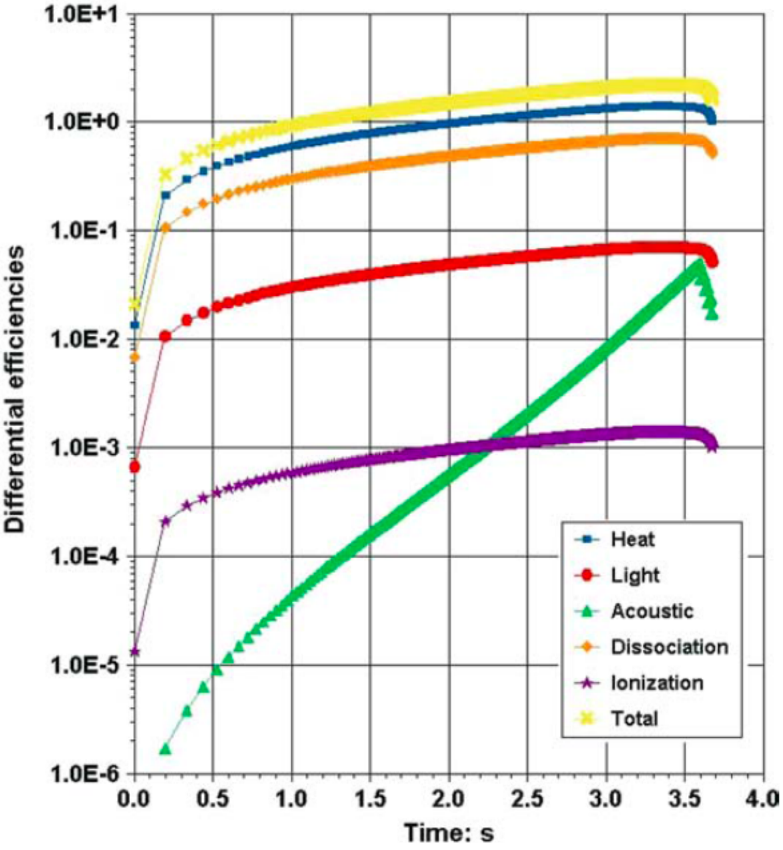

Figure 1.1: Total power balance as a function of time for the entry of the Neuschwanstein meteorite fall. The power balance was computed in a panchromatic band (~360 - 675 nm) (from ReVelle, 2005).

The deceleration (Eq. 1.1) and mass-loss (Eq. 1.3) equations are fundamental kinematic equations that describe how a body moves through the atmosphere. These two basic differential equations are sometimes called the "single body theory" which assumes a single non-fragmenting body moving through the atmosphere with a linear trajectory and ballistic entry neglecting lift forces and gravity (Ceplecha et al., 1998).

In general, it is assumed that the luminosity associated with a meteor is proportional to the loss of meteoroid kinetic energy. Thus, the luminosity, I, of the meteor can be defined as (Ceplecha et al., 1998):

$$I = \tau \frac{dE_k}{dt}, \tag{1.4}$$

where E_k is the meteoroid kinetic energy and τ is the luminous efficiency, the fraction of the total initial kinetic energy converted to light. A more general form is given by:

$$I = -\tau \left(\frac{v^2}{2} \frac{dm}{dt} + mv \frac{dv}{dt} \right), \tag{1.5}$$

where v is the velocity (m/s), m is the mass (kg), and t is the time (s).

The meteor's light curve, the observed luminosity of the meteor as a function of time, can be converted to an equivalent energy deposition curve (see Appendix B section B.3) which is the key parameter needed to determine the size of the shock wave blast cavity (called blast radius). As a meteoroid travels through the atmosphere, it produces a hypersonic shock and its geometry is well-approximated by a cylindrical shape. The blast radius is the radius of the cylindrical explosive line source, labelled as R_o in Fig. 1.2.

The blast radius (R_o) is the distance away from the meteoroid trajectory in the atmosphere to the point where the ambient atmospheric pressure equals the shock overpressure (Tsikulin, 1970). Physically, R_o represents the zone of highly nonlinear wave propagation where the atmosphere is very strongly shocked by the meteoroid's passage, and is defined as:

$$R_o = \left(\frac{E_o}{P_o} \right)^{\frac{1}{2}}, \tag{1.6}$$

where E_o is the total energy per unit trail length (J/m) and P_o is the ambient hydrostatic atmospheric pressure (Pa). For non-fragmenting meteors, R_o is directly related the atmospheric drag force so it can be also expressed as a product of Mach number and the meteoroid diameter

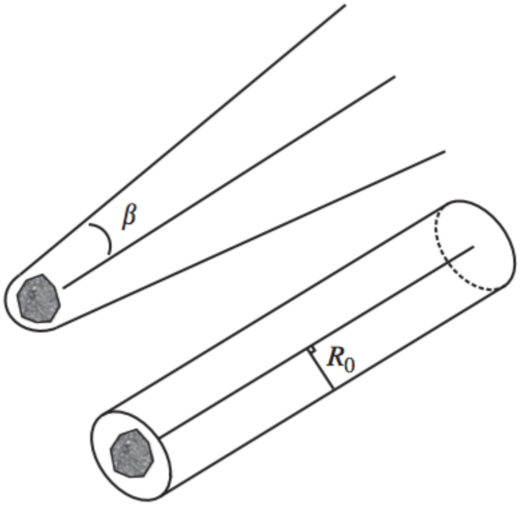

Figure 1.2: A diagram depicting the ballistic shock cone of the meteoroid (top). The geometry of the hypersonic ballistic shock of a meteor is well-approximated by a cylinder with blast radius (R_o) (bottom). The cylindrical line source is valid only if an object is travelling at much greater speeds (11 - 72 km/s) than the speed of sound (the angle β has to be very small) (from Ens et al., 2012).

(ReVelle, 1976):

$$R_o \approx M d_m, \tag{1.7}$$

where $M = v/C_s$, v is the speed of meteoroid (m/s) and C_s is the local ambient thermodynamic speed of sound (m/s).

As a meteor's shock wave propagates outward, it undergoes several transition. The propagation starts as a highly nonlinear shock with a large overpressure (ratio of the shock pressure amplitude to the ambient atmospheric pressure) during which time the shock wave propagates faster than the local speed of sound. After it has travelled several R_o distances, the wave propagates as a weakly nonlinear shock, where its speed is very close to, but slightly larger than, the ambient speed of sound.

According to ReVelle (1976), the shock wave reaches the fundamental wave frequency f_o (at maximum amplitude) after it has travelled a distance of $10R_o$. The fundamental period (τ_o)

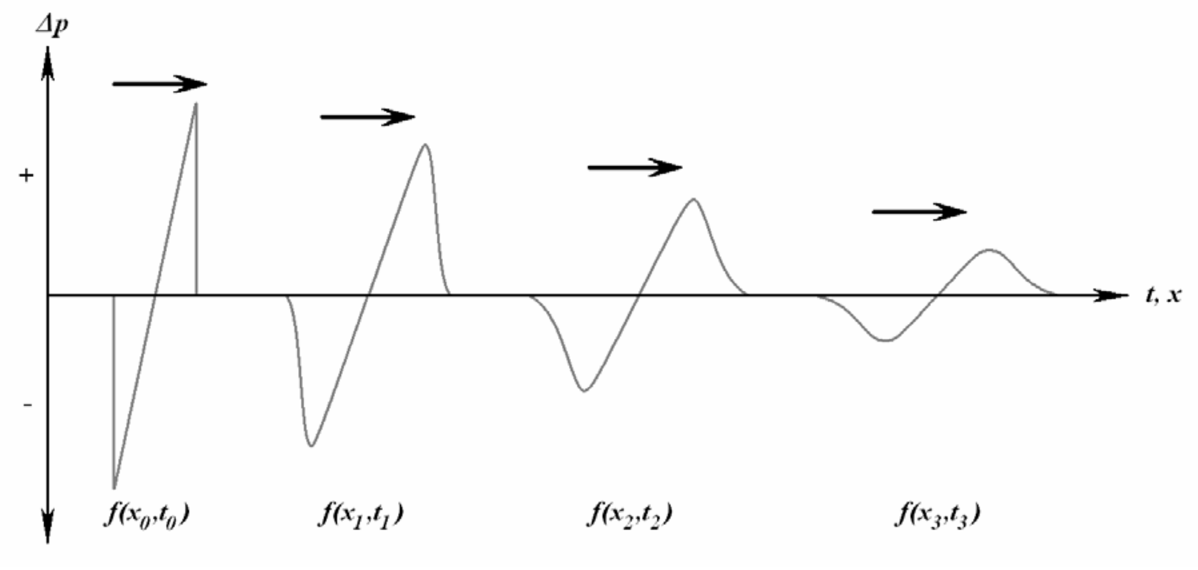

Figure 1.3: Modification of a shock wave from initial highly nonlinear ballistic shock. As the shock propagates, the amplitude decreases. The sharp wave front is rounded as the dispersion gradually increases the period (from Edwards, 2010).

is defined by inverting the fundamental frequency (f_o):

$$\tau_o = \frac{1}{f_o} = \frac{2.81R_o}{C_s} \tag{1.8}$$

These relations of the meteor blast radius, fundamental frequency and period clearly show that faster and/or larger meteoroids produce larger blast radii resulting in longer fundamental periods and lower frequencies. In the regime of $10R_o$, the overpressure is still large enough to cause significant wave attenuation. As the wave amplitude decreases, dispersion modifies the wavefront and the period increases as shown in Fig. 1.3.

Once the amplitude is sufficiently decreased, the wave propagation eventually transitions into a linear perturbation as an infrasonic wave. This wave may be detectable at large distances from the source using sensitive microbarometers which can measure low frequency pressure changes in the atmosphere at the level of one part in a billion of the ambient atmospheric pressure.

1.1.3 Bolide Ablation Entry Models

While the previous section outlines the basic physics of meteoroid interaction with the atmosphere, in practice applying these equations to real events is more complex. Many ablation models have been developed to predict the entry behaviour of meteoroids as they ablate within the Earth's atmosphere. Both analytical models (Chyba et al., 1993; Hills and Goda, 1993, 1998; Collins et al., 2005) and numerical hydrocodes (Boslough and Crawford, 1997; Shuvalov and Trubetskaya, 2007) have been applied to simulate in detail the entry, deformation, fragmentation and subsequent energy deposition of a hypothetical meteoroid.

Numerical entry models using detailed estimates of meteoroid strength and shock production also exist to model atmospheric energy deposition (Shuvalov et al., 2017). A recent validation focus for these models is computing the model energy deposition curve and comparing the results to the observationally derived energy deposition curve for the Chelyabinsk event. In most cases these show good agreement validating the use of these models (Avramenko et al., 2014; Shuvalov et al., 2013; Register et al., 2017; Robertson and Mathias, 2017; Collins et al., 2017).

In our work, we use a semi-analytic bolide ablation model first developed by ReVelle (1979) which predicts the ablation parameter, $\sigma = C_H/C_D Q$ where C_H is the heat transfer coefficient, C_D is the effective coefficient of wave drag and Q is the heat of ablation, for a given meteoroid. The model is based on integrating the equations of motion and mass-loss analytically, which yield relations between velocity and mass with height. The model determines physical parameters related to meteoroid ablation and fragmentation behaviour in real atmospheric profiles and generates the meteoroid light curve as a function of height. The model input parameters include initial bolide radius (m), mass (kg), velocity (m/s), bulk density (kg/m^3), and entry angle (°).

The model has developed over several decades (ReVelle, 1979, 2001, 2002). The major modification in recent years was adding the effects of shape change factor, μ. For a sphere which has a self-similar ablation into a smaller sphere with no shape change, $\mu = 2/3$ (an upper limit of μ). For $0 \leq \mu < 2/3$, the body experiences ablation and deceleration, and the frontal cross sectional area (S) decreases with decreasing height. In the case where a meteoroid is rapidly fragmented and crushed resulting in a catastrophic "pancake" fragmentation, S increases with decreasing height and $\mu < 0$. In general, the shape change factor, μ, cannot be calculated, other than using detailed numerical models. The model allows for ablation and deceleration and calculates the meteoroid blast radius as a function of height. More comprehensive details on the methodology and assumptions of this entry modeling can be found in ReVelle (1976, 1979, 2001, 2002, 2005).

Following ReVelle (2005), we used the analytic Triggered Progressive Fragmentation Model (TPFM), as the modern version of this ablation procedure is termed, which allows explicit inclusion of a simple fragmentation model once the tensile strength of an object is exceeded to simulate energy deposition and ablation. The model input parameters include initial speed (km/s), entry angle (°), initial energy (kT), porosity, strength (MPa), number of fragments, and increment in fragment strength. Many of these parameters are unknown, thus in our approach they are chosen from broader distributions in a Monte Carlo sense. I use the TPFM model to generate a range of predicted light curves which provide equivalent energy deposition profiles. From these, we calculated the blast radius (R_o) using the fundamental definition in terms of energy deposition per unit trail length. This was then used as an input for a weak shock model to determine the predicted overpressures (pressure caused by a shock wave) on the ground to gauge blast damage as an approach to addressing our third fundamental question for this thesis. Further details on the TPFM model can be found in Chapter 4.

1.2 Infrasound

1.2.1 Infrasound Characteristics and Propagation

In general, sound is a longitudinal pressure wave which propagates in the same direction as the source particle or oscillator motion. Sound waves in the atmosphere within the range of 20

- 20,000 Hz are audible to humans. Frequencies higher than 20,000 Hz, which are inaudible to humans, are called ultrasound. Sound waves below 20 Hz, are referred to as infrasound. The lower limit of infrasound is bounded by the natural buoyancy frequency of the atmosphere (Brunt-Väisälä frequency).

Infrasound is generated by a wide range of natural and artificial sources (Fig. 1.4[2]) and travels at the speed of sound, 343 m/s at 20°C in air. The velocity depends on the temperature structure, wind, and the composition of the atmosphere. Thus, the effective speed of sound incorporating these effects is given by

$$c_{eff} = \sqrt{\gamma_g RT} + \hat{n} \cdot \vec{u}, \tag{1.9}$$

where $\sqrt{\gamma_g RT}$ gives the adiabatic speed of sound (m/s) and $\hat{n} \cdot \vec{u}$ projects the wind vector $\vec{u}$ in the direction from source to observer $\hat{n}$. Infrasound may refract where c_{eff} becomes greater than the effective velocity at the surface (Fig. 1.5).

The stratospheric returns can be distinguished from the thermospheric returns principally through their infrasound signal velocity (celerity) and also through their frequency content. Celerity is defined as the ratio of the range to the travel time from the source to receiver location. The thermospheric returns have lower celerity (0.22-0.24 km/s) due to their longer path compared to the stratospheric returns (0.28-0.31 km/s) (Ceplecha et al., 1998). In general, the thermospheric returns tend to have lower frequency content and the stratospheric returns have higher frequency content. This is due to frequency dependent attenuation where high frequency content is more efficiently removed during longer range propagation.

Infrasonic waves have very low signal attenuation in the atmosphere and are capable of propagating over large distances. Fig. 1.6 shows the approximate attenuation as a function of frequency and height.

For the case of bolides produced by meter-sized NEO impactors, the fundamental period is of the order of several seconds (sub 1 Hz). In this range, it can be seen from Fig. 1.6

---

[2] https://www.ctbto.org/

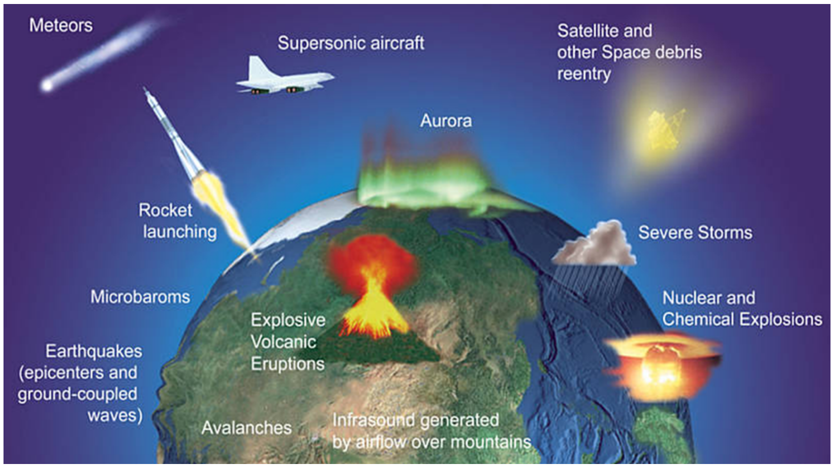

Figure 1.4: Sources of infrasound (from the web by CTBTO)

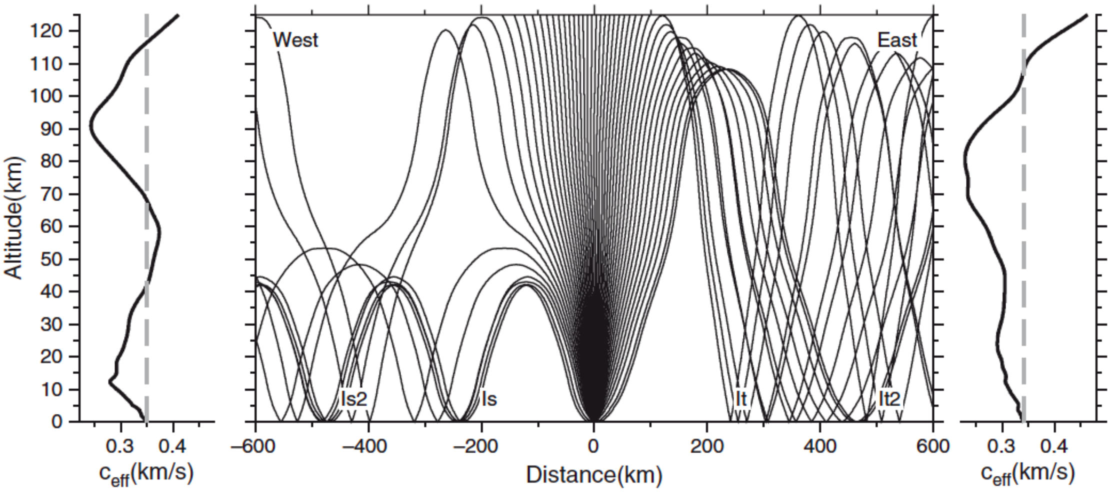

Figure 1.5: An example of infrasound raytracing showing rays from the source at an altitude 0 km shot every 4° from the vertical to the horizontal in a westward and eastward direction. The effective velocity profile for westward and eastward propagation is given in the left and right frame, respectively. In each frame, the dashed line indicates the surface value of the effective velocity (from Evers and Haak, 2010).

that provided ducted infrasonic waves do not travel into the thermosphere, the attenuation is negligible and detectability is global in scale.

The propagation of infrasound is greatly affected by stratospheric winds. There are two main features to take into account: jet streams and zonal mean circulation. Jet streams are narrow bands of strong wind in the top of the troposphere and lower stratosphere formed by a combination of the temperature gradient and Coriolis force. In the winter, jet streams become more active due to the greater difference in air temperatures between the pole and equator. The other important feature is zonal mean circulation in the stratosphere which has a strong westerly jet in the winter northern hemisphere and strong easterly jet in the summer northern hemisphere.

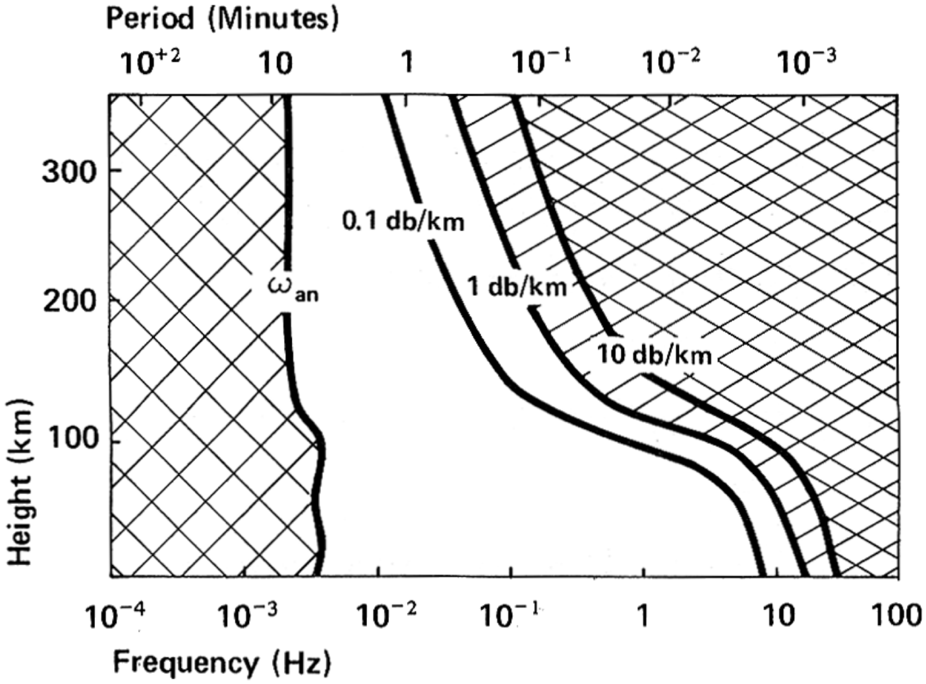

Figure 1.6: The approximate infrasound attenuation as a function of frequency and height per unit path length traveled. As an example, an infrasonic wave travelling at a height of 50 km at 10 Hz loses 1 dB of amplitude for every 1 km it travels. For a wave that travels at 100 km at 10 Hz, the amplitude decreases 10 dB every 1 km of propagation. ω_{an} is the lower frequency cutoff for acoustic waves. Infrasonic waves (ω_{an} - 20 Hz) lie well within the low attenuation region (from Beer, 1974).

1.2.2 Infrasound Network, Detection and Measurement

Because of infrasound's unique global propagation and detection properties, it has been used for detecting large atmospheric explosions for many decades. In the late 1940s in particular, infrasound was first recognized as a useful tool for detecting and geolocating nuclear explosions, which led to the deployment of a number of infrasound monitoring networks around the globe. Infrasound was widely used from the 1950s to the early 1970s in detecting and locating large nuclear explosions (10 kT - several MT). However, in the early 1970s, interest in the use of infrasound as a monitoring technology rapidly declined. This was due to the signing of the Limited Test-Ban Treaty (LTBT) in 1963, which prohibited testing of nuclear weapons in the atmosphere, oceans, and space, and also the deployment of sophisticated satellite-based detection systems.

On September 24, 1996, the Comprehensive Test-Ban Treaty (CTBT) was opened for signature. CTBT is a zero-yield treaty that prohibits all nuclear explosions. To enforce the CTBT, the International Monitoring System (IMS) was developed. The IMS is comprised of 4 monitoring technologies: seismic, infrasound, hydroacoustic, and radionuclide. The IMS adoption of infrasound as a key monitoring technology for the CTBT greatly increased the use of infrasonic detection as a tool for monitoring explosive sources, both natural and man-made in the atmosphere.

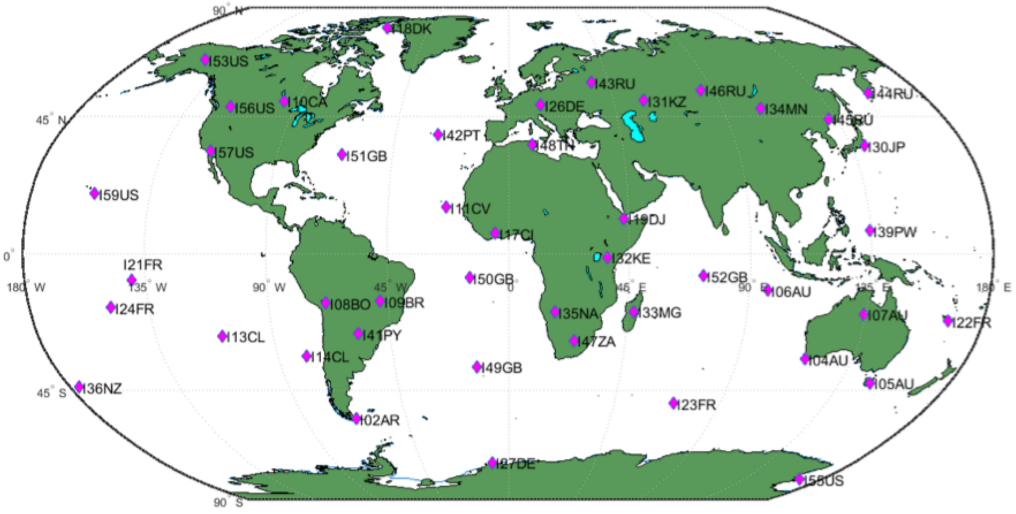

Figure 1.7: A global map showing the IMS infrasound network where each diamonds represents an operational infrasound station.

The IMS infrasound network consists of 60 infrasound stations uniformly distributed over the globe, 45 which are operating as of late 2016 (Fig. 1.7). The goal is to detect and locate nuclear explosions with a yield of 1 kT or less, anywhere on the globe. Most of these stations are designed with 7-8 array elements (minimum of 4 array elements) consisting of a pressure

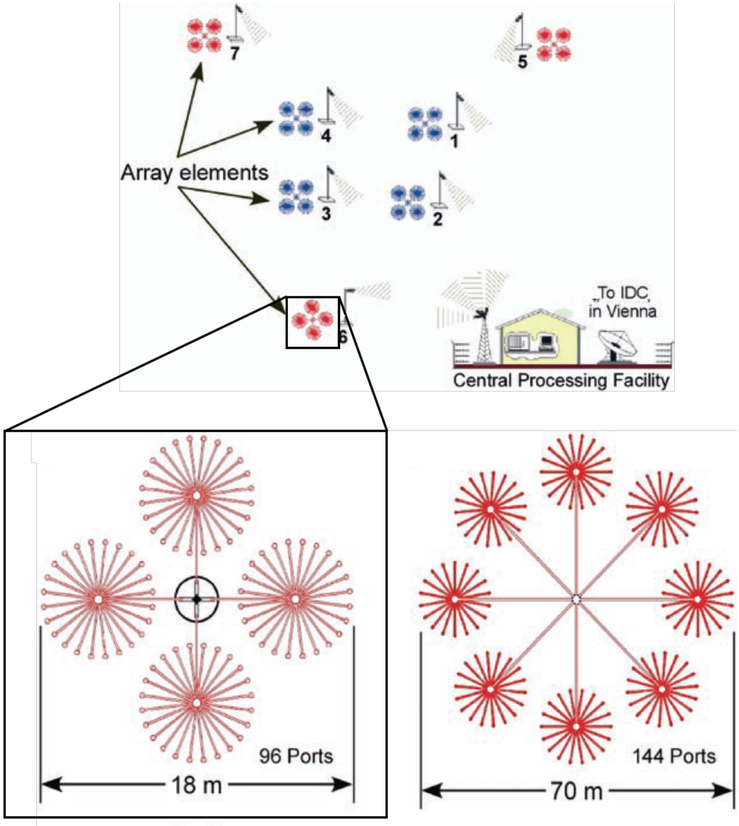

Figure 1.8: A schematic of typical 7 array elements IMS infrasound monitoring station (top). The bottom two diagrams illustrate two examples of wind-noise-reducing pipe array designs that are widely used throughout the IMS infrasound network (from Christie and Campus, 2010).

microbarometer placed at the center of each element. Each microbarometer is connected to a wind-noise-reducing pipe array which acts as a high-pass filter for infrasonic signals. Detection capability can be improved in high wind environments with a higher number of array elements and large pipe array.

Infrasonic signals detected from a microbarometer at each array element are digitized, authenticated and transmitted to a central processing facility. The data from all array elements are converted into a suitable format and transmitted to the International Data Centre (IDC). All IMS data are available to all signatory countries as part of the CTBT to allow each member state to analyse and decide for themselves if a nuclear explosion has occurred in violation of the treaty. As yet, the data are not regularly available for public scientific analysis. A schematic illustration of a typical IMS infrasound monitoring station with two examples of the wind-noise-reducing systems are shown in Fig. 1.8. As a coherent planar infrasonic wave sweeps across the array, the waveform cross-correlation algorithms allow signal arrival time, trace velocity and back azimuth to be determined. More details on the signal processing and analysis techniques can be found in Brachet et al. (2010).

1.3 Aim, Motivation and Thesis Outline

The work in this thesis aims to provide better understanding of small (1 - 20 m) near-Earth objects by examining their infrasound signature to estimate their source energy, possible correlation of this energy with secondary characteristics (entry angle, source height, speed) and to better quantify their impact consequences, specifically blast wave damage at the Earth's surface.

The specific major goals include: refinement of bolide characteristics by correlating their characteristics (height, speed, and entry angle) with infrasound signal period, to understand the root cause of variability in signal periods between infrasound stations and hence energy estimates for individual bolides and to estimate the frequency of window damage caused by shock waves produced by bolides.

Previous work has focused on determining bolide kinetic energy from infrasound signal measurements. For each single bolide event, these signal periods were found to vary by factors of several from independent estimates at multiple stations. The main deficiency of earlier studies was an absence of information about bolide characteristics such as burst height, speed and entry angle. For example, the burst height is expected to affect infrasound signal period significantly. Previous studies were unable to examine its role in energy estimation using infrasound due to lack of data. NASA Jet Propulsion Laboratory (JPL) fireball data[3] now provides the ground-truth secondary characteristics of bolides which permit examination for the first time of the secondary bolide entry characteristics which may affect energy estimates of bolides from

---

[3] http://neo.jpl.nasa.gov/fireballs/

infrasound measurements.

The thesis is organized as follows:

In Chapter 2, we review the basic literature relating to the flux of small NEOs and bolide energy estimation techniques from infrasound signals. In particular we summarize past empirical relations using infrasound amplitude and period to estimate atmospheric explosive yields.

In Chapter 3, we focus on establishing better estimates of bolide kinetic energy. I do this by exploring the relationship between independent estimates of bolide characteristics provided from NASA JPL fireball data and measured infrasound parameters. I try to determine what causes the wide spread in interstation infrasound signal periods. A complementary focus was on determining the bolide burst (source) height to examine how it affects energy estimates.

The 2013 Chelyabinsk fireball was the first recorded event producing an air blast shock wave that led to window damage. Several thousand buildings were damaged and over one thousand people were injured mostly due to the flying glass and cracking of windows (Popova et al., 2013). This event highlighted the prospect of small NEOs posing a significant impact damage threat on Earth due to airblast loading (overpressure), particularly on windows. This incident thus leads to a broader interesting question: how often do we expect fireballs to break windows on the ground?

In Chapter 4, we examined how damaging these shock waves can be on the ground. I employed a numerical bolide entry model (the TPFM model) to generate the energy deposition profile and the resulting output was coupled with the ReVelle (1976) weak shock model to compute the expected overpressures (ΔP) on the ground. I computed the area of the ground footprint where the overpressure is large enough to break windows. Then, we estimated the frequency with which we expect fireballs to produce window damage.

In Chapter 5, we summarize our major findings and discuss the implications of our main conclusions.

Bibliography

Avramenko, M. I., Glazyrin, I. V., Ionov, G. V., and Karpeev, A. V. (2014). Simulation of the airwave caused by the chelyabinsk superbolide. *Journal of Geophysical Research: Atmospheres*, 119(12):7035–7050.

Borovička, J., Spurný, P., and Brown, P. (2015). Small Near-Earth Asteroids as a Source of Meteorites. In *Asteroids IV*, pages 257–280.

Borovička, J., Spurný, P., Brown, P., Wiegert, P., Kalenda, P., Clark, D., and Shrbený, L. (2013). The trajectory, structure and origin of the Chelyabinsk asteroidal impactor. *Nature*, 503:235–237.

Boslough, M. B. E. and Crawford, D. A. (1997). Shoemaker-Levy 9 and Plume-Forming Collisions on Earth. *Annals of the New York Academy of Sciences*, 822:236–282.

Brachet, N., Brown, D., Le Bras, R., Cansi, Y., Mialle, P., and Coyne, J. (2010). Monitoring the Earths Atmosphere with the Global IMS Infrasound Network. In *Infrasound Monitoring for Atmospheric Studies*, chapter 3, pages 77–118. Springer Science. Business Media B.V.

Brown, P., Spalding, R. E., ReVelle, D. O., Tagliaferri, E., and Worden, S. P. (2002). The flux of small near-Earth objects colliding with the Earth. *Nature*, 420:294–296.

Brown, P. G., Assink, J. D., Astiz, L., Blaauw, R. C., Boslough, M. B., Borovička, J., Brachet, N., Brown, D., Campbell-Brown, M. D., Ceranna, L., Cooke, W., de Groot-Hedlin, C., Drob, D. P., Edwards, W. N., Evers, L. G., Garces, M., Gill, J., Hedlin, M., Kingery, A., Laske, G., Le Pichon, A., Mialle, P., Moser, D. E., Saffer, A., Silber, E., Smets, P., Spalding, R. E., Spurný, P., Tagliaferri, E., Uren, D., Weryk, R., Whitaker, R., and Krzeminski, Z. (2013). A 500-kiloton airburst over Chelyabinsk and an enhanced hazard from small impactors. *Nature*, 503:238–241.

Ceplecha, Z., Borovička, J., Elford, W. G., ReVelle, D. O., Hawkes, R. L., Porubčan, V., and Šimek, M. (1998). Meteor Phenomena and Bodies. *Space Science Reviews*, 84:327–471.

Chyba, C. F., Thomas, P. J., and Zahnle, K. J. (1993). The 1908 Tunguska explosion - Atmospheric disruption of a stony asteroid. *Nature*, 361:40–44.

Collins, G. S., Lynch, E., McAdam, R., and Davison, T. M. (2017). A numerical assessment of simple airblast models of impact airbursts. *Meteoritics & Planetary Science*, 19:1–19.

Collins, G. S., Melosh, H. J., and Marcus, R. A. (2005). Earth Impact Effects Program: A Web-based computer program for calculating the regional environmental consequences of a meteoroid impact on Earth. *Meteoritics and Planetary Science*, 40:817–840.

Ens, T. A., Brown, P. G., Edwards, W. N., and Silber, E. A. (2012). Infrasound production by bolides: A global statistical study. *Journal of Atmospheric and Solar-Terrestrial Physics*, 80:208–229.

Hills, J. G. and Goda, M. P. (1993). The fragmentation of small asteroids in the atmosphere. *Astronomical Journal*, 105:1114–1144.

Hills, J. G. and Goda, M. P. (1998). Damage from the impacts of small asteroids. *Planetary and Space Science*, 46:219–229.

Popova, O. P., Jenniskens, P., Emel'yanenko, V., Kartashova, A., Biryukov, E., Khaibrakhmanov, S., Shuvalov, V., Rybnov, Y., Dudorov, A., Grokhovsky, V. I., Badyukov, D. D., Yin, Q.-Z., Gural, P. S., Albers, J., Granvik, M., Evers, L. G., Kuiper, J., Kharlamov, V., Solovyov, A., Rusakov, Y. S., Korotkiy, S., Serdyuk, I., Korochantsev, A. V., Larionov, M. Y., Glazachev, D., Mayer, A. E., Gisler, G., Gladkovsky, S. V., Wimpenny, J., Sanborn, M. E., Yamakawa, A., Verosub, K. L., Rowland, D. J., Roeske, S., Botto, N. W., Friedrich, J. M., Zolensky, M. E., Le, L., Ross, D., Ziegler, K., Nakamura, T., Ahn, I., Lee, J. I., Zhou, Q., Li, X.-H., Li, Q.-L., Liu, Y., Tang, G.-Q., Hiroi, T., Sears, D., Weinstein,

I. A., Vokhmintsev, A. S., Ishchenko, A. V., Schmitt-Kopplin, P., Hertkorn, N., Nagao, K., Haba, M. K., Komatsu, M., Mikouchi, T., and the Chelyabinsk Airburst Consortium (2013). Chelyabinsk Airburst, Damage Assessment, Meteorite Recovery, and Characterization. *Science*, 342:1069–1073.

Register, P. J., Mathias, D. L., and Wheeler, L. F. (2017). Asteroid fragmentation approaches for modeling atmospheric energy deposition. *Icarus*, 284:157–166.

ReVelle, D. O. (1976). On meteor-generated infrasound. *Journal of Geophysical Research*, 81:1217–1230.

ReVelle, D. O. (1979). A quasi-simple ablation model for large meteorite entry - Theory vs observations. *Journal of Atmospheric and Terrestrial Physics*, 41:453–473.

ReVelle, D. O. (2001). Theoretical Leonid entry modeling. In *Meteoroids 2001 Conference*, volume 495 of *ESA Special Publication*, pages 149–154.

ReVelle, D. O. (2002). Fireball dynamics, energetics, ablation, luminosity and fragmentation modeling. In *Asteroids, Comets, and Meteors: ACM 2002*, volume 500 of *ESA Special Publication*, pages 127–136.

ReVelle, D. O. (2005). Recent Advances in Bolide Entry Modeling:A Bolide Potpourri. *Earth Moon and Planets*, 97:1–35.

Robertson, D. K. and Mathias, D. L. (2017). Effect of yield curves and porous crush on hydrocode simulations of asteroid airburst. *Journal of Geophysical Research: Planets*, 122:599–613.

Shuvalov, V., Svetsov, V., Popova, O., and Glazachev, D. (2017). Numerical model of the Chelyabinsk meteoroid as a strengthless object. *Planetary and Space Science (in press)*.

Shuvalov, V. V., Svettsov, V. V., and Trubetskaya, I. A. (2013). An estimate for the size of the area of damage on the Earth's surface after impacts of 10-300-m asteroids. *Solar System Research*, 47:260–267.

Shuvalov, V. V. and Trubetskaya, I. A. (2007). Aerial bursts in the terrestrial atmosphere. *Solar System Research*, 41:220–230.

Tsikulin, M. A. (1970). Shock waves during the movement of large meteorites in the atmosphere (No. NIC-Trans-3148). Naval Intelligence Command Alexandria VA Translation Div.

Chapter 2

Literature Review

2.1 Flux and Bolide Energy

Observations of bolides and estimation of their characteristics provide critical clues to the physical properties, structure, population properties, and the flux of small NEOs, some of which could pose an impact threat to the Earth (Borovička et al., 2015; Brown et al., 2002).

Brown et al. (2002) examined the satellite records of bolide detonations to estimate the flux of small NEOs. Their study determined a power-law relationship between the flux and bolide energy, where an object with the equivalent energy of 0.3 kT of TNT strikes the Earth every month, a 5 kT object striking annually, a 50 kT object striking every 10 years, and a 10 MT object striking every 1000 years (Brown et al., 2002). Silber et al. (2009) used infrasound measurements to estimate the flux of meter-sized meteoroids (5 - 20 m diameter) and suggested a more gradual slope of flux with respect to energy than that of the Brown et al. (2002) satellite observation study. The Silber et al. (2009) relations predict one impact of 11 - 12 kT annually, and a large (MT) event to happen every 15 years. Most recently, Brown et al. (2013) estimated the bolide flux based on 20 years (1994 - 2013) of global observations from U.S. government sensors. The flux of small size bolides (< 5 m in diameter) was found to be comparable with earlier telescopic studies and infrasonic influx estimates. However, the Brown et al. (2013)

bolide flux at larger sizes (15 - 30 m in diameter) resulted in an order of magnitude greater cumulative number impacting the Earth per year than earlier studies due to a single large event, Chelyabinsk, which was estimated to have an airburst energy of 500 kT. Exclusion of the Chelyabinsk event and two other large events (E > 30 kT) produced a nearly identical power-law slope to the Brown et al. (2002) previous study.

Fig. 2.1 shows the current estimated population of small NEOs from various sources - the flux in the decameter range remains the most uncertain, with more than an order of magnitude variance between some telescopic population estimates and direct estimates from bolide measurements. Details are given in the figure caption.

In constructing these flux curves from bolide data, energy is the primary measurable characteristic. Several previous studies have used infrasound measurements alone to estimate NEO flux (e.g. Silber et al. 2009; ReVelle 1997). These studies require individual infrasound bolide measurements be used to estimate source energy. ReVelle (1974, 1976) presented the first theoretical method of using infrasound to measure the propagation and attenuation of bolide airwaves and developed the analytic theory as to how the resulting infrasound amplitude and periods relate to bolide energy. Extension of this early work has included a number of studies, which sought to improve energy estimation accuracy for bolides using both theoretical methods and applications of empirical estimates from man-made ground-level explosions.

The bolide infrasound theory of ReVelle (1976) is a useful baseline, but does not include various real-world effects which modify the observed infrasound signal. These effects include nonlinear attenuation of the infrasound bolide signal, propagation and wind effects, turbulence, ducting, diffraction, and station noise among other shortcomings.

As a result, several different studies have developed relations associating amplitude (overpressure) and period of infrasound signals to the explosion yield (energy) and range from source to receiver from various observational data sources. These empirical energy scaling equations are real-world attempts to characterize the expected amplitude-period-yield relationships for infrasound measurements.

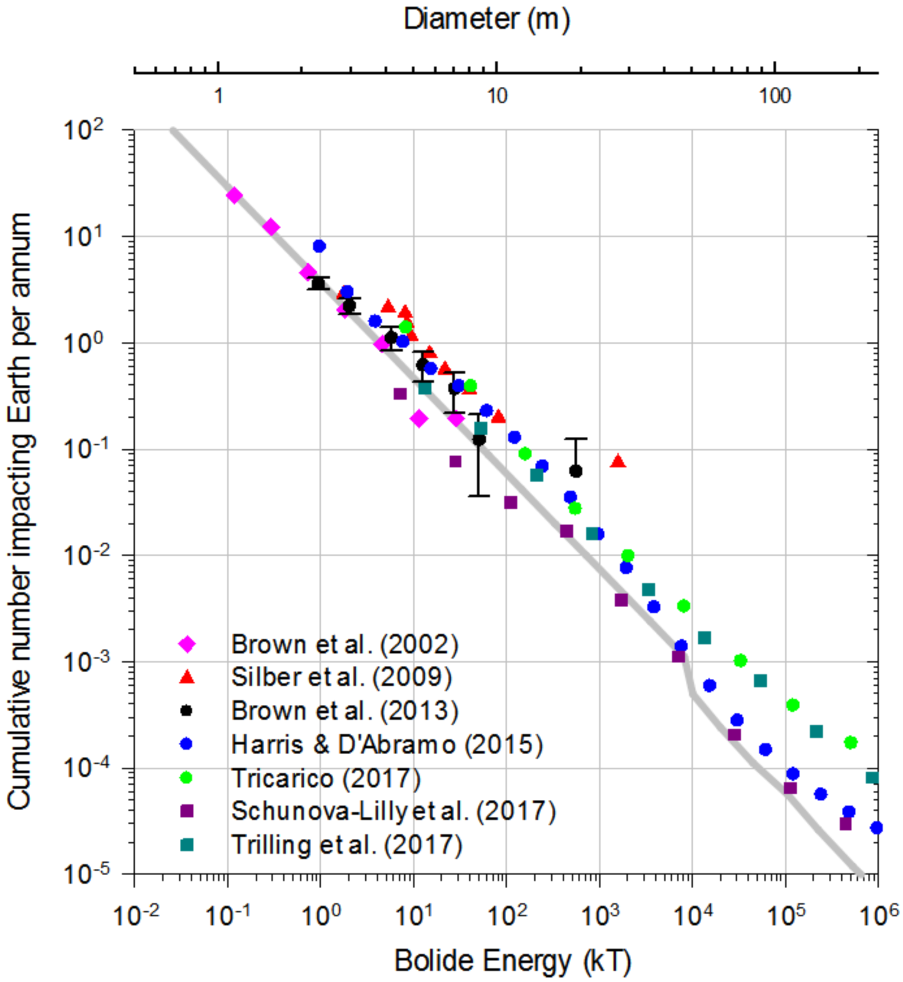

Figure 2.1: The estimated flux of near-Earth objects impacting the Earth using various techniques. The satellite-observed bolide impacts based on 8.5 years of global observations (pink diamonds) reported by Brown et al. (2002) as well as the power law fit to these data are shown (grey solid line). The influx rate of meter-sized meteoroids (5 - 20 m diameter) inferred from infrasound measurements by the U.S. Air Force Technical Applications Center (AFTAC) acoustic recordings over a period of 13 years (early 1960s - mid 1970s) as analysed by Silber et al. (2009) are shown in red triangles. These infrasound measurements from the AFTAC-operated network differ from the International Monitoring System (IMS) in several respects including setup, sampling rate, and noise/signal processing. In particular, the AFTAC data was stored on paper tapes as described in Silber et al. (2009). Array elements of the AFTAC-operated network have larger separations (6 - 12 km) compared to the IMS network (1 - 3 km) and the AFTAC-operated network has lower signal-to-noise ratios. The AFTAC flux is computed based on a seasonal dependent completeness assuming a simple stratospheric wind model as described in ReVelle (1997). The black circles are the measured debiased bolide impactor flux based on 20 years (1994 - 2013) of global observations from U.S. government sensors as presented in Brown et al. (2013).

Figure 2.1: For comparison, four telescopic survey studies (Harris and D'Abramo, 2015; Tricarico, 2017; Schunová-Lilly et al., 2017; Trilling et al., 2017) are also shown. These studies estimated the total population of NEOs based on debiasing of telescopic detections of NEOs with survey simulations. The blue circles are estimates from Harris and D'Abramo (2015) where they estimated the size-frequency distribution of NEAs using the re-detection ratio (fraction of population that are re-detections of already known asteroids rather than new discoveries) from all surveys to estimate population completion. They translated their debiased estimate of the population of NEAs to an equivalent annual cumulative impact flux (ordinate in this graph) using a single average value for the impact probability of 2×10^{-9} year^{-1}. Tricarico (2017) (green circles) was based on an analysis of the combined telescopic observations of nine asteroid surveys over the past two decades. In this study, they calculated the observed impact probability for every NEA absolute magnitude bin instead of using an average value. Giving equal weight to all sampled orbits, the average value of the impact probability is 6×10^{-9} year^{-1} while weighting orbits by the estimated population gives 4×10^{-9} year^{-1}. Schunová-Lilly et al. (2017) (purple squares) estimated the NEO population based on simulating the detection for NEOs with the absolute magnitude (H) between 13 and 30 and Asteroid Retrieval Mission (ARM) targets with $27 < H < 31$ using data from the 1st telescope of the Panoramic Survey Telescope and Rapid Response System (Pan-STARRS1). To check the detection efficiency, they artificially injected NEOs and ARM targets that met a size-dependent Minimum Orbit Intersection Distance (MOID) requirement with Earth to debias the survey. Trilling et al. (2017) (cyan squares) analyzed the first year of survey data from the Dark Energy Camera (DECam) on the 4-meter Blanco telescope at the Cerro Tololo Inter-American Observatory (CTIO) to estimate the NEO population. They measured the detection efficiency by implanting synthetic NEOs in their data stream, which allowed them to debias and measure the size distribution of NEOs down to 10 m diameters. The impact probability was not explicitly reported in this study. However, assuming their NEO population estimate is correct, their result implies a factor of ten greater impact probability than previously assumed in Brown et al. (2002) and Harris and D'Abramo (2015). In the figure, the cumulative number impact rate was plotted from their assumed population using the impact probability of 2×10^{-8} year^{-1}.

2.2 Atmospheric Explosive Energy Derived From Infrasound Signal Amplitude

Here we briefly review previous studies which focus on using the pressure amplitude from an explosive signal to estimate source energy. Throughout this chapter, W is used to represent the explosion weight in keeping with the weapons effects literature and E is used to represent the initial total energy of the explosion/bolide.

The American National Standards Institute (ANSI) derived an overpressure-yield relation based on nuclear explosions ranging from 1 kT to several MT at low amplitudes (ANSI, 1983):

$$\Delta p = 6.526 W^{0.3667} R^{-1.1} (p/p_o)^{0.663}, \tag{2.1}$$

where Δp is the overpressure (Pa), W is the yield (kT), R is the source to receiver range (km), p and p_o are the atmospheric pressure at the source and receiver, respectively.

Blanc et al. (1997) developed the following amplitude-yield relation by analyzing French nuclear tests:

$$\log W = 2 \log A + 3.52 \log R - 10.62, \tag{2.2}$$

where A is the infrasonic signal amplitude (Pa).

Another commonly used empirical energy relation was found from U.S. Air Force Technical Applications Centre (AFTAC) nuclear explosion data (Clauter and Blandford, 1998):

$$\log W = 2 \log A + 2.94 \log \Delta - 1.84, \tag{2.3}$$

where Δ is the distance from source to receiver in degrees.

Using Soviet atmospheric nuclear explosion, similar relations were developed for down-wind and crosswind returns, respectively (Stevens et al., 2006) :

$$\log W = 3.03\log A + 3.03\log R - 9.09 \tag{2.4a}$$

$$\log W = 3.03\log A + 3.03\log R - 10 \tag{2.4b}$$

All the above equations are plotted on Fig. 2.2. Note that there are large variations between different studies, emphasizing the difficulty of using amplitude-only estimates for yields.

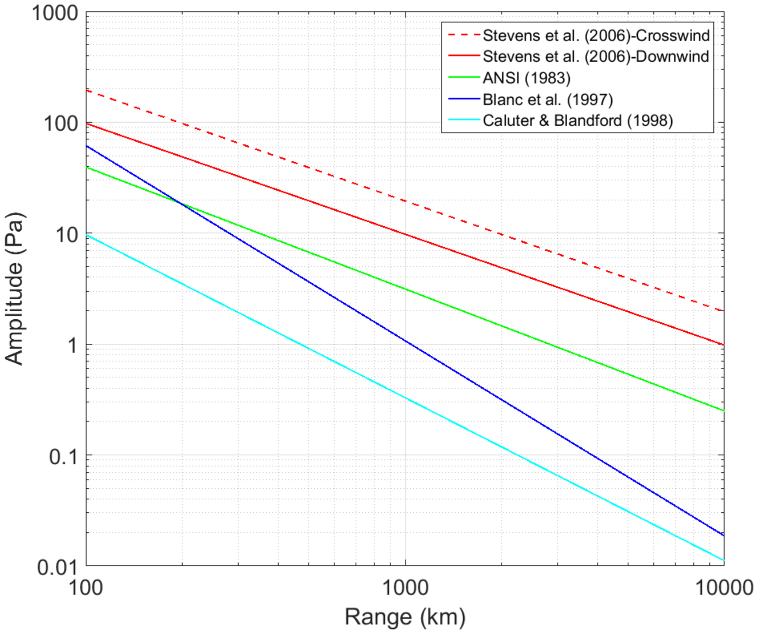

Figure 2.2: The previous empirical amplitude-range relations for an explosion of 1 kT yield.

It was noted in Chapter 1 that stratospheric wind can have a significant effect on the propagation of infrasound. Since infrasonic waves propagate through a moving medium, a correction must be applied based on wind speed. Infrasound measurements of high explosive sources (specifically mixtures of fuel oil and ammonium nitrate with yields approaching small nuclear explosions) were conducted by the US Defense Nuclear Agency suggesting an amplitude-yield relation of (Mutschlecner and Whitaker, 2010):

$$\log W = 1.49\log A_w + 2.00\log R - 4.18, \tag{2.5}$$

where W is the yield in tons of ANFO equivalent (1 tons of ANFO = 1.42 tons of TNT) and A_w is the wind normalized amplitude in microbars (1 microbar = 0.1 Pa). In Mutschlecner and Whitaker (2010), the amplitude was normalized for the effects of wind by applying the following equation:

$$A_w = 10^{kv_h} A, \tag{2.6}$$

where k is an empirical constant (s/m) and v_h is the horizontal component of the stratospheric wind directed toward the receiver (m/s).

A similar empirical approach has been employed to estimating bolide energies from amplitude. Edwards et al. (2006) examined 31 bolide events observed both by optical and infrared space-based sensors and resulted in the following amplitude-yield equation:

$$\log W = 1.71 \log A_w + 3 \log R - 0.03v - 5.49, \tag{2.7}$$

where v is the average stratospheric wind velocity (m/s) directed toward the receiver.

Building on the study of Edwards et al. (2006), Ens et al. (2012) developed empirical relations between bolide total energy and infrasound signal amplitude based on 71 satellite detected bolides:

$$\log W = 2.26 \log A_w + 2.41 \log R - 0.015v - 9.95 \tag{2.8}$$

Fig. 2.3 compares three altitude-energy relations with a wind correction of the form (Eq. 2.6) applied. Despite applying the wind correction, a large variation between relations can be seen. Since these relations are linear in log-space, a small difference in slope can translate into a large uncertainty in energy. Also, depending on the wind direction, there is a vertical shift of almost a factor of 2 as shown in Fig. 2.3.

The infrasonic signals propagating along the wind directions (i.e. the wind is directed from the source to the receiver) show larger amplitudes than signals moving against the prevailing stratospheric winds. Generally, the wave period is modified only by the doppler shift due to the wind and this is much less than the modification experienced by infrasound amplitude during

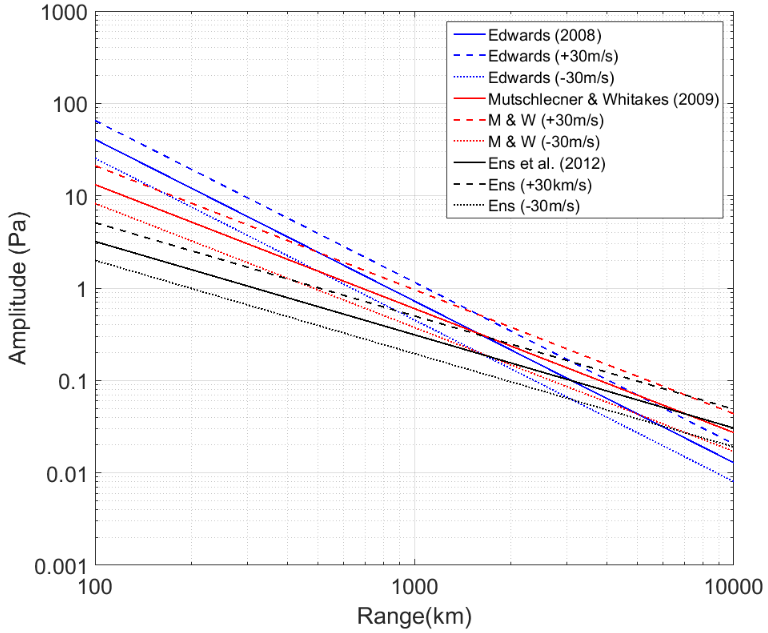

Figure 2.3: The previous empirical amplitude-energy relations with a correction applied based on wind speed. Plots are generated for an explosion of equivalent 1 kT yield. Dashed lines represent the average 30 m/s stratospheric wind blowing toward the receiver while dotted lines indicate the same magnitude velocity of stratospheric winds directed away from the receiver.

propagation. Thus, we expect a priori the period-yield relationship to be more robust (ReVelle, 1997).

2.3 Atmospheric Explosive Energy Derived From Infrasound Signal Period

The most commonly used period-energy relations for estimation of ground-based or atmospheric explosions from infrasound signals are the Air Force Technical Applications Center (AFTAC) relations (ReVelle, 1997; Edwards et al., 2006; Ens et al., 2012). These were developed through measurements of the observed dominant infrasound period for known nuclear explosion yields. The period-yield regressions are provided by ReVelle (1997):

$$\log(E) = 3.34\log(\tau) - 2.28, \qquad E \leq 200\ \mathrm{kT} \tag{2.9a}$$

$$\log(E) = 4.14\log(\tau) - 3.31, \qquad E \geq 80\ \mathrm{kT} \tag{2.9b}$$

where E is energy in kT of TNT equivalent and τ is the observed infrasound signal period in seconds. Similar empirical energy relations were derived by Stevens et al. (2002) who used infrasound signal measurements from Soviet atmospheric nuclear tests conducted in 1957 and 1961 to analyse the period-yield relationships. Fig. 2.4 shows the measured period as a function of yield for AFTAC and Stevens et al. (2002) data. The most striking aspect of both results is the substantial scatter in the signal period for a given event (vertical lines). Unfortunately, the original paper records for both datasets are no longer available so we cannot explore directly the causes for this large interstation scatter.

By observing 31 bolides which had infrasonic waves detected in common with satellite observations, Edwards et al. (2006) derived an equation similar to the AFTAC relation but relating the total energy of the bolide with observed infrasound period. Silber et al. (2011) analyzed infrasonic signals produced by a large fireball that occurred over Indonesia on October 8, 2009. They found the Edwards et al. (2006) energy estimates and AFTAC period-energy relationship to be robust. However, their new modeling and raytracing techniques placed more solid constraints on energy estimation by associating specific parts of the bolide trajectory with signals received at a particular station.

Building on the study of Edwards et al. (2006), Ens et al. (2012) refined empirical relations between bolide characteristics and infrasound signal properties based on a combined study of 71 satellite detected infrasound bolides. They established a power-law relationship between bolide kinetic energy and infrasonic wave period that is linear in log-log space (Fig. 2.5a). The

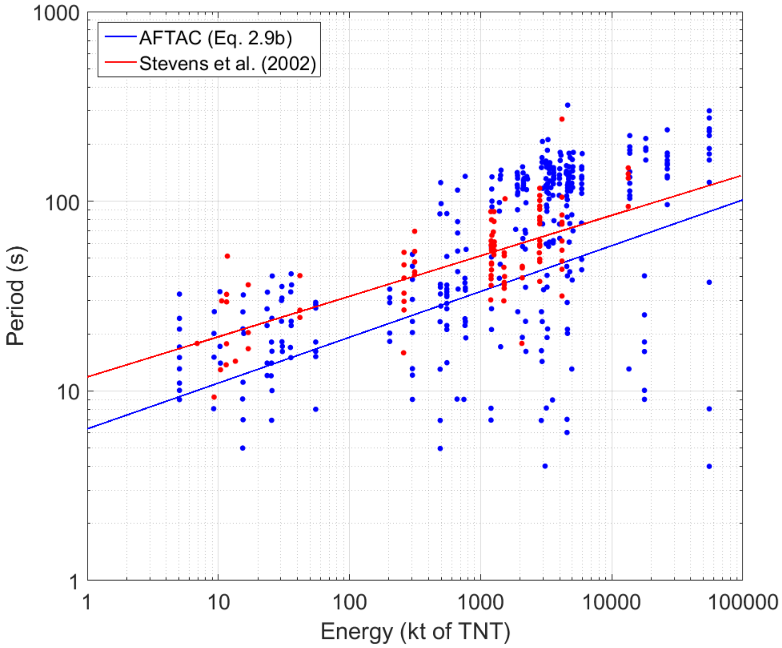

Figure 2.4: Previous empirical infrasonic period-energy relations based on nuclear explosions. The original AFTAC infrasound data is shown in blue and Stevens et al. (2002) Russian nuclear tests data is shown in red. Each vertical set of points represents the spread in station periods for one nuclear tests. Note that some of the nuclear explosions are common to both datasets, the blue points having been measured at AFTAC stations and the red points at Soviet stations.

best-fit regression equation was given by

$$\log(E) = 3.75(\log\tau) + 0.50, \tag{2.10}$$

where E is the satellite-measured bolide kinetic energy in tons of TNT and τ is the infrasonic wave period in seconds. This individual station period fit showed considerable scatter. A tighter fit was found by using multi-station averages for the 30 bolides detected at more than one station (Fig. 2.5b). For this multi-station average a fit of the form:

$$\log(E) = 3.28(\log\bar{\tau}) + 0.71, \tag{2.11}$$

where $\bar{\tau}$ is the multi-station period average was computed. However, Ens et al. (2012) could not further examine the underlying cause of the period scatter per event as the correlation with

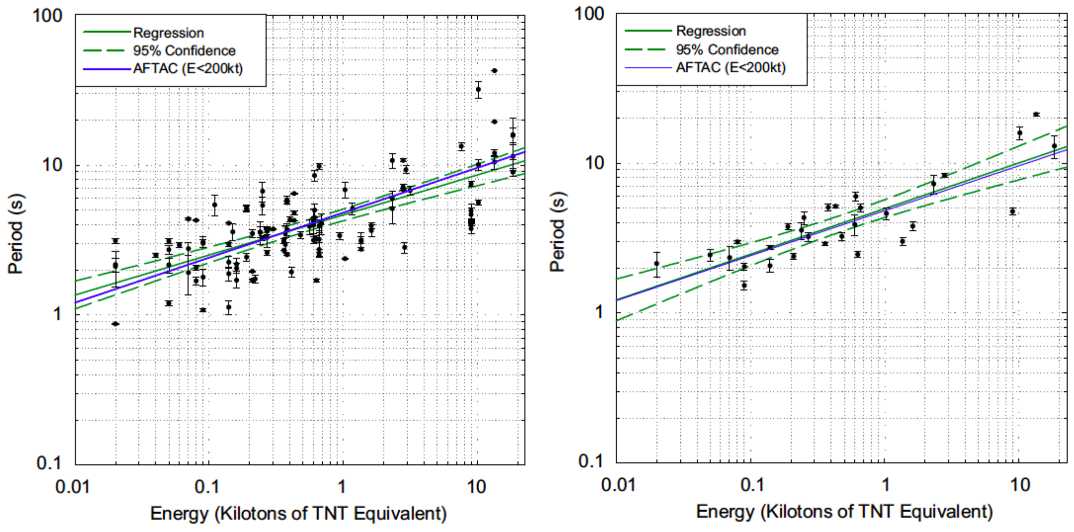

(a) (b)

Figure 2.5: The infrasound signal period vs. satellite-measured energy (from Ens et al. (2012)). (a) Each point represents the signal period at individual station. (b) Each point represents the averaged signal period from multiple stations observed for an individual fireball where independent detection by satellite systems provides a ground-truth estimate for bolide total energy (from Ens et al., 2012).

bolide source characteristics with amplitude or period due to lack of ancillary data on each bolide's trajectory, speed and burst height.

In the next chapter, the problem of interstation period variability per bolide event is examined in detail together with the possible correlation of period with other aspects of bolide ablation in the atmosphere. I extend the Ens et al. (2012) study using NASA JPL fireball data and explore improvements and limitations in infrasound empirical relationships for bolides, particularly with respect to signal period scatter.

Bibliography

ANSI (1983). Estimating airblast characteristics for single point explosions in air, with a guide to evaluation of atmospheric propagation and effects. Technical report, American National Standards Institute.

Blanc, E., Millies-Lacroix, J. C., Issartel, J. P., and Perez, S. (1997). Detection of Nuclear Explosions in the Atmosphere. *Chocs*, 17:23–34.

Borovička, J., Spurný, P., and Brown, P. (2015). Small Near-Earth Asteroids as a Source of Meteorites. In *Asteroids IV*, pages 257–280.

Brown, P., Spalding, R. E., ReVelle, D. O., Tagliaferri, E., and Worden, S. P. (2002). The flux of small near-Earth objects colliding with the Earth. *Nature*, 420:294–296.

Brown, P. G., Assink, J. D., Astiz, L., Blaauw, R., Boslough, M. B., Borovička, J., Brachet, N., Brown, D., Campbell-Brown, M., Ceranna, L., Cooke, W., de Groot-Hedlin, C., Drob, D. P., Edwards, W., Evers, L. G., Garces, M., Gill, J., Hedlin, M., Kingery, A., Laske, G., Le Pichon, A., Mialle, P., Moser, D. E., Saffer, A., Silber, E., Smets, P., Spalding, R. E., Spurný, P., Tagliaferri, E., Uren, D., Weryk, R. J., Whitaker, R., and Krzeminski, Z. (2013). A 500-kiloton airburst over Chelyabinsk and an enhanced hazard from small impactors. *Nature*, 503:238–241.

Clauter, D. A. and Blandford, R. R. (1998). Capability modeling of the proposed international monitoring system 60-station infrasonic network, LAUR-98-56. Technical report, Los Alamos National Laboratory, Los Alamos, New Mexico.

Edwards, W. N., Brown, P. G., and ReVelle, D. O. (2006). Estimates of meteoroid kinetic energies from observations of infrasonic airwaves. *Journal of Atmospheric and Solar-Terrestrial Physics*, 68:1136–1160.

Ens, T. A., Brown, P. G., Edwards, W. N., and Silber, E. A. (2012). Infrasound production by bolides: A global statistical study. *Journal of Atmospheric and Solar-Terrestrial Physics*, 80:208–229.

Harris, A. W. and D'Abramo, G. (2015). The population of near-Earth asteroids. *Icarus*, 257:302–312.

Mutschlecner, J. P. and Whitaker, W. R. (2010). Some atmospheric effects on infrasound signal amplitudes. In *Infrasound Monitoring for Atmospheric Studies*, chapter 14, pages 455–474. Springer Science. Business Media B.V.

ReVelle, D. O. (1974). *Acoustics of meteors-effects of the atmospheric temperature and wind structure on the sounds produced by meteors*. PhD thesis, Michigan University, Ann Arbor.

ReVelle, D. O. (1976). On meteor-generated infrasound. *Journal of Geophysical Research*, 81:1217–1230.

ReVelle, D. O. (1997). Historical Detection of Atmospheric Impacts by Large Bolides Using Acoustic-Gravity Waves. *Annals of the New York Academy of Sciences*, 822:284–302.

Schunová-Lilly, E., Jedicke, R., Vereš, P., Denneau, L., and Wainscoat, R. J. (2017). The size-frequency distribution of H > 13 NEOs and ARM target candidates detected by Pan-STARRS1. *Icarus*, 284:114–125.

Silber, E. A., Le Pichon, A., and Brown, P. G. (2011). Infrasonic detection of a near-Earth object impact over Indonesia on 8 October 2009. *Geophysical Research Letters*, 38:L12201.

Silber, E. A., ReVelle, D. O., Brown, P. G., and Edwards, W. N. (2009). An estimate of the terrestrial influx of large meteoroids from infrasonic measurements. *Journal of Geophysical Research: Planets*, 114:E08006.

Stevens, J. L., Adams, D. A., Baker, G. E., Xu, H., Murphy, J. R., Divnov, I., and Bourchik, V. N. (2006). Infrasound modeling using soviet explosion data and instrument design criteria from experiments and simulations. Technical report, Institute for the Dynamics of the Geospheres, Moscow, Russia.

Stevens, J. L., Divnov, I. I., Adams, D. A., Murphy, J. R., and Bourchik, V. N. (2002). Constraints on Infrasound Scaling and Attenuation Relations from Soviet Explosion Data. *Pure and Applied Geophysics*, 159:1045–1062.

Tricarico, P. (2017). The near-Earth asteroid population from two decades of observations. *Icarus*, 284:416–423.

Trilling, D. E., Valdes, F., Allen, L., James, D., Fuentes, C., Herrera, D., Axelrod, T., and Rajagopal, J. (2017). The size distribution of Near Earth Objects larger than 10 meters. *ArXiv e-prints*.

Chapter 3

Refinement of Bolide Characteristics from Infrasound measurements

A version of this chapter has been published as:

Gi, N. and Brown, P. (2017) Refinement of Bolide Characteristics from Infrasound measurements, *Planetary and Space Science*. 143:169-181. doi:10.1016/j.pss.2017.04.021.

3.1 Introduction

The recognition that small (1 - 20 m) near-Earth asteroids (NEAs) may pose a significant impact threat to the Earth (Boslough et al., 2015) has led to a renewed impetus to further our understanding of these small near-Earth objects. Observations of bolides and estimation of their characteristics provide critical clues to physical properties, structure, and the overall NEA population such as the flux of small NEAs impacting the Earth (Borovička et al., 2015). In particular, fragmentation behavior, energy deposition with height and total energy yield when correlated with pre-atmospheric orbits may be used to broaden our understanding of the physical properties, structure, and characteristics of small NEAs both individually and as a population. With the development of the International Monitoring System (IMS) in the late 1990s as part of the Comprehensive Nuclear Test Ban Treaty Organization (CTBTO), infrasound stations have been continuously collecting low frequency sound on a global scale from explosive sources for more than a decade. Among the events regularly detected by the infrasound component of the IMS are bolides (Ens et al., 2012). Infrasound is low frequency sound waves extending from the atmospheric Brunt-Väisälä frequency to the limit of human hearing (0.001 - 20 Hz) (Bedard and Georges, 2000). Infrasound is ideal for remote sensing of bolides as such low frequency acoustic waves do not suffer significant attenuation over long distances, making detection and characterization of bolides at long ranges possible.

The IMS detects these objects as their entry to Earth's atmosphere is accompanied by luminous phenomena (collectively termed a meteor) including heat, ionization and in particular production of a shock. Meteors can produce two distinct types of shock waves. One is a hypersonic (or ballistic) shock wave, which radiates as a cylindrical line source and propagates almost perpendicular to the path of the meteor (Edwards, 2009). A second type of shock is produced when the meteoroid suddenly fragments depositing a large fraction of its total energy over a very short segment of its path. In this case the shock radiates more nearly as a point source (ReVelle, 1974). The detailed theory on the infrasound source of the bolides has been developed by ReVelle (1974, 1976), however they are most applicable at short ranges (< 300 km). The existing theory does not take into account intrinsic signal dispersion or effects of the atmospheric turbulence. Therefore, the meteor infrasound signal at large ranges can be modified due to shock wave interactions and conditions in the atmosphere between the meteoroids and the receiver.

In the past, optical observations using photographic, television and video technologies were the dominant techniques used to study bolides (Ceplecha et al., 1998). In the late 1990s, the use of infrasonic technology to register bolides greatly increased due to the establishment of the CTBTO and its implementation of the IMS network. The IMS consists of seismic, radionuclide, hydroacoustic and infrasound stations. The final IMS plan includes 60 global infrasound stations, though only some 45 are installed and operating as of late 2016.

Infrasonic measurements of bolides may provide source location, origin time and an estimate of yield (Edwards, 2010). The yield (or total bolide energy) is of great physical interest as it establishes the scale of the event and forms the most basic property needed to lead to better understanding of both the physical properties of asteroids and their flux at Earth, through ablation modeling. However, past studies using amplitude and particularly period of the infrasonic signal show large interstation variability for common events. Ens et al. (2012) showed that events detected with many stations may have more accurate yields estimated using the dominant period average across all stations, but such averaging is only possible for a limited subset of well observed events. A similar approach has been employed for ground based explosions by the Air Force Technical Applications Centre (AFTAC) which assumes a log normal distribution of periods (Antolik et al., 2014). The root cause of the dispersion in signal periods remains unknown. Possible explanations include:

1. Signals detected at different stations emanating from different positions/heights along the bolide trajectory as suggested by Silber et al. (2009). This could lead to period differences due to different blast radii as a function of energy deposition and/or due to the increased attenuation of higher frequencies for shocks emitted at higher altitudes artificially increasing the apparent signal period.
2. Doppler shifts caused by winds (Ens et al., 2012)
3. Dispersion effects in propagation to different ranges (ReVelle, 1974)
4. Height of burst effects (Herrin et al., 2008; Edwards et al., 2006)
5. Different noise characteristics at each site may alter the apparent period or mask its spectral characteristics (Bowman et al., 2005).
6. Measurement uncertainty and/or broad frequency peaks leading to imprecise dominant period measurements (Golden et al., 2012)

The goal of this study is to examine the infrasonic signals produced by a large sample of bolides, which have known properties as reported on the Web by NASA's Jet Propulsion

Laboratory (JPL) [1]. These data are based on U.S. government sensor detections of bolides and report bolide characteristics including location, time, energy, height, speed, and entry angle for a subset of events. This data is collected by U.S. Government sensors which monitor Earth's surface and atmosphere for events of interest, and is provided to NASA for scientific study of natural objects impacting the Earth.

Our aim is to explore empirical correlations between measured infrasound parameters at IMS stations (particularly dominant signal period) and bolide secondary characteristics reported on the JPL website. Beyond these empirical explorations, we investigate three test cases in detail to determine if signals emanating from different portions of bolide trails can provide self-consistent explanations for differing signal periods measured at different stations. We wish to test if possibility #1 in the foregoing list is viable explanation for station period scatter. These bolides include the February 15, 2013 Chelyabinsk fireball (Borovička et al., 2013), the September 3, 2004 Antarctica bolide (Klekociuk et al., 2005) and the Park Forest meteorite dropping fireball of March 27, 2003 (Brown et al., 2004). In these cases we have independent estimates of energy deposition and are able to apply raytracing to establish probable source heights. When combined with weak shock modelling (Edwards, 2010), we may then compare predicted dominant periods with observed periods to investigate if different source heights can self-consistently explain the differing station periods. Finally, in Appendix A section A.2 we provide a database of all our measured infrasound signals extracted from 179 stations representing detections of 78 fireballs (Table A.1).

3.2 Theory and Background

In previous studies, examinations of the satellite records of bolide detonations were used to estimate the flux of small NEAs (Brown et al., 2002). Their study determined a power-law relationship between the flux and bolide energy, such that a roughly 1 m diameter object

---

[1] http://neo.jpl.nasa.gov/fireballs/

having a total energy of ~0.1 kiloton TNT equivalent (1 kT = 4.184×10^{12} J) impacts Earth once every 1 - 2 weeks. For comparison, a 0.3 kiloton event occurs once every month, a 5 kiloton object strikes annually and one ~50 kiloton object is expected every 10 years (Brown et al., 2002). The IMS is able to detect energies as small as 0.1 kT at multiple stations if wind and geographical location are favorable so we expect ~dozens of bolides to be detected by the IMS annually (Brown et al., 2014).

The speed of a meteoroid impacting Earth is at least 11.2 km/s, though typical impact speeds are closer to 16 - 18 km/s (Brown et al., 2015). Thus, the geometry of the hypersonic shock cone is well approximated by a cylinder (ReVelle, 1974). The radius of the cylindrical line source, known as the blast radius (R_o), is the distance away from the meteoroid trajectory in the atmosphere wherein all of the deposited explosion energy would equal the expansion work required by the weak shock to move the surrounding atmosphere to this radius (Few, 1969). It corresponds approximately to the distance from the trajectory where the shock overpressure equals the ambient atmospheric pressure. Inside the blast radius the atmosphere is strongly shocked leading to non-linear wave propagation (Ens et al., 2012). Using cylindrical line source blast wave theory (Tsikulin, 1970), the blast radius can be calculated as:

$$R_o = \left(\frac{E_o}{P_o}\right)^{\frac{1}{2}}, \tag{3.1}$$

where E_o is the total energy per unit trail length and P_o is the ambient hydrostatic atmospheric pressure. We apply the ReVelle (1976) weak shock model to calculate the period of wave at ten blast radii by inverting the fundamental frequency of the wave, which is given by:

$$\tau_o = \frac{1}{f_o} = \frac{2.81 R_o}{C_s}, \tag{3.2}$$

where R_o is the blast radius and C_s is the speed of sound. This implies a power law relation between energy deposition per unit path length and infrasonic period at fixed source range, assuming atmospheric pressure is approximately constant.

ReVelle (1974, 1976) presented the first complete theoretical model of meteor infrasound. Extension and observational testing of this early work has included a number of studies, which sought to improve energy estimate accuracy for bolides using both theoretical methods and applications of empirical estimates from man-made ground-level explosions (Edwards et al., 2005, 2006; Ens et al., 2012; Silber et al., 2015). The empirical relations between bolide energy and infrasound properties (notably observed signal period and amplitude) were compared with ground-level explosive sources. The most common practical energy relations used were those produced by the U.S. Air Force Technical Applications Centre (AFTAC) (ReVelle, 1997) which related observed infrasound period to known nuclear explosion yields. The period-yield fits often quoted are:

$$\log(E) = 3.34\log(\tau) - 2.28, \qquad E \leq 200\ \text{kT} \tag{3.3a}$$

$$\log(E) = 4.14\log(\tau) - 3.31, \qquad E \geq 80\ \text{kT} \tag{3.3b}$$

where E is energy in kilotons of TNT equivalent and τ is the infrasound signal period. Fig. 3.1 shows the original data used to construct the AFTAC period fits. It is apparent that significant scatter in the period per event are present, as similarly shown in Stevens et al. (2002) who presented measured infrasound signals from Soviet atmospheric nuclear tests conducted in 1957 and 1961. They plotted measured period as a function of yield for all data and their result showed substantial scatter in the signal period.

Historically it has been assumed that the wave period is less modified than the amplitude during propagation. Thus, the period-yield relationship is taken to be more robust (ReVelle, 1997), though the effects of station period scatter have not been systematically investigated. Silber et al. (2011) used global infrasound records associated with the large October 8, 2009 bolide over Indonesia to explore the possibility that different station periods are due to signals emanating from different parts of the bolide trail. They found this to be a plausible explanation for the station period dispersions, but lacked observational ground-truth on the bolide trajectory and energy deposition to make more firm conclusions.

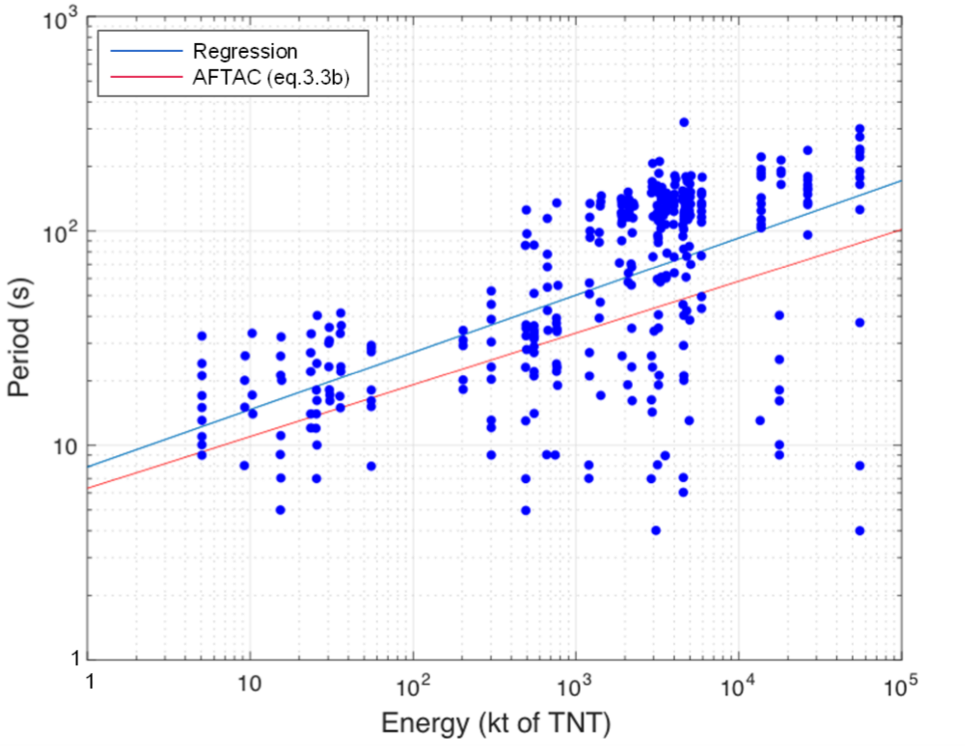

Figure 3.1: Original AFTAC infrasound data showing yield (x-axis) and individual station periods (y-axis). Note that some of the larger periods are likely Lamb-wave returns (but we do not have sufficient information to determine which of these points are Lamb-wave returns and which are not) and hence were likely not included in the original regression fit (shown in red). A direct regression fit to all data (blue line) produces a similar slope to the AFTAC relation with a vertical shift. Each vertical set of points represents the spread in station periods for one nuclear test.

Edwards et al. (2006) showed the theoretically expected change in apparent observed pressure amplitude at the ground scales with source altitude following:

$$\Delta p \propto \left(\frac{p_o}{p}\right)^{\frac{-2}{3}}, \tag{3.4}$$

where Δp is the amplitude, p_o is the pressure at ground level, and p is the pressure at the source height. An explosion with yield E at ground level will show a correspondingly larger apparent period as altitude increases as the blast radius (for a fixed energy yield) scales with ambient pressure – i.e. the blast cavity becomes larger for fixed energy with height. As a result, we expect explosions with constant yields to show larger periods with increasing height, an effect predicted by ReVelle (1976) and observed with small atmospheric explosions (Herrin et al., 2008). The main complication in using signal amplitude is the large corrections needed for the effects of winds, which makes inferring burst heights from amplitudes alone very challenging.

Building on the study of Edwards et al. (2006), Ens et al. (2012) developed empirical relations between bolide total energies as measured by satellites and infrasound signal properties based on a combined study of 71 bolides. Following the same empirical approach as used to generate Eq. 3.3(a/b) they found a power-law relationship between bolide total energy and infrasonic wave period that is linear in log-log space. The best-fit regression to all data was given by

$$\log(E) = 3.75(\log\tau) + 0.50, \tag{3.5}$$

where E is the satellite-measured bolide kinetic energy in tons of TNT and τ is the infrasonic wave period in seconds (Ens et al. (2012)). This single station period fit showed considerable scatter. A better fit was found by using multi-station averages for the 30 bolides detected at more than one station. For this multi-station average a fit of the form:

$$\log(E) = 3.28(\log\bar{\tau}) + 0.71, \tag{3.6}$$

where $\bar{\tau}$ is the multi-station period average was computed.

This is quite close to the AFTAC Eq. 3.3(a), a surprising result as the bolide energy deposition occurs at higher altitudes and hence we would expect larger periods for the same yield. The similar slope (3.28 vs. 3.34) reflects the fact that at the typical large station ranges in our dataset, the finite length of the bolide trail and the effects of atmospheric turbulence lead to the initially cylindrical wave becoming spherical at great distances (ReVelle, 1974). One subtly in comparing the AFTAC and bolide data is that we calibrate the bolide yield from the U.S. government sensors to total radiated energy, which is integrated over the entire path of the fireball. In contrast, the period observed at the ground represents only the energy deposition per unit trail length at some point along the trail, assuming multi-path propagation is not significant. So the correspondence between the AFTAC energies and the bolide total energies may simply be a reflection of the near balancing effects of burst height (which would tend to make the periods appear larger) and energy deposition per unit length (which makes the period appear smaller than if the entire yield occurred at one point).

However, Ens et al. (2012) could not explore the effects of bolide source characteristics on amplitude or period as they were unable to correlate infrasound signals with bolide height, entry angle and speed as these were unknown for their events. We note that while speed is unlikely to greatly affect infrasound characteristics (except indirectly through a correlation with source height) entry angle and the geographical orientation of the trajectory affect infrasonic signal amplitudes, in particular, as recently demonstrated by Pilger et al. (2015). Our work extends the Ens et al. (2012) study by using the NASA JPL fireball data which provides the ground-truth secondary characteristics of bolides, such as height, speed, and entry angle at peak brightness, to explore improvements and limitations in infrasound empirical relationships for bolides related specifically to infrasound period. We note that following Eq. 3.1 fireballs having the same total energy but different speeds will in general also show different blast radii and hence different periods and amplitudes at the ground.

3.3 Analysis Methodology

3.3.1 Infrasound Signal Database Construction

We constructed our bolide infrasound signal database cued by the location and timing of ground-truth data from the NASA JPL fireball website. These data, provided by U.S. government sensors, include time, location, height, velocity, total radiated energy, and calculated total impact energy. For each JPL bolide event with all these data, we searched for corresponding signals on infrasound stations of the IMS of the CTBTO. As a guide, we used a probable maximum detection range of:

$$R_{max} = 10^{(2.80+0.33\log E)}, \tag{3.7}$$

where R_{max} is maximum detection range in km and E is calculated total impact energy in tons of TNT (Ens et al., 2012). Each potential infrasound waveform from each station was processed using the InfraTool (Fig. 3.2) component of the analysis package Matseis (Harris and Young, 1997; Young et al., 2002) to isolate the likely bolide infrasound signal. The InfraTool display windows show the cross-correlation/Fisher F-statistic of waveforms, the trace velocity of the signal, the back azimuth of the waveform, and the waveform filtered by the given frequency bandpass as a function of time. Richard and Timothy (2000) showed that the MB2000, a typical infrasound microphone used at CTBTO stations, has a flat sensor response over 0.01 to 10 Hz. This implies that for signal periods less than 100 seconds (almost all events discussed in this chapter including the Chelyabinsk event), the sensor response is flat. The waveform was filtered using a second order Butterworth filter and we have varied the lower and upper cutoff frequency until a maximum signal to noise ratio is achieved. Coherent infrasound signals are first identified by the constant trace velocity and back azimuth values. If there is no signal, the trace velocity and back azimuth will be random because of the continuous fluctuations of pressure produced by winds and other background noise. In cases where the trace velocity and back azimuth change may be indistinct, the cross correlation maximum or the Fisher F-statistic maximum is used to identify the duration of the signal. Appropriate frequency bandpass and window parameters must be chosen in order to maximize the signal-to-noise ratio.

Once an infrasound signal is found, a toolkit termed “inframeasure”, which has specifically been developed for systematic bolide infrasound analysis was used to extract infrasound signal metrics. This process is developed and described in detail in Ens et al. (2012) which built upon the work of Edwards et al. (2006) where the core 7-step process was first employed. Details of the inframeasure methodology and 7-step process can be found in Appendix A section A.1.

Following this approach, we were able to identify a total of 179 individual infrasound station detections from 78 bolides having complete information on speed, height of peak bright-

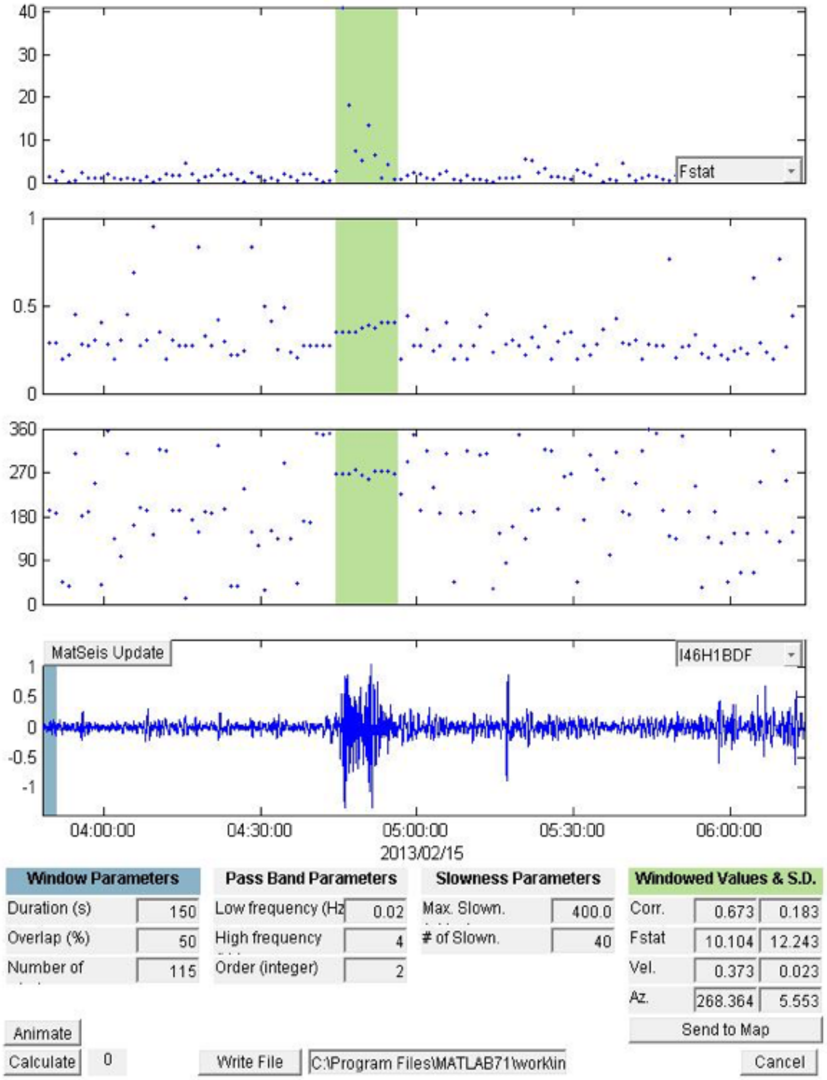

Window Parameters
Duration (s) 150
Overlap (%) 50
Number of 115

Pass Band Parameters
Low frequency (Hz 0.02
High frequency 4
Order (integer) 2

Slowness Parameters
Max. Slown. 400.0
# of Slown. 40

Windowed Values & S.D.
Corr. 0.673 0.183
Fstat 10.104 12.243
Vel. 0.373 0.023
Az. 268.364 5.553

Calculate 0
C:\Program Files\MATLAB71\work\in

Figure 3.2: An example screen from the InfraTool analysis package of Matseis (Harris and Young, 1997; Young et al., 2002) showing detection at IS46 for the Chelyabinsk fireball on February 15, 2013. The display window shows (from top to bottom) the F-statistic, trace velocity, back azimuth computed in time windows of 150 seconds duration with 50% overlap. The final (lowest) graph is raw pressure signal for the first array element. The green region represents the bolide signal where the F-statistic is above the background noise and where the trace velocity and the back azimuth are approximately constant, consistent with what is expected of a coherent infrasound signal.

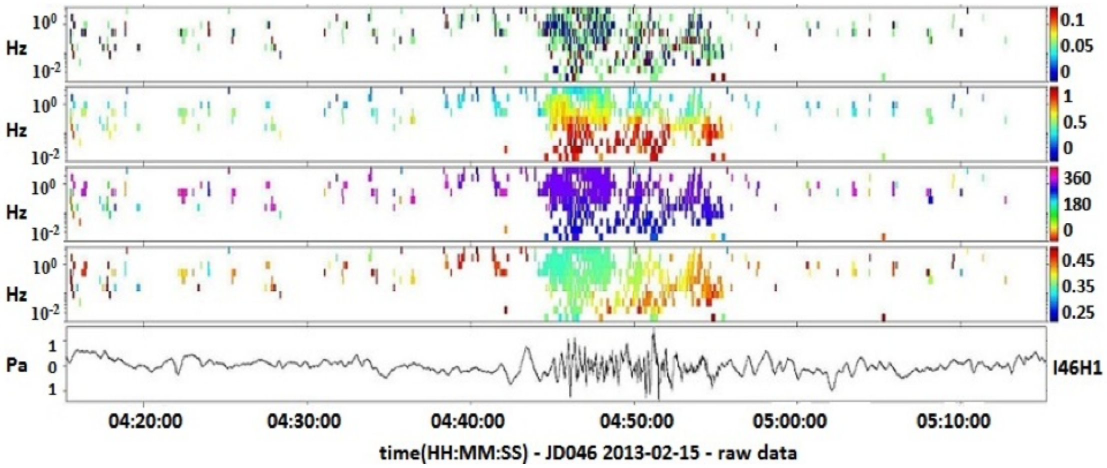

Figure 3.3: PMCC detection of the infrasound signal at IS46 for the Chelyabinsk fireball on February 15, 2013. The display window shows consistency, correlation, observed back azimuth, trace velocity of the signal, and the raw pressure signal for one of array elements. Details of the PMCC algorithm and its use can be found in Brachet et al. (2010).

ness and entry angle from 2006 to 2015. The detections use InfraTool supplemented with the Progressive Multi-Channel Correlation (PMCC) algorithm as described in Ens et al. (2012). PMCC is an array processing tool that detects coherent signals in frequency and time windows (Cansi, 1995) (Fig. 3.3). It is sensitive to signals with low signal-to-noise ratio.

3.3.2 Raytracing - GeoAc

We first explored the possibility of identifying source heights of bolide infrasound received at each station for select bolides having sufficient trajectory and light curve data through raytracing. Our goal was to find heights which match the observed signal characteristics (arrival times, back azimuth and arrival elevations) and check for self-consistency in terms of predicted periods at the ground using the known bolide light curve (and hence energy deposition) coupled with the ReVelle weak shock approach. For this purpose we used the GeoAc raytracing package (Blom, 2014) to extract possible eigenrays, which are individual rays from among a large starting test population of rays at the source which are found to arrive at a given receiver to within some user set distance threshold (in our case 0.1 km). GeoAc is a numerical package, which models linear acoustic propagation through the atmosphere. In this study, a 3D Range Dependent Global Propagation mode was used which computes ray paths in a three dimensional inhomogeneous atmosphere using spherical coordinates. The atmospheric profile including temperature, pressure, and wind was acquired from the UK meteorological office (UKMO) assimilated data for the altitudes from 0 - 60 km, and for the altitudes above 60 km the atmospheric profile was obtained from the Horizontal Wind Model (HWM) (Drob et al., 2015) and US Naval Research Laboratory Mass Spectrometer and Incoherent Scatter Radar (NRLMSIS)-00 model (Picone et al., 2002). The resulting atmospheric splining procedure follows Silber and Brown (2014). We found all eigenrays within all possible inclination ranges and one-degree azimuth windows centred around the great-circle azimuth connecting the bolide source location to the infrasound station (Fig. 3.4). Because of the large attenuation for thermospherically ducted rays, we are only interested in stratospherically ducted eigenrays. Once we obtained the arrival information for each eigenray, we compared the raytracing results with the observed quantities at the station including travel time, elevation angle, back azimuth and ballistic angle to identify the most probable source height.

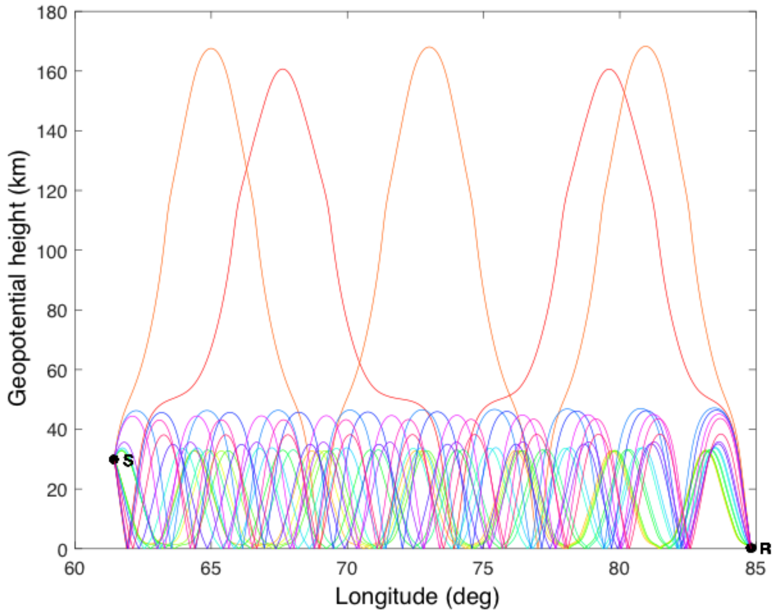

Figure 3.4: An example of a height - longitude cut along the great-circle path showing a raytracing plot with all eigenrays emitted from a source height of 30 km (left hand side of the plot) reaching the station IS46 for the Chelyabinsk event.

3.3.3 ReVelle Weak Shock Model

We adapted the ReVelle (1974, 1976) weak shock model to predict what the raytrace estimated source height should produce as a period at the ground in the direction of our measuring stations, given the known energy deposition for several bolides. The weak shock model is an analytical model that requires a set of input parameters characterizing the entry conditions of the meteoroid such as entry angle, trace velocity and blast radius. With the initial conditions, the weak shock model predicts at a given source height what the weak shock period should be at the ground in different directions. In this model, we have the following assumptions:

1. The meteoroid is spherically shaped single body and there is no fragmentation.
2. The trajectory is a straight line therefore gravitational effects are negligible.
3. Only rays that propagate downward and are direct arrivals are considered.
4. Once the transition height is reached (ReVelle, 1976) the wave period remains fixed.

According to the weak shock model, the shock wave reaches its fundamental period after travelling a distance of approximately ten times the blast radius. From this point, the shock wave propagates weakly nonlinearly. According to Towne (1967), the distortion distance (d') is the distance required for a wave to distort by 10% and calculated by

$$d' = \frac{C_s \tau}{34.3(\frac{\Delta P}{P_o})}, \tag{3.8}$$

where C_s is the speed of sound (m/s), τ is the signal period (s), and $\triangle P/P_o$ is the overpressure (Pa). Once the shock wave reaches the transition height, the shock is assumed to be in the linear regime ($d' \leq d_a$) where d_a is the remaining distance before a wave reaches the receiver. From this height, the shock propagates linearly and the period remains fixed (Fig. 3.5). This allows us to compare the predicted infrasound periods with observations. In particular, note that once the linear period is reached, within the assumptions of this model, we have "frozen" the period

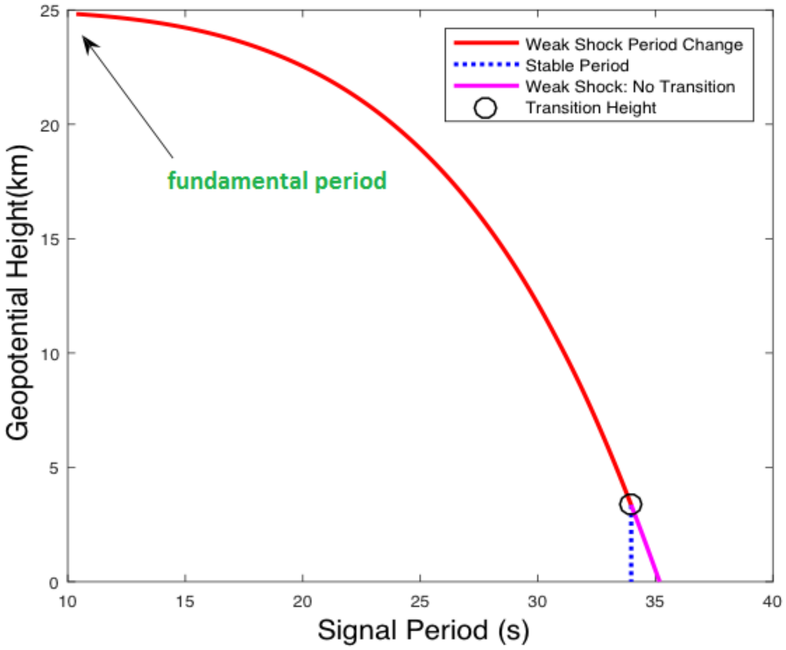

Figure 3.5: An example of the ReVelle weak shock model result for the February 15, 2013 Chelyabinsk event showing changes in signal period as a function of height in the direction of IS46. The source height was 25 km with blast radius 1.08 km. In this case, the theory predicts a signal period of 34 seconds.

so detectors at some larger distance will record the same period. In this sense it is possible to examine the predicted period at ranges beyond where direct arrivals only occur, though this is not possible for the amplitude.

3.4 Results and Discussion

3.4.1 Period-Yield Relation

For our study, we have analyzed 78 bolide events as detected from 179 individual infrasound stations from 2006 to 2015 of which 65 events detected from 156 infrasound stations are distinct from Ens et al. (2012). For events that were in common with Ens et al. (2012), we have independently completed inframeasure analysis to compare signal measurements. In a few cases we found some discrepancy between ours and Ens et al. (2012) signal measurements, thus we have re-analysed the bolide infrasound signal with inframeasure several times in order to choose the most appropriate bandpass (which we expect to show the largest SNR) and to remove the background noise. We combined our dataset (Appendix A Table A.1) with the Ens et al. (2012) 50 additional bolide events detected at 143 individual infrasound stations (Appendix A Table A.2) to compare with the period-yield relation from AFTAC ReVelle (1997). We also analyzed 37 bolide events that were detected at multiple-stations by taking the average of all signal periods detected at individual station and using one mean period per event. The regression to the combined dataset for all individual detections and multi-station detections were found to be respectively:

$$\log(E) = 3.68(\log\tau) - 1.99 \tag{3.9a}$$

$$\log(E) = 3.84(\log\bar{\tau}) - 2.21 \tag{3.9b}$$

where E is the source energy in kt of TNT, τ is the observed period at maximum amplitude in seconds, and $\bar{\tau}$ is the averaged signal period for a given event detected at different stations. The regression for the combined dataset was found to be very close to the AFTAC period-yield relation as shown in Fig. 3.6. For any single bolide event, different stations show a large spread in observed periods, similar to the spread in the original AFTAC nuclear explosion data. In principal, we expect a one to one relationship between the period and energy. However, bolides produce cylindrical line source shock along their entire trail (ReVelle, 1976), thus the period measured at each station can be different simply because returns correspond to the size of the cylindrical blast cavity at that particular segment of the trail having an acoustical path to each station. The actual length of segment of the trail that contributes to the signal is unclear since the length depends on non-linear bending near trail (Brown et al., 2007). So one possibility for this large variation is that signals are coming from different part of the bolide trail. Moreover we expect (in the absence of height effects) the line segment sampled at any one station to have an energy deposition only a small fraction of the total bolide energy.

Before exploring this source height effect in detail for specific cases, we first look at our

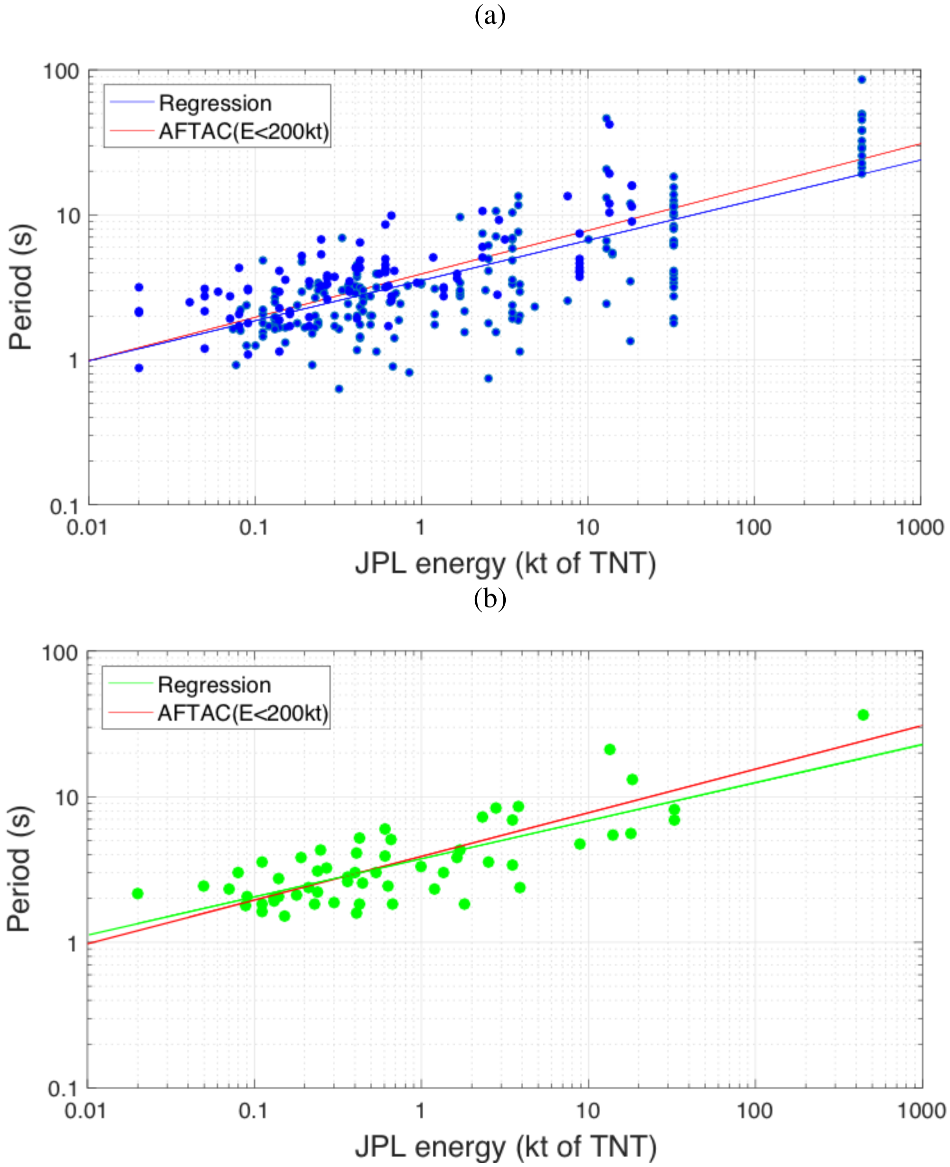

Figure 3.6: The infrasound signal period at the maximum amplitude as a function of bolide energy as given on the JPL webpage. (a) Each point represents the observed signal period at one particular station. (b) Each point represents the averaged signal period observed for a given event at different stations.

dataset as a whole. Fig. 3.7 shows the signal period at maximum amplitude as a function of JPL energy for multi-station events color coded by range (km) from the bolide location to different infrasound stations. Longer range stations show higher signal period; In Fig. 3.7 at fixed energy, there is a weak trend of larger periods at longer ranges. This trend is clearer especially for events > 1 kt of TNT. We expect the frequency dependent attenuation to remove

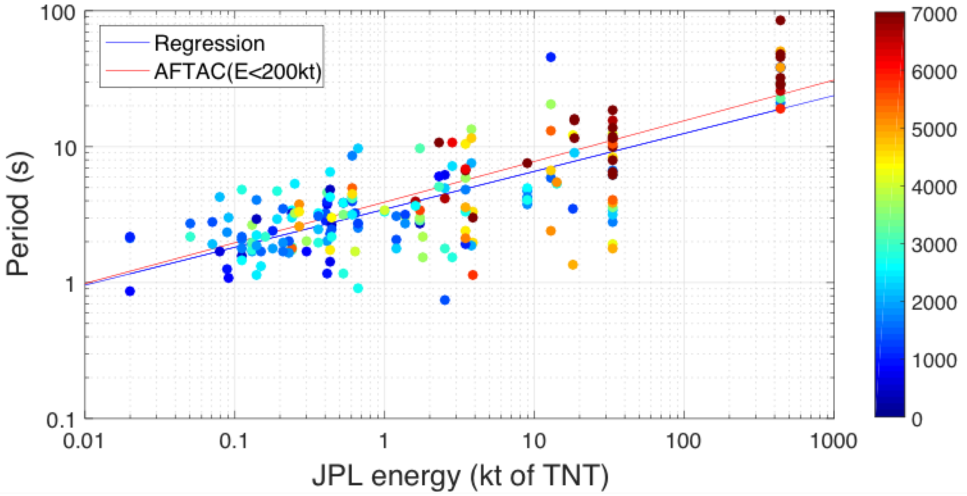

Figure 3.7: The signal period observed at different stations for multi-station bolide events as a function of JPL energy. Color represents the range (km) from the bolide location to the infrasound station.

higher frequencies with increasing propagation distance (e.g. Norris et al. 2010). This should tend to increase the signal period as the wave propagates further from the source, basically the effect we see in Fig. 3.7.

Fig. 3.8(a/b/c) shows the averaged signal period as a function of JPL energy with color coding for different bolide entry speeds (km/s), bolide heights (km) at peak brightness, and bolide entry angle (degrees). The speed itself is a variable that we do not expect to make a large difference to infrasound period; as expected we do not see any strong correlation. For a given small range in energy, all other things being equal, we would expect to see a vertical gradient in the points whereby the lowest heights show the smallest periods, if the infrasound signals at all stations were predominantly being emitted at the height of peak brightness. The height at peak brightness shows no such strong correlation, though the number statistics in this multi-station average are small (only 37 bolides). This implies that the location along the trail where peak brightness occurs is likely not where the infrasonic periods originate, that each stations sees a different part of the trail and/or the light curve for each event is quite different. No correlation was found between the infrasound signal period and the entry angle.

The simplest interpretation, that infrasound does not dominantly come from where the fire-

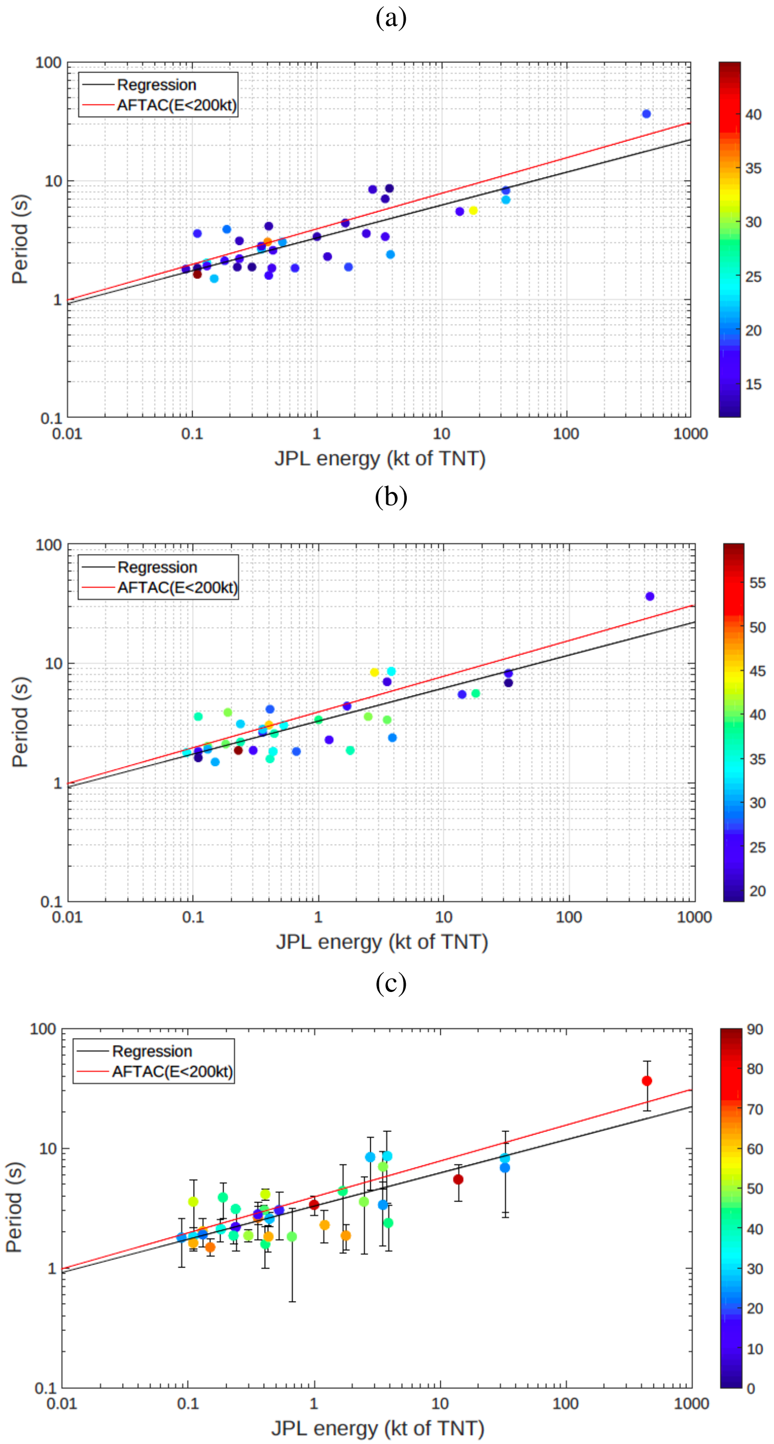

Figure 3.8: The averaged signal period observed at different stations for multi-station events as a function of JPL energy. (a) Color represents the speed (km/s) at peak brightness. (b) Color represents the height (km) at the peak brightness. (c) Color represents the entry angle (°) and the error bars the standard deviation among signal periods measured at the various stations per events.

ball is brightest, would imply either that individual station-bolide geometries dominant the process or that multiple fragmentation points at different locations in the stratospheric waveguide channel may play a larger role in funneling acoustic energy to a given station. We do not have sufficient information for most of these events to explore this further other than to conclude that burst height does not dominate the observed periods.

Pilger et al. (2015) found that station noise levels were the dominant factor in infrasound detection of the Chelyabinsk fireball. Motivated by that study, we also examined the possibility that the peak-to-peak amplitude signal to noise ratio (SNR) plays a significant role in the spread in signal period. As shown in Fig. 3.9, high SNR points are indeed more clustered along both the AFTAC period-yield relation and our regression to the bolide signal period directly weighed by signal to noise ratio. This trend is clearer as we increase the SNR cut-off value. We have measured the spread of the fit around the AFTAC period-yield relation by calculating the sum of squared residuals (SSR) and the value decreases as we increased the SNR cut-off value. This suggests that SNR is a contributing factor in the dispersion of periods. However, we see that even at high SNR individual events detected at different stations show some spread (though much less than is the case for low SNR station detections). This suggests a more explicit examination of the role of source heights and period is required for cases where sufficient information is available to allow such comparisons.

3.4.2 Bolide Infrasound Source Height Estimation: Case studies

To investigate in more detail the possibility that differing source heights may be responsible for the range of periods we investigate three bolides with well-documented trajectories and energy deposition curves.

The Chelyabinsk Fireball (February 15, 2013)

Our first case study event was the Chelyabinsk fireball, which occurred on February 15, 2013 at 3:20:33 UT over Chelyabinsk, Russia (Borovička et al., 2013; Brown et al., 2013;

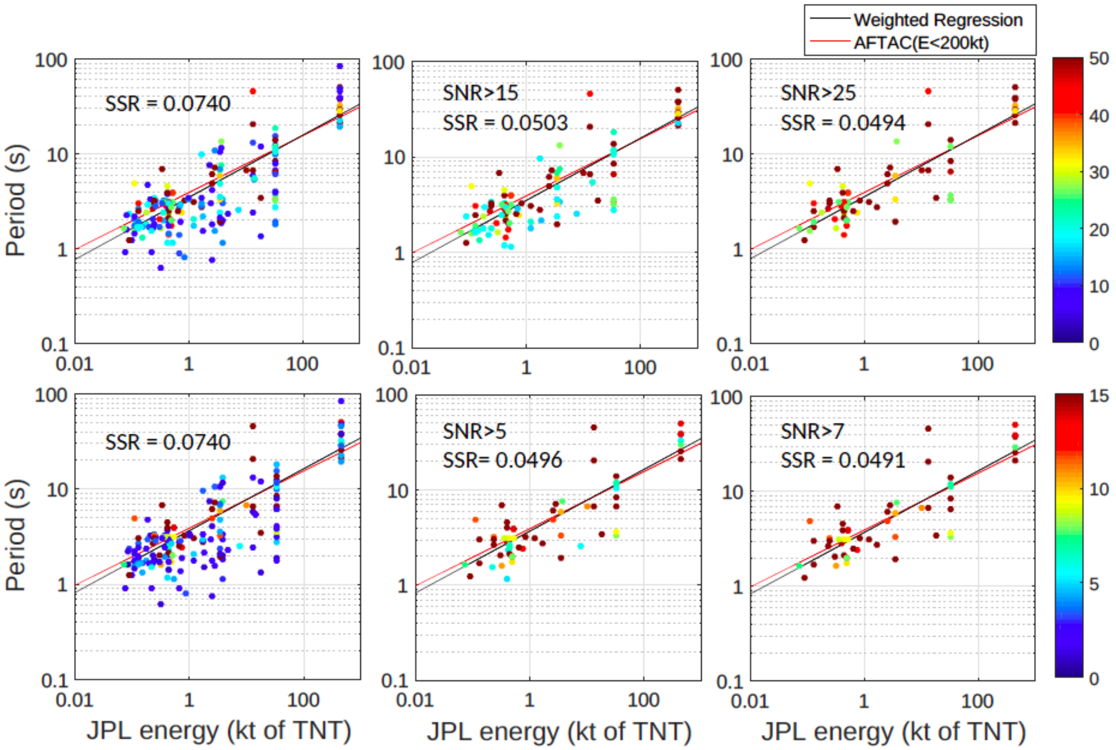

Figure 3.9: The signal period as a function of JPL energy for all station-bolide detections. The color coding of the upper row plots are the peak-to-peak amplitude signal to noise ratio (SNR) with two different cut off values, SNR>15 and SNR>25. The color of the bottom row plots are the integrated total bolide infrasound waveform energy signal to noise ratio (SNR) with two different cut off values, SNR>5 and SNR>7.

Popova et al., 2013). This unusually energetic event was detected at over twenty global infrasound stations. We focus on the nearest stations, knowing that our raytrace modelling becomes more uncertain with range.

We were not able to model any stratospherically ducted eigenrays reaching IS31, the closest infrasound station, potentially due to atmospheric uncertainties or counter-wind returns, which are notoriously difficult to model (de Groot-Hedlin et al., 2009). Thus we applied the raytracing-source height technique to the second closest station, IS46. We were able to find eigenrays to this station and established source height by comparing the raytracing model predictions to the observed parameters of signal travel time, elevation angle, back azimuth, and ballistic angle. The results are shown in Fig. 3.10. Using the travel time and the elevation angle, we isolated the most probable source height as 30 km. In this particular case, we could not

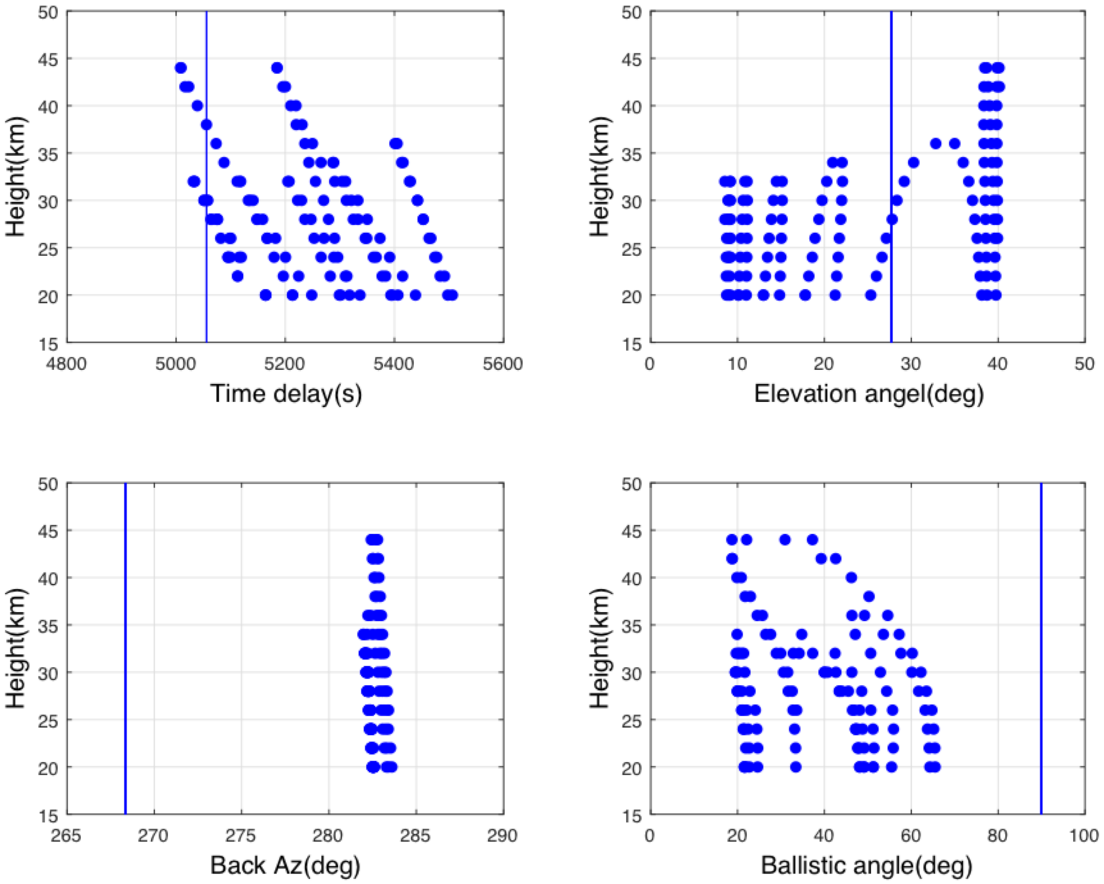

Figure 3.10: A composite plot showing the travel time (top left), elevation angle at arrival (top right), back azimuth at arrival (lower left) and ballistic angle (lower right) for the February 15, 2013, Chelyabinsk fireball event. The points represent each modelled arrivals from the raytracing at one km height intervals while the vertical solid line corresponds to the observed quantity from inframeasure analysis. The lower right plot shows the take-off angle for the ray from the source where the ballistic angle is the solid line at 90°, expected from a cylindrical line source.

distinguish source height based on the back azimuth, which shows a large deviation compared to other events (e.g. Ens et al. 2012 data showed azimuth agreement within 10 degrees). This significant deviation is possibly due to the turbulence or because the shock has relatively high amplitude thus, the wave front is more distorted and it is no longer a plane wave.

Having established ~30 km as the most probable source height using the raytracing method, we applied the ReVelle weak shock model. Using the energy deposition curve (Fig. 3.11), we calculated the blast radius as shown in Fig. 3.12. Chelyabinsk produced blast radii up to about 9.5 km at the expected source height 30 km, much larger than any other bolide with instrumental measurements. Unfortunately, this blast radius is comparable to or larger than the atmospheric scale height at this altitude, which invalidates one of the assumptions in the use of the ReVelle model.

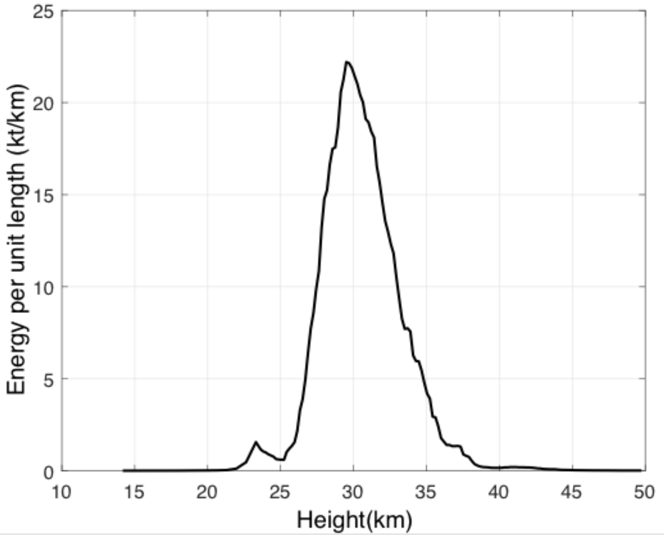

Figure 3.11: Energy deposition curve for the February 15, 2013 Chelyabinsk fireball taken from Brown et al. (2013).

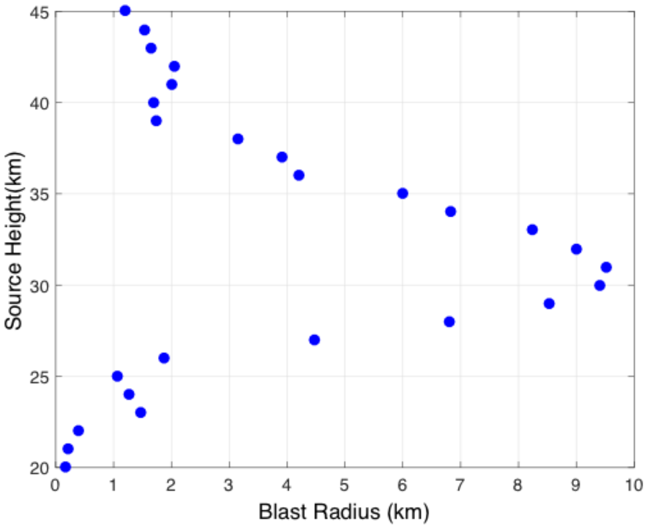

Figure 3.12: Equivalent blast radius plot for the February 15, 2013 Chelyabinsk fireball based on Fig. 3.11.

Fig. 3.13 shows the result from weak shock modeling with source height from 20 to 45 km as a function of signal period. In fact we see the greatest disagreement between the simulated signal period and the observed signal period at 30 km height. However, this disagreement is not significant because we are violating the assumption that the blast radius is much smaller than the scale height of the atmosphere implicit in the weak shock model. Therefore, we concluded that the period prediction for the ReVelle weak shock model is not valid for the Chelyabinsk event.

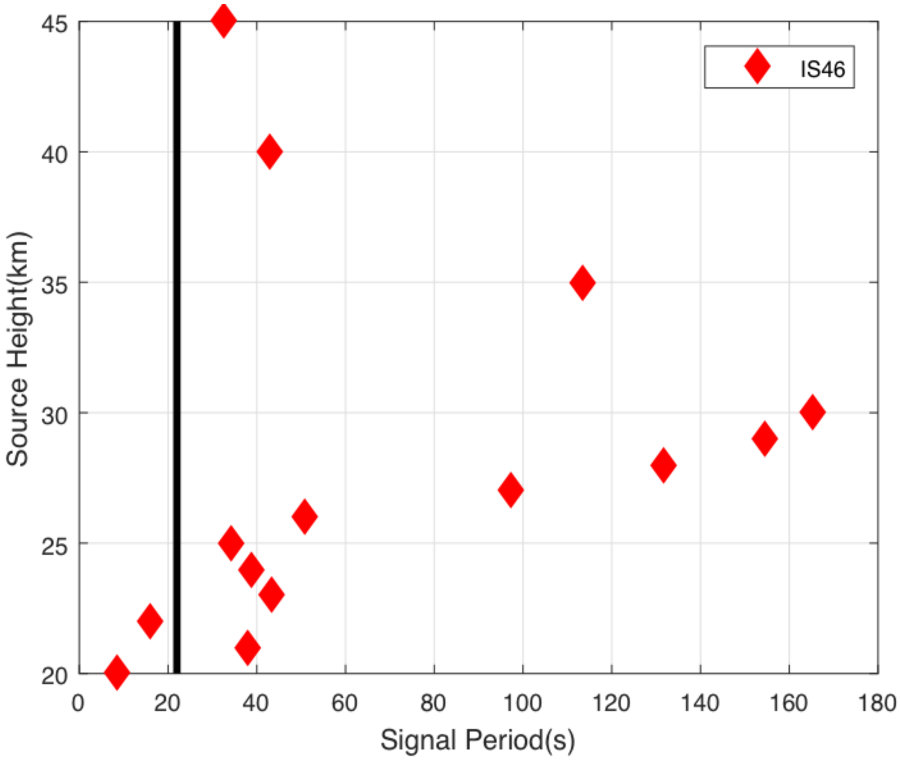

Figure 3.13: The signal period plot for the Chelyabinsk fireball of February 15, 2013. The diamonds represent simulated signal period from weak shock model and the solid line corresponds to the observed infrasonic signal period (see Table A.2 in Appendix A).

The Antarctica Fireball (September 3, 2004)

Our next case study was a fireball occurring near Antarctica on September 3, 2004 at 12:07:22 UT (67.64°S 18.83°E). This event was detected at three infrasound stations, IS27, IS55, and IS35 (Klekociuk et al., 2005). The details of infrasound measurements at each station can be found in the Table A.2 of Appendix A. From the U.S. government sensor observations, the total radiated energy is 7.26×10^{12} J suggesting total impact energy of 13 kT, using the Brown et al. (2002) optical energy-total calibrated energy relation. The light curve from Klekociuk et al. (2005) is shown in Fig. 3.14 and from the equivalent energy deposition curve, we generated blast radii as a function of height for the event as shown in Fig. 3.15.

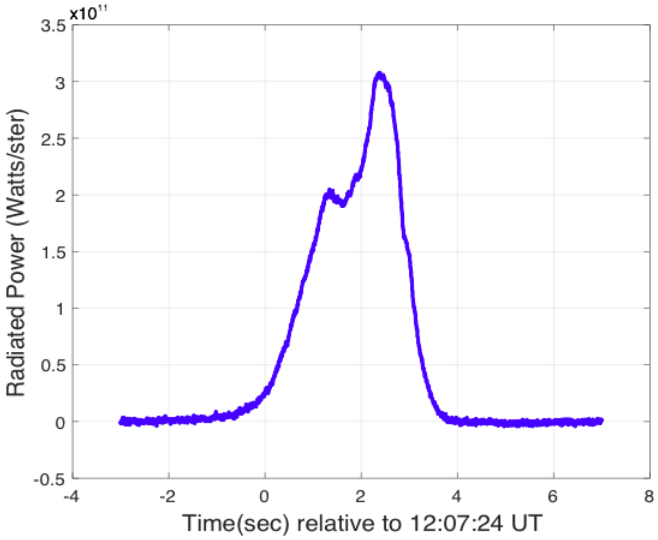

Figure 3.14: Light curve for the September 3, 2004 Antarctica fireball

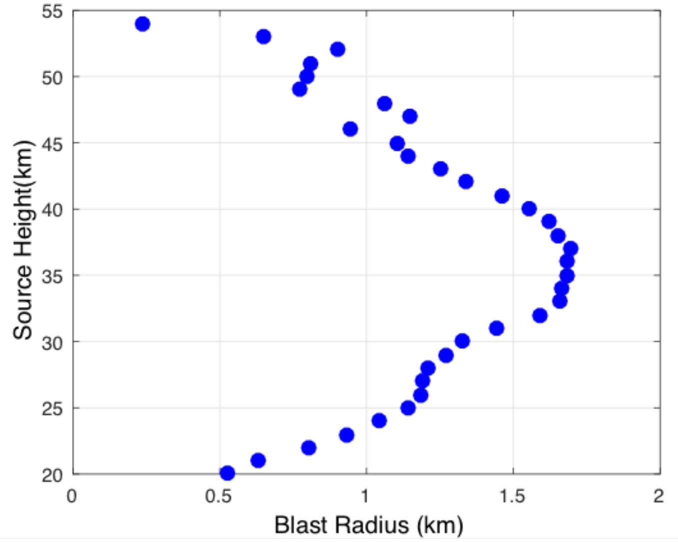

Figure 3.15: Blast radius plot for the September 3, 2004 Antarctica fireball

As with the Chelyabinsk event, we applied raytracing to isolate the most probable source heights from each station and then weak shock modelling to check the predicted period against the observed period. We were not able to find any stratospherically ducted eigenrays for the furthest station, IS35, so we only have raytracing results for the first two closest stations, IS27 and IS55. The results are shown in Fig. 3.16(a/b). For the IS27 composite plot, the elevation angle and back azimuth suggests that ~35 km is the source height though these are not strongly constrained solutions. This height is also consistent with the ballistic angle closest to 90°, consistent within uncertainty to a true ballistic arrival assuming some non-linear shock behaviour near the source (Brown et al., 2007). This is the most internally consistent height for a true cylindrical shock for this station. According to Brown et al. (2007) the angular deviation of ballistic angle can be up to 24 degrees. For this event, we see up to about 30 degrees deviation, which would not be unreasonable for such an energetic event where the shock is strongly non-linear for considerable distance from the trail and bending of the wave front may also be pronounced. In contrast, the IS55 composite plot, has a less well determined source height, with almost all heights showing one or two eigenray elevation arrivals agreeing with observations, while the back azimuth plot is uniformly at variance at all heights with observations. The ballistic arrival condition is met near 40 - 45 km height. As a whole, this does not suggest we can assign a unique source height to IS55 from raytracing alone.

We next applied the ReVelle weak shock model to this event, converting each blast radii as a function of height into the equivalent period expected for the geometry to the observing station. The results from all three infrasound stations are shown in Fig. 3.17. For the closest station, IS27, which also has the best estimate of source height (35 km), the observed and predicted signal period show good agreement for a source height of 35 km. However, while the periods at other stations are consistent with high altitude sources, we cannot assign unique source height based on raytracing results so these are less convincing.

(a) IS27

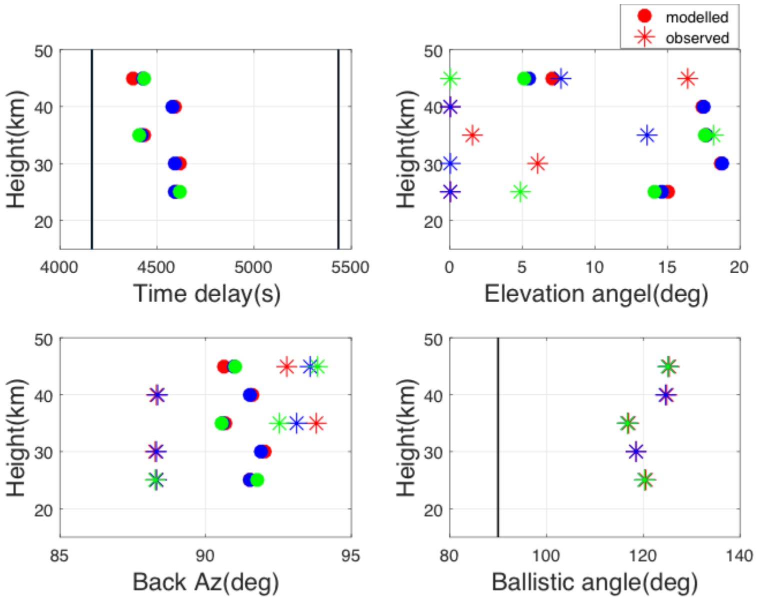

(b) IS55

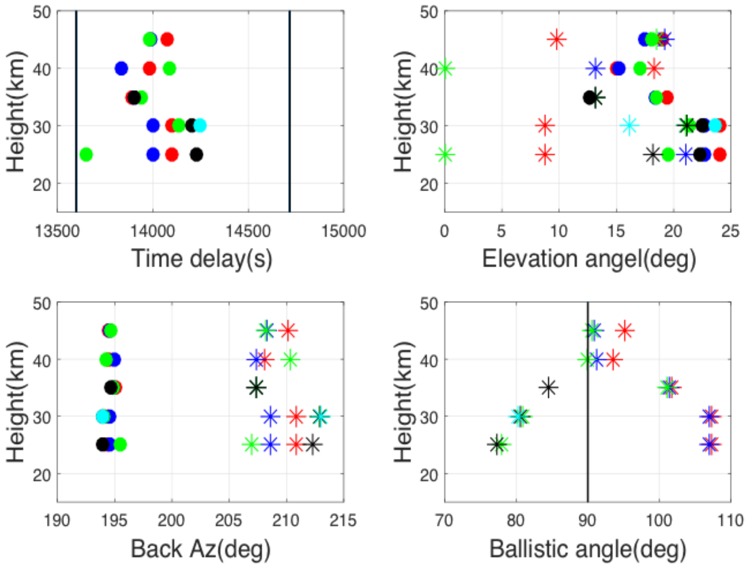

Figure 3.16: A composite plot showing the travel time with two vertical lines indicating where the signal starts and ends (top left), elevation angle at arrival times for the given eigenrays(top right), back azimuth at arrival for the given eigenrays (lower left) and ballistic angle of emission at the fireball trajectory (lower right) for eigenrays reaching each of IS27 (a) and IS55 (b) for the September 3, 2004, Antarctica fireball. The circles represent individual eigenrays from the modelled raytracing arrivals and asterisks are the observed quantity corresponding to the same colour circles at the modelled arrival times.

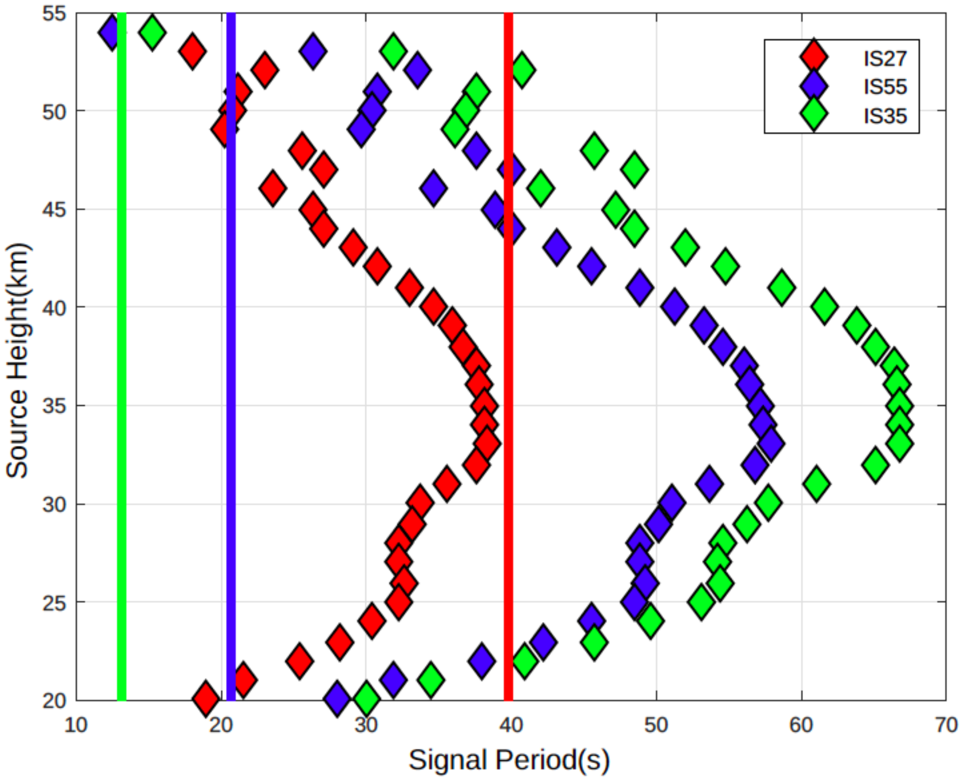

Figure 3.17: The signal period plot for the September 3, 2004, Antarctica fireball. The diamonds represent the simulated signal period from the weak shock model expected at the observing stations while the solid lines correspond to the observed infrasonic signal period (see Table A.2 in Appendix A). The different colors correspond to different infrasound stations with red, blue, green being IS27, IS55, IS35 respectively.

The Park Forest Fireball (March 27, 2003)

Our last case study event was the Park Forest fireball, which occurred on March 27, 2003 at 5:50 UT in Illinois, United States. The infrasound signal was detected at IS10 and at Blossom Point, Maryland, however, we will only be discussing the signal detected at the IS10 infrasound station, as the Blossom Point data is not publically available. According to Brown et al. (2004), the original total energy of this event was ~0.5 kT. To calculate the blast radii for the Park Forest event, we used same method as used to generate Fig. 3.15 for the Antarctica event. The blast radii graph can be found in Appendix A figure A.4. Raytracing results (Fig. 3.18) did not clearly indicate the source height, however ballistic angle suggests range of 15 - 30 km is the best source height presuming a cylindrical line source while the weak shock model (Fig. 3.19) is consistent with a height range of 20 - 25 km. We can see that there is overlap agreement between these two predictions and therefore, we can conclude that a source height in the range of 20 - 25 km is most probable.

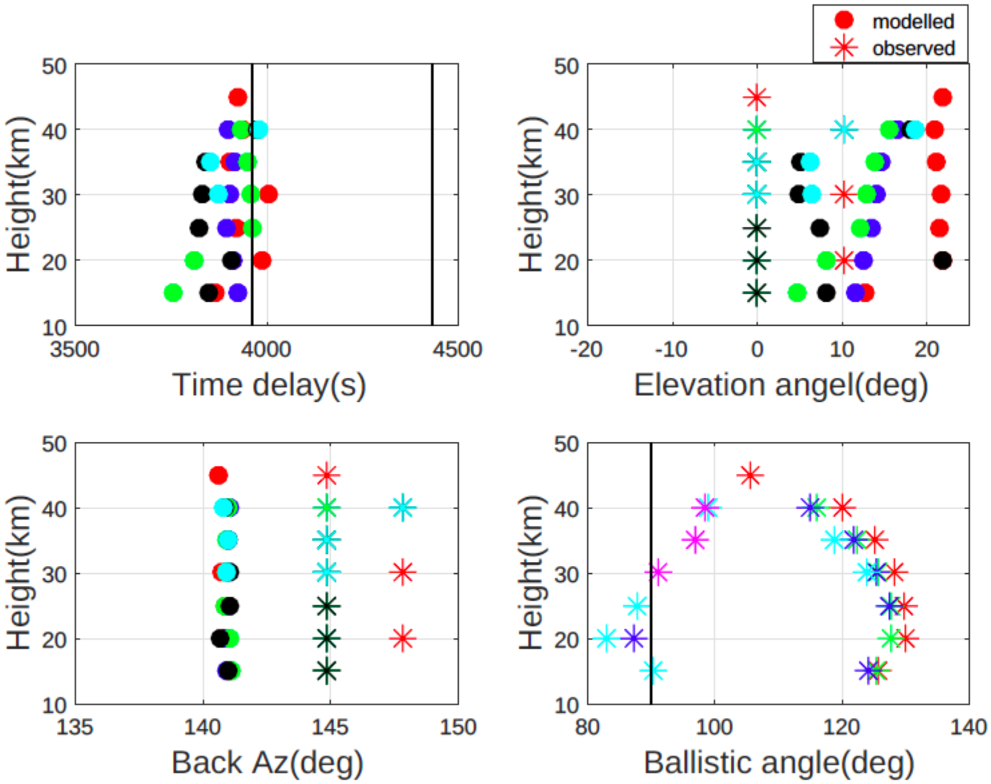

Figure 3.18: A composite plot for the Park Forest fireball infrasound showing the travel time with two vertical lines indicating where the signal starts and ends (top left), elevation angle at arrival (top right), back azimuth at arrival (lower left) and ballistic angle of emission at the fireball trajectory (lower right) for eigenrays reaching IS10. The circles represent individual eigenrays from the modelled raytracing arrivals and asterisks are the observed quantity corresponding to the same colour circles.

3.5 Conclusions

In this chapter, we extended the study of Edwards et al. (2006) and Ens et al. (2012) to examine the correlation between the infrasound signals and bolide characteristics, including entry angle, speed, height of peak brightness and range to station. Using a dataset consisting of 78 bolides detected by U.S. government sensors we have analyzed 179 individual infrasonic

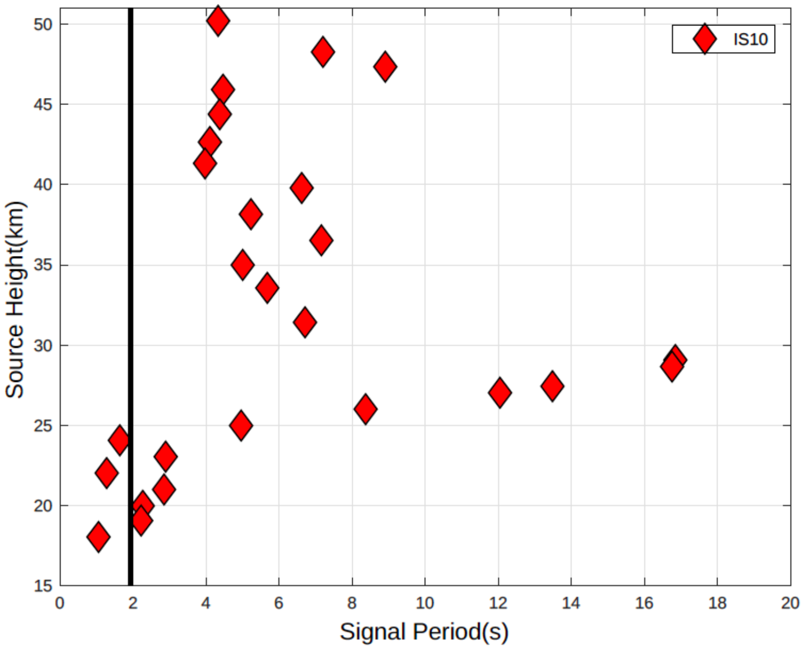

Figure 3.19: The signal period plot for the Park Forest meteorite dropping fireball of March 27, 2003. The diamonds represent simulated signal period from weak shock model and the solid line corresponds to the observed infrasonic signal period (see Table A.2 in Appendix A).

waveforms and have been able to establish an empirical quantitative relationship between observed infrasonic bolide periods and total bolide yield (Eq. 3.9). Our period-yield relation for averaged signal periods was found to be very close to the AFTAC period-yield relation derived from nuclear tests, as was also found by Ens et al. (2012).

We find that two effects show a correlation with interstation periods:

1. Station noise levels produce noticeable scatter in period measurements, suggesting this may be a contributing cause to some of the large scatter, particularly for low SNR recordings. This is consistent with the results from Golden et al. (2012) who found that the dominant frequency in some cases occurs within a broader plateau making period measurements imprecise.

2. Increasing range from the bolide (particularly for larger events) shows a correlation with increasing apparent period. This is expected based on the larger attenuation with range with increasing frequency.

It is notable that the original AFTAC data nuclear yield-period data (Fig. 3.1) show significant scatter and that both of the foregoing effects would apply equally to the AFTAC or bolide datasets.

No empirical correlation with height of peak bolide brightness or entry angle is found for averaged signal periods. We suggest this implies either that the location along the trail where peak brightness occurs is not where the infrasonic periods dominantly originate, that each station sees a different part of the trail and/or the light curve for each event is quite different. The non-uniformity of energy release along the trail may cause a change in the shape of the shock wave during propagation through interaction of shocks formed at different parts of the trail. This is another possibility as to why we do not see a strong dependence of signal period with the source height. We applied the raytracing method and the ReVelle (1974) weak shock model to three fireball events to critically investigate how the bolide secondary characteristics, especially the source height affect the infrasound signal period. The main results of our case studies were:

- The weak shock model cannot be applied when the bolide blast radius is comparable to or larger than the atmospheric scale height (as is the case for Chelyabinsk).
- For relatively short-range stations (< 1000 km), heights from raytracing and the weak shock model were generally in good agreement. We found self-consistent results for a source height of ~35 km for the measured infrasonic period at IS27 for the Antarctica event and 20 - 25 km height for the infrasound period detected at IS10 for the Park Forest fireball.
- For longer-range stations, or stations with non-ballistic arrivals, we were not able to isolate a self-consistent and unique source height from raytracing.

Our initial exploration is suggestive that source height may be at least part of the answer to station period spreads from bolide returns. However, the number of useable cases with sufficient information is too small to make any firm conclusions. More infrasonically detected bolides with complete energy deposition profiles (light curves) are required to test this hypothesis. It is clear, however, that much of the station period scatter is due to both station noise levels and range effects, probable explanations also for the scatter in AFTAC nuclear period measurements where differing source heights/locations are not an issue.

Finally, we note that the agreement between the bolide total yield-period relations and the AFTAC period-yield remains puzzling. Bolide yield from the U.S. government sensor data represents all initial energy of the impactor at the top of the atmosphere. In contrast, the period observed at the ground probes only the energy deposition per unit trail length at some point (or points) along the trail, which should skew the bolide yield curve to lower apparent periods compared to the total yield. However, a countervailing factor is that the bolide trail segments occur at higher altitudes than the AFTAC nuclear detonations and this artificially increases the apparent period. The fact that the AFTAC energy-period and the bolide energy-period relations agree may simply be a reflection of the near balancing effects of burst height and energy deposition per unit length. In cases where the signals are detected at large distances from the trajectory, the source could be considered as point-like. If the source is point-like and occurring near ground level we would expect to see agreement with the AFTAC energy-period relations. The dataset used in this chapter is provided in Table A.1 together with all the raw measurements from Ens et al. (2012) in Table A.2 in Appendix A section A.2. In total this represents 128 individual bolides measured at 267 infrasound stations.

Acknowledgements

The authors thank Olga Popova and one anonymous reviewer for the detailed reviews of the original manuscript. This work was supported by grants from the Canadian Research Chair program (950221865), the Natural Sciences and Engineering Research council of Canada (RGPIN-2016-04433) and Natural Resources Canada (3000624187) as well as NASA cooperative agreement NNX15AC94A.

Bibliography

Antolik, M., Ichinose, G., Creasey, J., and Clauter, D. (2014). Seismic and Infrasonic Analysis of the Major Bolide Event of 15 February 2013. *Seismological Research Letters*, 85(2):334–343.

Bedard, A. J. and Georges, T. M. (2000). Atmospheric infrasound. *Physics Today*, 53(3):32–37.

Blom, P. (2014). GeoAc: Numerical Tools to Model Acoustic Propagation in the Geometric Limit. Software, Los Alamos National Laboratory.

Borovička, J., Spurný, P., and Brown, P. (2015). Small Near-Earth Asteroids as a Source of Meteorites. In *Asteroids IV*, pages 257–280.

Borovička, J., Spurný, P., Brown, P., Wiegert, P., Kalenda, P., Clark, D., and Shrbený, L. (2013). The trajectory, structure and origin of the Chelyabinsk asteroidal impactor. *Nature*, 503:235–237.

Boslough, M., Brown, P., and Harris, A. W. (2015). Updated population and risk assessment for airbursts from near-earth objects (NEOS). In : 2015 IEEE Aerospace Conference, Big Sky, Montana, pages 1–12.

Bowman, J. R., Baker, G. E., and Bahavar, M. (2005). Ambient infrasound noise. *Geophysical Research Letters*, 32:L09803.

Brachet, N., Brown, D., Le Bras, R., Cansi, Y., Mialle, P., and Coyne, J. (2010). Monitoring the Earths Atmosphere with the Global IMS Infrasound Network. In *Infrasound Monitoring for Atmospheric Studies*, chapter 3, pages 77–118. Springer Science. Business Media B.V.

Brown, P., Pack, D., Edwards, W. N., ReVelle, D. O., Yoo, B. B., Spalding, R. E., and Tagliaferri, E. (2004). The orbit, atmospheric dynamics, and initial mass of the Park Forest meteorite. *Meteoritics and Planetary Science*, 39:1781–1796.

Brown, P., Spalding, R. E., ReVelle, D. O., Tagliaferri, E., and Worden, S. P. (2002). The flux of small near-Earth objects colliding with the Earth. *Nature*, 420:294–296.

Brown, P. G., Assink, J. D., Astiz, L., Blaauw, R., Boslough, M. B., Borovička, J., Brachet, N., Brown, D., Campbell-Brown, M., Ceranna, L., Cooke, W., de Groot-Hedlin, C., Drob, D. P., Edwards, W., Evers, L. G., Garces, M., Gill, J., Hedlin, M., Kingery, A., Laske, G., Le Pichon, A., Mialle, P., Moser, D. E., Saffer, A., Silber, E., Smets, P., Spalding, R. E., Spurný, P., Tagliaferri, E., Uren, D., Weryk, R. J., Whitaker, R., and Krzeminski, Z. (2013). A 500-kiloton airburst over Chelyabinsk and an enhanced hazard from small impactors. *Nature*, 503:238–241.

Brown, P. G., Dube, K., and Silber, E. (2014). Detecting NEO Impacts using the International Monitoring System. In *AAS/Division for Planetary Sciences Meeting Abstracts*, volume 46 of *AAS/Division for Planetary Sciences Meeting Abstracts*, page 403.02.

Brown, P. G., Edwards, W. N., Revelle, D. O., and Spurny, P. (2007). Acoustic analysis of shock production by very high-altitude meteors—I: infrasonic observations, dynamics and luminosity. *Journal of Atmospheric and Solar-Terrestrial Physics*, 69:600–620.

Brown, P. G., Wiegert, P., Clark, D., and Tagliaferri, E. (2015). Orbital and Physical Characteristics of Meter-sized Earth Impactors. In *AAS/Division for Planetary Sciences Meeting Abstracts*, volume 47 of *AAS/Division for Planetary Sciences Meeting Abstracts*, page 402.07.

Cansi, Y. (1995). An automatic seismic event processing for detection and location: The P.M.C.C. method. *Geophysical Research Letters*, 22:1021–1024.

Ceplecha, Z., Borovička, J., Elford, W. G., ReVelle, D. O., Hawkes, R. L., Porubčan, V., and Šimek, M. (1998). Meteor Phenomena and Bodies. *Space Science Reviews*, 84:327–471.

de Groot-Hedlin, C. D., Hedlin, M. A. H., and Drob, D. P. (2009). Atmospheric variability and infrasound monitoring. In *Infrasound Monitoring for Atmospheric Studies*, chapter 15, pages 475–507. Springer Science. Business Media B.V.

Drob, D. P., Emmert, J. T., Meriwether, J. W., Makela, J. J., Doornbos, E., Conde, M., Hernandez, G., Noto, J., Zawdie, K. A., McDonald, S. E., Huba, J. D., and Klenzing, J. H. (2015). An update to the Horizontal Wind Model (HWM): The quiet time thermosphere. *Earth and Space Science*, 2:301–319.

Edwards, W. N. (2010). Meteor generated infrasound : Theory and observation. In *Infrasound Monitoring for Atmospheric Studies*, chapter 12, pages 361–414. Springer Science. Business Media B.V.

Edwards, W. N., Brown, P. G., and ReVelle, D. O. (2005). Bolide Energy Estimates from Infrasonic measurements. *Earth, Moon and Planets*, 95:501–512.

Edwards, W. N., Brown, P. G., and ReVelle, D. O. (2006). Estimates of meteoroid kinetic energies from observations of infrasonic airwaves. *Journal of Atmospheric and Solar-Terrestrial Physics*, 68:1136–1160.

Ens, T. A., Brown, P. G., Edwards, W. N., and Silber, E. A. (2012). Infrasound production by bolides: A global statistical study. *Journal of Atmospheric and Solar-Terrestrial Physics*, 80:208–229.

Few, A. A. (1969). Power spectrum of thunder. *Journal of Geophysical Research*, 74:6926–6934.

Golden, P., Negraru, P., and Howard, J. (2012). Infrasound studies for yield estimation of he explosions. AFRL-RV-PS-TR-20120084. June 5th, 2012. Technical report.

Harris, M. and Young, C. (1997). MatSeis: a seismic GUI and tool-box for MATLAB. *Seismological Research Letters*, 68(2):267–269.

Herrin, G., Bass, H., Andre, B., Woodward, B., Drob, D., Hedlin, M., Garcs, M., Golden, P., Norris, D., de Groot-Hedlin, C., Walker, K., Szuberla, C., Whitaker, R., and Shields, D. (2008). High-altitude infrasound calibration experiments. In *Acoustic Today*, volume 4, pages 9–21.

Klekociuk, A. R., Brown, P. G., Pack, D. W., Revelle, D. O., Edwards, W. N., Spalding, R. E., Tagliaferri, E., Yoo, B. B., and Zagari, J. (2005). Meteoritic dust from the atmospheric disintegration of a large meteoroid. *Nature*, 436:1132–1135.

Norris, D., Gibson, R., and Bongiovanni, K. (2010). Numerical methods to model infrasonic propagation through realistic specifications of the atmosphere. In *Infrasound Monitoring for Atmospheric Studies*, chapter 17, pages 541–574. Springer Science. Business Media B.V.

Picone, J. M., Hedin, A. E., Drob, D. P., and Aikin, A. C. (2002). NRLMSISE-00 empirical model of the atmosphere: Statistical comparisons and scientific issues. *Journal of Geophysical Research: Space Physics*, 107(A12):15–16.

Pilger, C., Ceranna, L., Ross, J. O., Le Pichon, A., Mialle, P., and Garcés, M. A. (2015). CTBT infrasound network performance to detect the 2013 Russian fireball event. *Geophysical Research Letters*, 42:2523–2531.

Popova, O. P., Jenniskens, P., Emel'yanenko, V., Kartashova, A., Biryukov, E., Khaibrakhmanov, S., Shuvalov, V., Rybnov, Y., Dudorov, A., Grokhovsky, V. I., Badyukov, D. D., Yin, Q.-Z., Gural, P. S., Albers, J., Granvik, M., Evers, L. G., Kuiper, J., Kharlamov, V., Solovyov, A., Rusakov, Y. S., Korotkiy, S., Serdyuk, I., Korochantsev, A. V., Larionov, M. Y., Glazachev, D., Mayer, A. E., Gisler, G., Gladkovsky, S. V., Wimpenny, J., Sanborn, M. E., Yamakawa, A., Verosub, K. L., Rowland, D. J., Roeske, S., Botto, N. W., Friedrich, J. M., Zolensky, M. E., Le, L., Ross, D., Ziegler, K., Nakamura, T., Ahn, I., Lee, J. I., Zhou, Q., Li, X.-H., Li, Q.-L., Liu, Y., Tang, G.-Q., Hiroi, T., Sears, D., Weinstein, I. A., Vokhmintsev, A. S., Ishchenko, A. V., Schmitt-Kopplin, P., Hertkorn, N., Nagao, K., Haba, M. K., Komatsu, M., Mikouchi, T., and the Chelyabinsk Airburst Consortium (2013). Chelyabinsk Airburst, Damage Assessment, Meteorite Recovery, and Characterization. *Science*, 342:1069–1073.

ReVelle, D. O. (1974). *Acoustics of meteors-effects of the atmospheric temperature and wind structure on the sounds produced by meteors*. PhD thesis, Michigan University, Ann Arbor.

ReVelle, D. O. (1976). On meteor-generated infrasound. *Journal of Geophysical Research*, 81:1217–1230.

ReVelle, D. O. (1997). Historical Detection of Atmospheric Impacts by Large Bolides Using Acoustic-Gravity Waves. *Annals of the New York Academy of Sciences*, 822:284–302.

Richard, P. K. and Timothy, S. M. (2000). Infrasound sensor models and evaluation. Technical report, Sandia National Laboratories.

Silber, E. A. and Brown, P. G. (2014). Optical observations of meteors generating infrasound-I: Acoustic signal identification and phenomenology. *Journal of Atmospheric and Solar-Terrestrial Physics*, 119:116–128.

Silber, E. A., Brown, P. G., and Krzeminski, Z. (2015). Optical observations of meteors generating infrasound: Weak shock theory and validation. *Journal of Geophysical Research: Planets*, 120:413–428.

Silber, E. A., Le Pichon, A., and Brown, P. G. (2011). Infrasonic detection of a near-Earth object impact over Indonesia on 8 October 2009. *Geophysical Research Letters*, 38:L12201.

Silber, E. A., ReVelle, D. O., Brown, P. G., and Edwards, W. N. (2009). An estimate of the terrestrial influx of large meteoroids from infrasonic measurements. *Journal of Geophysical Research: Planets*, 114:E08006.

Stevens, J. L., Divnov, I. I., Adams, D. A., Murphy, J. R., and Bourchik, V. N. (2002). Constraints on Infrasound Scaling and Attenuation Relations from Soviet Explosion Data. *Pure and Applied Geophysics*, 159:1045–1062.

Towne, D. H. (1967). Wave Phenomena, Reading, Addison-Wesley Pub. Co., Massachusetts.

Tsikulin, M. A. (1970). Shock waves during the movement of large meteorites in the atmosphere (No. NIC-Trans-3148). Naval Intelligence Command Alexandria VA Translation Div.

Young, C. J., Chael, E. P., and Merchant, B. J. (2002). Version 1.7 of MatSeis and the GNEM R & E regional seismic analysis tools. 24th Seismic Research Review, pages 915–924.

Chapter 4

The Frequency of Window Damage Caused by Bolide Airbursts

A version of this chapter was submitted for a publication as:

Gi, N. and Brown, P. (2017) The frequency of window damage caused by bolide airbursts, *Meteoritics & Planetary Science*, Manuscript ID: MAPS-2805.

4.1 Introduction

Understanding the small (1 - 20 m) near-Earth objects (NEOs) population has become more important in recent years as the damage risk from these objects appears to be greater than previously thought (Chapman and Morrison, 1994; Brown et al., 2013). The estimated flux of small impactors suggests that a 1 m diameter object strikes Earth every 1 - 2 weeks, a 10 m object every 15 years while a 20 m diameter NEO is expected to collide with the Earth every 50 - 100 years (Brown et al., 2002a; Boslough et al., 2015; Harris and D'Abramo, 2015). For these small objects the atmosphere usually absorbs the majority of the initial energy and a ground-level airburst is avoided. In this size range, the ground damage caused by a bolide is most likely to be due to the airburst shock wave (Chapman and Morrison, 1994; Hills and Goda, 1998; Collins et al., 2005; Rumpf et al., 2017; Collins et al., 2017), which can result in a surface airblast sufficient to cause property damage and/or loss of life, should it occur over a populated area (Boslough and Crawford, 2008).

The February 15, 2013 airburst proximal to the city of Chelyabinsk in Russia, was the first recorded impact producing an air blast leading to window damage (Brown et al., 2013). The shock wave impacting the city caused in excess of $60 M in damage, mostly through breakage or cracking of windows (Popova et al., 2013).

As demonstrated by the Chelyabinsk event, at the lowest threshold where impactors are expected to just barely cause air blast damage at the ground, window breakage is the most likely damage modality. As the size-frequency distribution of impactors is a power-law, these are also the most likely events to occur. This problem is similar to the sonic boom threshold damage problem encountered in aeronautics (Clarkson and Mayes, 1972; Seaman, 1967). Prior to Chelyabinsk, however, studies of air blast damage from airbursts have focused on the ground footprint under the airburst where overpressure (ΔP) is very large. These works most often use the Hills and Goda (1998) criteria of the ground footprint where the ΔP exceeds 28 kPa (e.g. Collins et al. 2005; Toon et al. 1997), which is an overpressure at which trees are toppled and buildings seriously damaged.

The goal of our study is to quantify the expected incidence of window breakage from the ground level shocks (air blasts) produced by fireballs (airbursts). As discussed later, addressing this problem primarily requires knowledge of the height and magnitude of the energy deposition (edep) profile for an airburst.

There are two approaches to addressing this question.

The first, is to model in detail the ablation, fragmentation and subsequent edep of a hypothetical meteoroid and then propagate the resulting shock to the ground. This approach has been widely used employing both analytical models (Chyba et al., 1993; Hills and Goda, 1993, 1998; Collins et al., 2005) and numerical hydrocodes (Boslough and Crawford, 1997; Shuvalov and Trubetskaya, 2007). More recently, very high fidelity numerical entry models using detailed estimates of meteoroid strength and shock behaviour (Avramenko et al., 2014; Shuvalov et al., 2013; Register et al., 2017; Robertson and Mathias, 2017; Collins et al., 2017), have been validated against the observed ground-level ΔP from Chelyabinsk (Aftosmis et al., 2016).

Recently, Mathias et al. (2017) has merged modern entry models and blast models to produce a comprehensive global asteroid impact risk assessment incorporating all damage modalities using a Monte Carlo approach, while Collins et al. (2017) has done a similar analysis focused on blast wave damage alone. The advantage of these approaches is the ability to perform large numbers of realizations exploring wide swaths of parameter space to fully characterize damage modalities, limited only by the underlying physical assumptions of the numerical entry models.

A drawback of these “physics-first” approaches is the need to assume the properties and response to atmospheric entry of hypothetical meteoroids, notably strength and fragmentation behaviour, together with parameters which may require tuning and which subsequently drives the resulting edep profile.

A second approach to estimating the edep profile is to rely on empirical relationships to bound the solution space. This approach becomes particularly useful if we have airbursts for which some information is available (such as energy, speed and height at peak brightness). In such cases, we can reconstruct the edep profile using empirical estimates of peak brightness as a function of total energy and strength when coupled to a numerical entry model. Fortunately, such a dataset of fireballs has recently become available.

In this study, we adopt the second approach to present an empirically-focused analysis of how often fireballs may be expected to produce ΔPs at the ground sufficient to damage windows. We do this by simulating in detail a set of energetic fireballs (E > 2 kT) reported on the NASA Jet Propulsion Laboratory (JPL) website[1]. These data consist of over 600 bright fireballs recorded by U.S. Government sensors in the last 25 years. This data is collected by U.S. Government sensors which monitor Earth’s surface and atmosphere for events of interest, and is provided to NASA for scientific study of natural objects impacting the Earth.

---

[1] http://neo.jpl.nasa.gov/fireballs/

The specific fireballs chosen for our analysis can be found in Appendix B Table B.1. To be included in our dataset, an estimate of total fireball energy (which must be > 2 kT), velocity and height at peak brightness in addition to location must be reported. The JPL website does not explicitly report edep as a function of height.

To estimate edep as a function of height we will make use of a Monte Carlo numerical approach based on application of an analytic entry model, namely the Triggered Progressive Fragmentation Model (TPFM) of ReVelle (2005). Our aim is to reproduce as accurately as possible the maximum edep of each event, where we expect most of the damaging shock to originate. Using these estimates of the edep and its probable range for a given fireball, we couple the output of the TPFM model with an analytic weak shock model (ReVelle, 1976) to estimate the ΔP footprint on the ground.

In our approach, the edep profiles away from the peak are expected to be less accurately reproduced, but we anticipate this will not change the ΔP computed very much. To check this assumption and to validate our approach of generating model edep profiles from empirical relations, we will apply our generic approach to five well-constrained fireballs. These five fireballs are found among the JPL data, but in addition to the data given by that source other publications provide known trajectories, and (most importantly) observed light curves. These light curves are an indirect measurement of the fireball's associated edep.

These calibration fireball events are:

1. Feb 1, 1994 - the Marshall Islands fireball (Tagliaferri et al., 1995)
2. Jan 18, 2000 - the Tagish Lake fireball (Hildebrand et al., 2006; Brown et al., 2002b)
3. Mar 27, 2003 - the Park Forest fireball (Brown et al., 2004)
4. Sep 3, 2004 - the Antarctica fireball (Klekociuk et al., 2005)
5. Jul 23, 2008 - the Tajikistan superbolide (Konovalova et al., 2013)

For these five cases we can independently check our model edep profiles against the observed edep (light) curve.

For all fireball events in our study we have computed the area at ground-level where the ΔP is large enough to break windows. From this suite of ΔP-Area per unit time estimates, we then estimate the frequency with which we expect fireballs to produce window damage over urban areas on a global scale.

4.2 Background

4.2.1 Window Breakage - General Considerations

Window breakage is a significant damage mode in airblasts (Glasstone and Dolan, 1977). Injuries are commonly due to flying glass. In general, structural damage from airblasts is largely determined by the duration and amplitude of the blast wave (Needham, 2010). However, small and light structural elements, such as windows, require only a short period of vibration (up to ~0.05 sec) and small plastic deformation to break. Therefore, the breakage of window glass is mostly determined by peak ΔP, the maximum pressure caused by a blast wave above the ambient atmospheric pressure, without significant considerations needed for the duration of the blast wave (Glasstone and Dolan, 1977; Pritchard, 1981).

Window breakage is a complex process (Zhang and Hao, 2016). For a given shock geometry, ΔP and pulse duration, window failure depends on factors such as window thickness, area, method of attachment to frame, defect/microcrack density and damage history (Pritchard, 1981). Identically produced and mounted windows will not fail under the same conditions, because of microstructural variability (Hershey and Higgins, 1976). As a result, window breakage by airblasts is treated statistically with prediction models using empirical relations scaled to window thickness and area with various simplifications (Fletcher et al., 1980).

Impulse is another factor that can influence window damage levels. The ΔP-impulse diagram given by Gilbert et al. (1994) shows that at high charge weights (> 20 tonnes), ΔP is the only factor that determines structural damage. At low charge weights (< 0.5 tonnes), impulse is solely responsible for causing damage to structures. Between these two extremes, both ΔP and impulse need to be considered to estimate damage levels. However, as most of our fireball sources are comparatively large equivalent charges (on the order of kilotons of TNT), we will assume ΔP is the only feature of the airblast which needs to be considered in window damage. This is consistent with most past empirical studies of window breakage from large charges (cf. Reed, 1992). To get a simple estimate of the range of ΔP of interest, we will use a few empirical studies to bound the ΔP levels at which window damage may be expected to occur. We caution that the relation of window breakage probability to the ΔP adopted for our study is therefore simple, but we believe it is instructive to address the threshold level for a fireball at which damage may occur. It is worth noting in what follows that window damage can occur at lower ΔP levels if the windows are old or already stressed, and similarly, newer windows might survive at much higher ΔP levels.

4.2.2 Window Breakage Criteria

There have been a number of experimental studies giving quantitative estimates of the peak ΔP which causes window breakage both generally and as a function of thickness/area. Glasstone and Dolan (1977) provided a widely cited approximate ΔP range of 3.5 - 7 kPa for typical residential large and small glass window failure based on air blasts produced during nuclear tests. Clancey (1972) suggested that the peak ΔP for small window breakage to be 0.7 kPa while Kinney and Graham (1985) gave the range of typical window glass breakage as 1 - 1.5 kPa. Previous nuclear tests had shown that windows start to break at an ΔP of about 400 Pa, and this is the standard adopted in ANSI (1983).

However, a fundamental problem with these earlier studies is the lack of consideration for the size or thickness of windows. Fletcher et al. (1980) suggested a 50% probability of failure for most face-on windows lies between 0.6 - 6 kPa, showing explicit dependence on window area based on the experimental results of Iverson (1968).

In exploring all the literature on window breakage, we found one study in particular which used real-world data, explicitly included window sizes and was consistent with other studies. In this work, Reed (1992) derived empirical relations for predicting airblast damage to windows based on records of window breakage due to the 1963 Medina facility explosion, an accidental explosion of 50 tonnes of chemical high explosives near San Antonio, Texas. Reed (1992) explored the relationship between window breakage probability and incident ΔP for typical San Antonio window panes, which are taken to be a single-strength glass, 0.6 m x 0.6 m x 2 mm thick. Gilbert et al. (1994) derived a probit equation from the Reed (1992) relationship, namely:

$$Y = -4.77 + 1.09 ln \left(p_e^\circ\right), \tag{4.1}$$

where Y is the probit and p_e° is the peak effective ΔP (Pa) experienced by Reed's standard pane. We take the peak incident ΔP that would be required for other windows to break from the following equation of Gilbert et al. (1994):

$$p^\circ = \frac{p_e^\circ}{\left(\frac{A/0.372}{t/0.002}\right)}, \tag{4.2}$$

where p° is the peak incident ΔP (Pa), A is the pane area (m^2), and t is the glass thickness (m). Using Eq. 4.1 and 4.2, we have generated a plot (Fig. 4.1) showing the window breakage probability as a function of incident ΔP for typical window sizes in urban areas following Gilbert et al. (1994). We note that our range and breakage probability are broadly consistent with earlier studies, in particular it is comparable to changes in ΔP as a function of area values summarized in Fletcher et al. (1980).

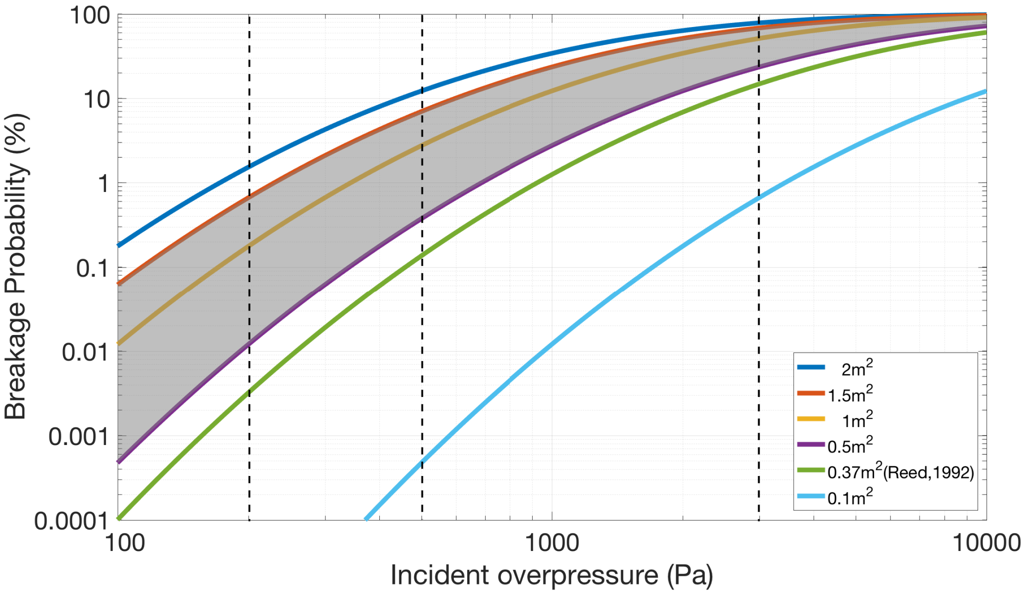

Figure 4.1: Window breakage probability as a function of incident ΔP for six typical window sizes in urban areas. Colored lines represent different window pane areas. The green line corresponds to the Reed (1992) single-strength glass (0.6 m x 0.6 m x 2 mm thick). The shaded region includes sizes representative of those found in most urban areas. Dashed vertical lines indicate reference incident ΔPs of 200 Pa, 500 Pa and 3 kPa. Note that based on the work of Fletcher et al. (1980) increasing the thickness from 2 mm to 6 mm increases the corresponding breakage ΔP curves by a factor of four.

4.2.3 Data for Window Breakage from the Chelyabinsk Airburst and Adopted Criteria

The February 15, 2013 Chelyabinsk airburst is the only fireball for which window damage was widely recorded. One challenge with estimating window breakage percentages is the rapid replacement of windows after the event due to the winter conditions at the time.

Brown et al. (2013) used videos from the time of the event or immediately after to attempt to quantify window damage and therefore remove any window replacement bias. They examined a total of 5415 windows in Chelyabinsk visible in videos with known geolocation. They categorized windows into four area groupings: A: 0 - 0.5 m^2, B: 0.5 - 1 m^2, C: 1 - 1.5 m^2, and D > 1.5 m^2. The majority of windows fell in categories B and C: 1810 (33%) windows being category B and 2258 (42%) windows being category C, corresponding to the shaded area in

Fig. 4.1. The average percentage of standard window breakage based on Eq. 4.1 and 4.2 is expected to be ~0.01 - 0.7% at 200 Pa, ~0.4 - 7% at 500 Pa, and ~25 - 60% at 3 kPa, the latter range being consistent with the weighted average of 20% breakage reported in Brown et al. (2013) for category B and C windows.

There was a strong variability across the city in window breakage, with some sections in the northern part of the city experiencing much larger breakage percentage, suggesting that local values may deviate by up to a factor of two from the nominally reported value near 3 kPa.

Independent estimates of the ΔP in Chelyabinsk are available from several sources. Brown et al. (2013) used the measured velocity of glass shards from several videos and empirical relations of ΔP versus expected shard speed to estimate a ΔP of 2.6 kPa. Avramenko et al. (2014) measured the apparent dynamic pressure of the air blast by the observed jump in lateral velocity of car exhaust in two videos to estimate an equivalent ΔP of 1.6 - 1.9 kPa.

Comparing these estimates to those obtained from our empirical window breakage relations (e.g. Fig. 4.1), we see a better than factor of two agreement. Given the variability in ΔP expected in an urban area due to reflections, caustics and large scale shock interference, this is remarkably consistent. We suggest that this confirms the basic validity of our adopted empirical relations.

As such, we adopt Fig. 4.1 as our baseline estimate to quantify window breakage. We will examine the areal footprint on the ground under our modelled airbursts where ΔPs exceed 200 Pa and 500 Pa, denoting these hereafter as $\Delta P(200)$ and $\Delta P(500)$ and describe them as light and heavy window damage thresholds respectively.

These two ΔP thresholds correspond approximately to the levels at which large windows (2 m^2) have a 1.5% and 12% breakage probability respectively. Similarly, standard urban windows (with $0.5 < A < 1.5$ m^2) would have a 0.01 - 0.7% and 0.4 - 7% probability of breakage for $\Delta P(200)$ and $\Delta P(500)$. In practical terms, these breakage probabilities bracket the ranges at which window damage from sonic booms are cited as producing damage claims in urban areas (Clarkson and Mayes, 1972).

4.3 Analysis Methodology

4.3.1 Triggered Progressive Fragmentation Model (TPFM)

To estimate ground-level ΔP, we must first estimate the edep for each fireball. Following ReVelle (2005) we use the analytic Triggered Progressive Fragmentation Model, which allows explicit inclusion of a simple fragmentation model once a bodies tensile strength is exceeded to simulate edep and ablation. Our approach attempts to best match the peak edep; heights above and below this point are expected to have poor (factor of several) discrepancies in modeled versus observed edep.

We briefly describe the TPFM model, our implementation, and choice of input parameters. More details can be found in Appendix B section B.2, ReVelle (2005) and references therein.

The model is based on analytically solving coupled differential equations for the meteoroid speed (Eq. 4.3a) and mass (Eq. 4.3b) to determine the height of the meteoroid as a function of its speed:

$$\frac{dv}{dt} = -\frac{\Gamma S \rho_a v^2}{m} \tag{4.3a}$$

$$\frac{dm}{dt} = -\frac{\Lambda S \rho_a v^3}{2\xi} \tag{4.3b}$$

where v is the meteoroid speed (km/s), m is the mass (kg), t is the time (s), ρ_a is the atmospheric density (kg/m^3), Γ is the drag coefficient, Λ is the heat transfer coefficient, S is the cross sectional area (m^2), and ξ is the meteoroid heat of ablation (ReVelle, 2005).

The model allows the ablation coefficient to change through variable drag, heat transfer coefficient and heat of ablation with height according to the flow regime, speed and material properties as described in ReVelle (1979) and modifications to that original approach outlined in ReVelle (2005). The atmosphere is a realistic, non-isothermal with the atmospheric mass density profile taken from the NRLMSIS-00 model of Picone et al. (2002) for the location and time of each simulated event.

Fragmentation for each simulation realization is randomly permitted to generate 0 to 1024 fragments, with each fragmentation episode doubling the number of fragments. In this manner, each time the dynamical pressure exceeds the meteoroid strength (specified in the simulation according to empirical criteria - see later), the meteoroid splits in half and the new fragment is assumed to ablate without any shielding effects from the leading fragment as described in ReVelle (2005).

Ablation is assumed to occur such that all fragments remain as spheres. Each succeeding fragment generation is assumed to have a higher strength, with the strength increment based on a Weibull distribution with the Weibull exponent chosen in the simulation randomly between values of 0.2 - 0.5 (Popova et al., 2011). Each simulation ceases when less than 1% of the original kinetic energy of the fireball remains. The resulting TPFM edep per unit path length output is then coupled with the ReVelle (1976) weak shock model to estimate ΔP on the ground.

The starting data used for our simulations is from the JPL fireball webpage which provides basic information on hundreds of real fireballs including in some cases entry angle, entry speed, height at the peak brightness, and total impact energy.

TPFM as a bolide ablation model computes mass loss, light production, and fragmentation associated with the atmospheric entry of fireballs. In general, the model input parameters are tuned to match the observed light curves and dynamics of fireballs. In these cases the TPFM fits may then provide estimates of the initial meteoroid properties including mass, porosity, strength, ablation rate and fragmentation behaviour. This forward modelling application of TPFM has already been applied to a number of past events (ReVelle, 2005, 2007; Brown et al., 2013).

In our study, we use each TPFM run as a single realization to try and match the available data from the JPL site of a particular fireball. For each fireball being simulated a number of input parameters are approximately known from JPL data (e.g. initial speed (km/s), entry angle (°), initial energy (kT)). Other parameters which are not known a priori are randomly chosen from broader distributions in a Monte Carlo sense (e.g. porosity, strength, number of fragments, increment in fragment strength). Table B.6 in Appendix B summarizes the input parameters, their sources and assumed statistical distributions.

This approach is used to produce a suite of 10,000 realizations. From this broad suite of model runs we chose a subset which also match empirical relations (see next section) and compute the corresponding range of edep to estimate median and maximum ΔP fields at the ground. At each point on the ground, we compute the largest ΔP and median ΔP among all accepted simulation runs and refer to these as maximum ΔP and median ΔP. From the array of maximum and median ΔP, we find the single point having the largest overpressure on the ground; we refer to these as a peak maximum ΔP and a peak median ΔP, respectively, throughout the chapter.

4.3.2 Empirical Constraints for TPFM

To select among our 10,000 simulations those which are most probable on physical grounds, we develop some empirical constraints from the population of bright bolides as a whole as a filter to select the most appropriate model runs. The first constraint is provided by the observational measurement of the height at peak brightness published on the JPL website. The height at peak brightness is known to have an accuracy of order 3 km from an earlier study where several JPL fireballs also observed from the ground were compared in detail (Brown et al., 2016). From that work, the measured height of peak brightness as a function of velocity for meter-sized impactors was determined as shown in Fig. 4.2a. This is equivalent to an estimate of the strength (calculated as the dynamic pressure for each object at its fragmentation height) as shown in Fig. 4.2b. The initial fragmentation occurs earlier than the point of peak brightness, so using the latter height provides an upper limit to the strength of the meteoroid (cf. Collins et al. 2017).

From TPFM modelling we find that we can match the height of peak brightness assuming the first fragmentation begins between one and two atmospheric scale heights above the height of peak brightness, depending on the number of assumed fragmentation episodes. While the

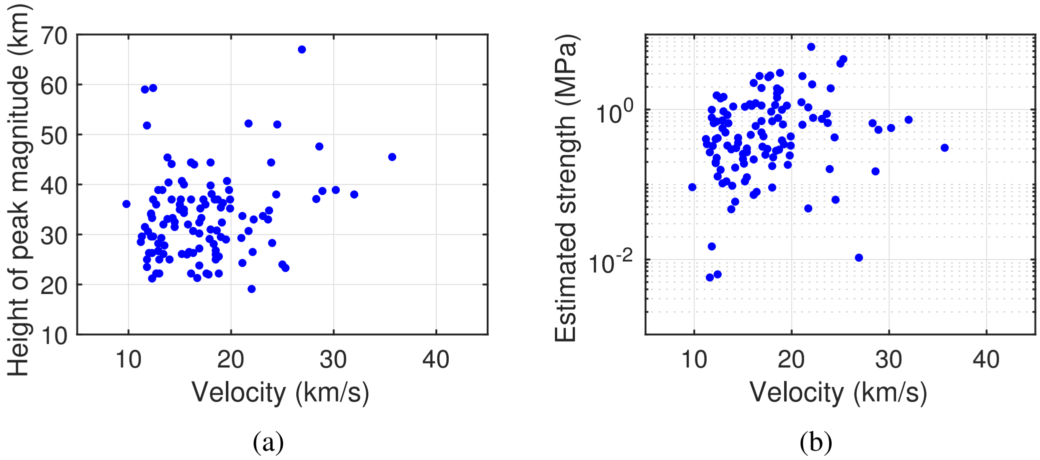

Figure 4.2: The distribution of (a) measured height of peak brightness and (b) the estimated strength based on this height (making the strength an upper limit to the global strength of the meteoroid) as a function of initial velocity for all meter-size objects (Brown et al., 2016).

global strength can be roughly matched in this manner, the fragmentation behaviour is still unspecified. We expect the height of peak brightness to correlate with the total energy of an event. The vertical spread in this correlation is a proxy for the degree of fragmentation.

Hence, to constrain the simulations further, we use the relationship between observed peak magnitude (radiated power) and total impact energy derived from the dataset reported in Brown et al. (2002a) as given in Brown (2016) and shown in Fig. 4.3. We require each realization to fall within the 2σ prediction intervals about the regression of Fig. 4.3. The best-fit regression to larger events (E > 1 kT) is given by

$$M_{peak} = -21.2 \pm 0.1 - (2.30 \pm 0.16)\log E, \tag{4.4}$$

where M_{peak} is the peak brightness and E is the total energy (kT). This peak brightness-energy filtering selects for model runs which have fragmentation behaviour physically similar to the meter-sized impactor population as a whole. We expect some deviation for very weak objects or objects entering at unusually shallow angles.

Finally, we also filter the model runs by requiring that the simulated total energy is within a factor of two of the JPL reported total impact energy based on modelling of the luminous effi-

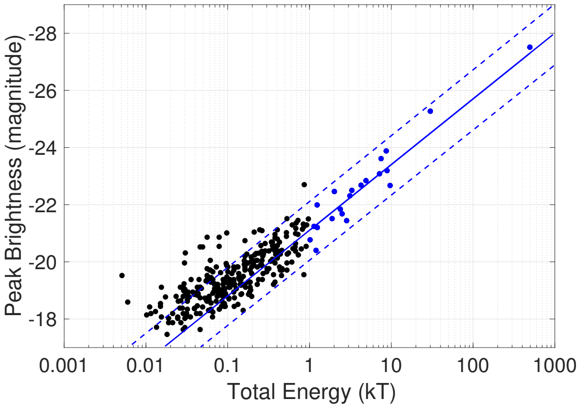

Figure 4.3: The distribution of measured peak brightness as a function of total impact energy (Brown, 2016). The dataset consists of 300 optical events from Brown et al. (2002a) and the Chelyabinsk event (~500 kT) from Brown et al. (2013). We see some deviation in the trend for smaller events (E < 1 kT). The blue solid line is a direct linear regression fit for events with E >1 kT also shown as blue circles. The blue dashed line shows the 2σ prediction interval about the regression.

ciency which shows a similar variation (Nemtchinov et al., 1997). An example of the resulting model plots of filtered runs (i.e. those which produce maxima within 3 km of the reported height at peak brightness, lie within the 2σ prediction interval of Fig. 4.3, and span a factor of two compared to the JPL reported energy) are shown in Appendix B section B.2.2 Fig. B.2.

This Monte Carlo simulation procedure is followed using the TPFM code one thousand times for each of the five calibration events and ten thousand times for each of the additional 18 JPL fireballs chosen for our study. These final filtered runs for each event provide an estimated range of edep as a function of height that form the basis of the input for the next step in the simulations; namely estimating the ΔP at the ground.

4.3.3 ReVelle Weak Shock Model

The intense edep produced along the bolide trail mimics a strong cylindrical line shock near the trail, decaying to a weak-shock and eventually to a linear acoustic wave (Edwards, 2010). This cylindrical shock propagates perpendicular to the meteoroid trajectory. To numerically map the footprint of the ΔP at the surface, we simulated a grid of points at the ground that follows this specular geometry (Fig. 4.4). These points were computed every 0.01 degrees in latitude and longitude at each 1 km increment in height along the fireball trajectory. Fig. 4.4 shows a limited number of such receiver points for ease of visualization.

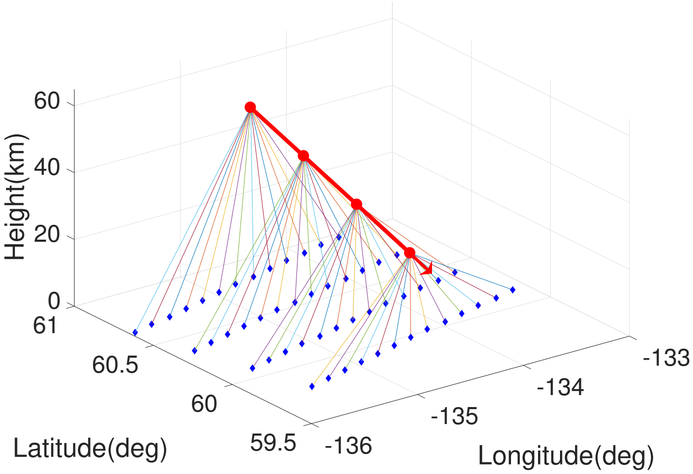

Figure 4.4: An example showing simulated weak-shock waves reaching a grid of receivers at the ground for the Tagish Lake fireball. The diagram has been simplified for better visualization. Red arrow is the bolide trajectory where red circles show 10 km interval height. Blue diamonds are the receiver points separated by 0.2 degrees.

To compute the expected ΔP at each receiver point, we adapted the ReVelle (1974, 1976) weak shock model to predict the ground ΔP, using as input the edep model outputs from the TPFM model for each fireball in our study. The ReVelle weak shock model was developed following earlier work on cylindrical shock waves (Sakurai, 1964; Jones et al., 1968; Few, 1969; Tsikulin, 1970). It is an analytical model that requires knowledge of the edep per unit length for the bolide and a known geometry between the trail and a receiver point on the ground to estimate ground ΔP. According to line source blast wave theory, the blast radius, (R_o) at any point along the trail, is defined as (Tsikulin, 1970):

$$R_o = \left(\frac{E_o}{P_o}\right)^{\frac{1}{2}}, \tag{4.5}$$

where E_o is the total energy per unit trail length (J/m) and P_o is the ambient hydrostatic atmospheric pressure (Pa) at the source height.

Physically, the blast radius is the distance from the center of the meteoroid trail to where the shock ΔP drops to roughly the ambient background pressure. It corresponds to the distance away from the meteoroid trajectory where the expansion work done by the shock to move the surrounding atmosphere equals the deposited explosion energy (Few, 1969). We assume that the shock propagates to the ground as a weak-shock and does not undergo a transition to linearity. This is a good approximation as shown by Silber et al. (2015) and appropriate to our short ranges for the large energy fireballs of our case study. Note that if we assume transition to linearity our estimated ΔP would increase in all cases, so this assumption makes our ΔP conservative. Details of the algorithms can be found in ReVelle (1974, 1976), Edwards (2010), and Silber et al. (2015).

4.4 Results

4.4.1 Empirical Modelling: Five Calibration Case Studies

Our modelling approach is designed to estimate peak edep for fireballs where only the height of peak brightness, speed, entry angle and total energy are known. Early or late portions of the bolide entry are entirely unconstrained and we do not expect our approach to produce matches in these parts of the trajectory.

However, we first need to demonstrate that the Monte Carlo TPFM approach with our empirical constraints produces peak edep values similar to observations. Validation of our modelling approach uses five well-documented fireball events, for which we have JPL data, trajectories, as well as the complete observed light curves. The data for these five fireballs are summarized in Table 4.1.

The observed light curve for each case study is equivalent to an edep curve (assuming a luminous efficiency) which can then be compared to the edep curve produced through our simulated TPFM Monte Carlo runs. The light curve data for each bolide and the details of the luminous efficiency conversion used to produce the edep profiles can be found in Appendix

	Marshall Islands	Tagish Lake	Park Forest	Antarctica	Tajikistan
Date	1994.02.01	2000.01.18	2003.03.27	2004.09.03	2008.07.23
Time (UT)	22:30	16:43	5:50	12:07	14:45
Location	Pacific Ocean (2.7, 164.1)	Canada (60.3, -134.6)	US (41.4, -87.7)	Antarctica (-67.7, 18.8)	Tajikistan (38.6, 68.0)
JPL energy (kT)	30	2.4	0.41	13	0.36
Speed (km/s)	25	15.8	19.5	13	14.3
Entry angle (°)	45.4	17.8	61	41.9	80
Radiant azimuth (°)	299.6	150.7	21	82.1	278.0
Mass(kg)	4.2×10^5	8.0×10^4	9.0×10^3	6.4×10^5	1.5×10^4
Radius(m)	3.1	2.3	0.9	3.5	1.0
Density (kg/m^{-3})	3500	1640	3400	3500	3500
Light curve extracted from	Tagliaferri et al., 1995	Brown et al., 2002(b)	Brown et al., 2004	Klekociuk et al., 2005	Konovalova et al., 2013

Table 4.1: Summary of bolide data for five calibration fireball case studies. Time, location, and energy were taken from NASA JPL fireball website. Speed, entry angle, and radiant azimuth are from the given reference from which the light curve was also extracted. The bolide mass was determined using the JPL estimated kinetic energy derived from the integrated luminous power. The meteoroid radius was computed using the volume of a sphere, where we assume a typical mass density for chondritic meteorites as ρ=3,500 kg/m^{-3}, except for the Tagish Lake and the Park Forest fireballs where the actual bulk density for the recovered meteorites was used. Tagish Lake was classified as a C2 carbonaceous chondrite (Hildebrand et al., 2006) and Park Forest as an L5 chondrite (Brown et al., 2004).

B section B.3. For each of these calibration fireball events, the TPFM model fit to the observed edep curve and the resulting predicted ground-level maximum ΔP plot are shown. The predicted median and standard deviation ΔP plots for each of the 5 events can be found in Appendix B section B.4. As mentioned earlier, maximum ΔP refers to the largest ΔP at any ground point computed from the ensemble of all simulations which met our empirical criteria. Similarly, median ΔP was calculated from the median of all accepted simulation runs.

Note that we have no direct measurements of the ΔP in these cases so cannot extend the validation to ΔP these five events. We note a similar procedure was used for the Chelyabinsk fireball (including use of the TPFM model and the ReVelle (1976) weak shock code) and the match was very good (Brown et al., 2013) in the centre of Chelyabinsk, though the technique is unable to estimate the largest ΔP for Chelyabinsk directly beneath the fireball due to the large blast radius.

We briefly describe these five calibration fireball events and compare our resulting modelled edep profile fits to the observations. More details of the modelling of each of these events can be found in Appendix B section B.4.

The February 1, 1994 Marshall Islands Fireball

This fireball occurred over the South Pacific and penetrated to a comparatively low altitude, reaching peak brightness at a height of 21 km. It is among the four largest energy events recorded by U.S. Government sensors in the last 25 years. For this first event, the TPFM model runs match well with the observed edep curve as shown in Fig. 4.5. The observed edep curve

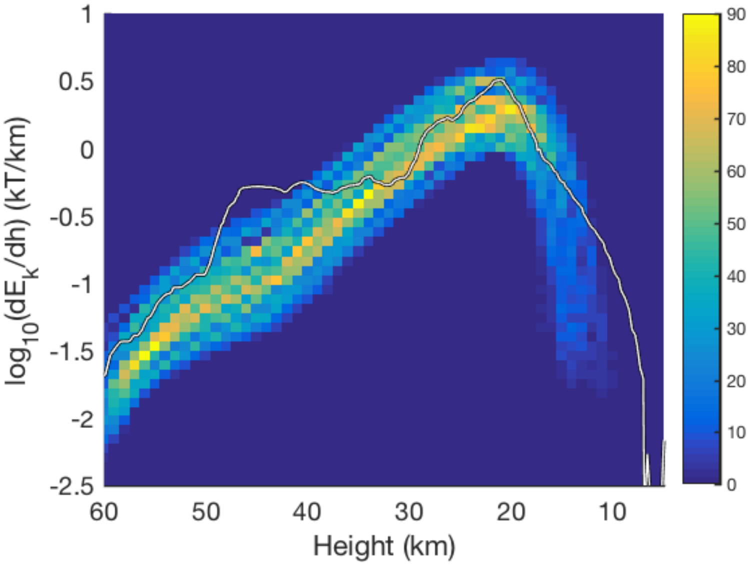

Figure 4.5: The TPFM model fits to the observed edep curve for the Marshall Islands fireball. Out of 1000 simulated runs, we found 45 that match all of our empirical correlations and known observational constraints. All of the accepted model runs are plotted. The colorbar represents the number of edep-height pairs that overlap in a particular pixel, where yellow shows highly populated number of runs clustered together. For the filtered simulated runs, the best-fit average initial mass was $4.2\pm1.5\times10^5$ kg, the average initial radius was 3.2 ± 0.5 m, and the average energy of 30 kT. This compares well with model results from Nemtchinov et al. (1997) who obtained a mass of 4×10^5 kg and an energy near 31 kT as well as a radius of 3.1 m using an analytic single-body pancake-type ablation model.

depicts two peaks as the meteoroid undergoes explosive disintegration at heights of 34 km and 21 km. The disintegration at 34 km is not well reproduced with the model runs, however the major disintegration at 21 km is in good agreement with the model. The peak brightness occurs where the peak edep occurs. We assume that the peak ΔP is dominated by the peak edep. Therefore, in this run as with all our other simulations, we only aim to match the peak of model runs with the major peak of the observed edep curve.

When a second edep local peak occurs at a height above the peak edep, the shock wave propagates downward and attenuates significantly, thus, does not have much of an effect on the ground ΔP. However, if there is significant edep at a height below the peak edep height, this could be a source of uncertainty in determining the ΔP. In that case, some of our estimates could be lower bounds.

The resulting predicted ground-level maximum ΔP is shown in Fig. 4.6. The model peak maximum ΔP is 740 Pa while the median ΔP is 500 Pa. These values bracket the observed light curve equivalent ΔP value of 590 Pa. The $\Delta P(500)$ is about 1300 km^2 as indicated by the dashed line in Fig. 4.6. For comparison, at 500 Pa, typical sized windows (0.5 - 1.5 m^2) start

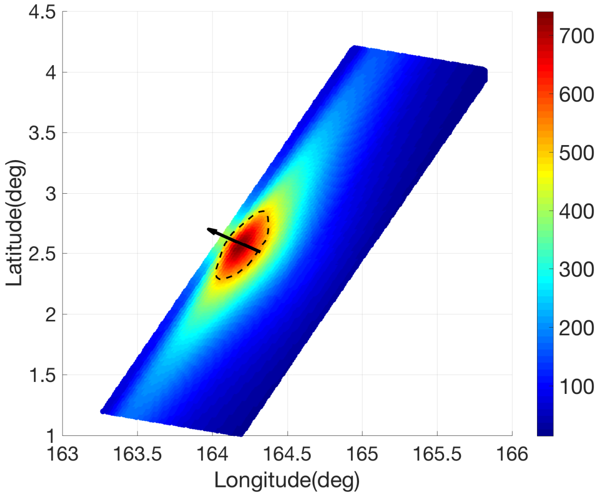

Figure 4.6: The model predicted ground-level maximum weak shock ΔP (Pa) for the Marshall Islands fireball. The arrow represents the bolide trajectory from an altitude of 60 km to 10 km moving northwest. The colormap shows ground points reachable by the cylindrical shock during ablation between 60 and 10 km altitude at 1 km increments. The colorbar represents the ΔP and the dashed line shows the boundary inside of which the ΔP exceeded 500 Pa.

to break at probability levels of ~0.4 - 7%. Large size windows (2 m^2) would have a breakage probability of ~12% at this pressure.

The January 18, 2000 Tagish Lake Fireball

This fireball occurred over northern Canada dropping C2 (ungrouped) meteorites on the frozen surface of Tagish Lake (Brown et al., 2000). The satellite optical light curve from Brown et al. (2002b) was digitized and used to compare with our Monte Carlo TPFM model. The TPFM model fit to the observed edep curve is shown in Fig. 4.7. The simulated runs do not reproduce the early light curve peak, but are a reasonable match to the lower altitude main light curve peak, which is our focus for ground level ΔP estimates.

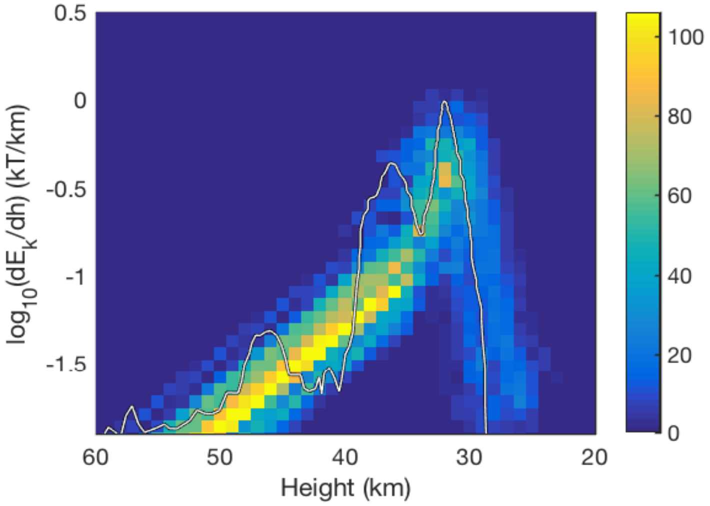

Figure 4.7: The TPFM model fit to the observed edep curve for the Tagish Lake fireball. Out of 1000 simulated runs, we found 53 that match all of our empirical correlations and observational constraints. For the simulated runs, the average mass was $9.48 \pm 3.2 \times 10^4$ kg, the average radius was 2.4±0.3 m, with an average energy of 2.8 kT.

We found that the average physical property values used in our model runs (as shown in Table 4.1) were very close to the initial physical properties of the meteoroid estimated in other studies. Hildebrand et al. (2006) bracketed the initial mass for Tagish Lake as between 6 - 9 $\times 10^4$ kg based on short-lived radionuclide activities in recovered samples, while Brown et al. (2002b) estimated a mass of 5.6×10^4 kg from entry modelling. ReVelle (2005) applied the

TPFM and forward modelling to estimate an initial mass of 1.5×10^5 kg while Popova and Nemtchinov (2000) applied a single-body analytic pancake-type model to estimate an initial mass of 50 - 200 tonnes. These are all comparable to within a factor of two of our modelled mean initial mass of 9.5×10^4 kg.

The predicted ground-level maximum ΔP is shown in Fig. 4.8 with the $\Delta P(200)$ of 1200 km^2 bounded by a dotted line. The modeled peak maximum ΔP is 240 Pa, very close to the light curve-derived value of 230 Pa. This event is an order of magnitude less energetic than the Marshall Islands fireball and has a higher altitude maximum edep. At 200 Pa, typical windows have a breakage probability between ~0.01 - 0.7%. Though this event occurred over land, only a few structures were within the 200 Pa contour, so the lack of reported window damage is unsurprising.

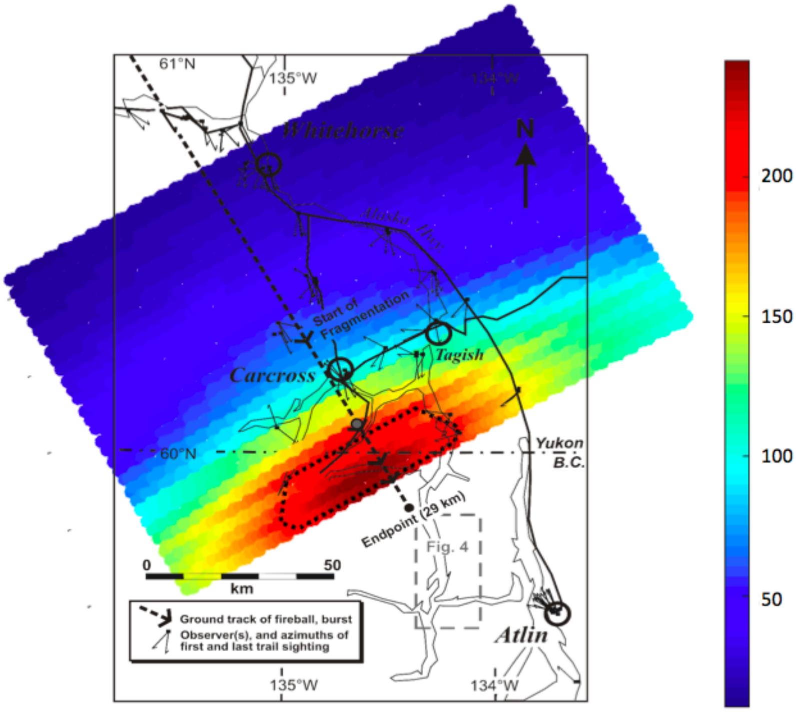

Figure 4.8: The predicted ground-level maximum weak shock ΔP (Pa) for the Tagish Lake fireball. The overlay map was taken from Hildebrand et al. (2006). In the map, the meteor moves southeastward, as shown with the dashed arrow line. The colormap shows all the ground points reachable by the ballistic shock emanating from the trail between heights of 60 - 29 km. The dotted line shows the boundary where our predicted ΔP exceeds 200 Pa.

The March 27, 2003 Park Forest Fireball

This was the second lowest energy of all our calibration events, but of particular interest because it produced a large shower of L5 meteorites in an urban area (Simon et al., 2004). The Park Forest meteorite fall is likely the largest meteorite shower to occur in a modern urban setting.

Fig. 4.9 shows the TPFM simulated runs compared with the observed edep curve. The observed curve shows three distinct peaks caused by fragmentation events at heights of 37, 29, and 22 km. The two fragmentation events at 37 and 22 km are not reproduced with our model runs; however the ensemble of simulations generally reproduce the observed maximum edep (within a factor of two) at ~29 km. Similarly, the average peak magnitude of the modelled fireball was -21.4, a good match to the observed peak absolute visual magnitude of -22 (Brown et al., 2004). Our mean modelled initial mass of 1.04×10^4 kg is similar to the estimate from Brown et al. (2004) but a factor of 2 - 3 higher than a more recent estimate by Meier et al. (2017) based on short-lived radionuclide or the estimate from ReVelle (2005).

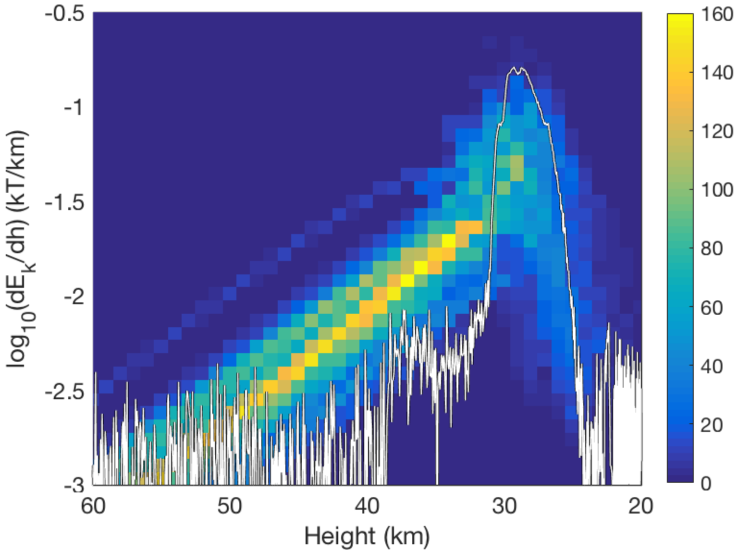

Figure 4.9: The TPFM model fit to the observed edep curve for the Park forest fireball. The 80 runs which met all empirical criteria (as described in the text) are shown as color curves. For the simulated runs, the average mass was $10.4 \pm 4.0 \times 10^3$ kg, the average radius was 0.97±0.2 m, with the average energy was 0.47 kT.

The model result (Fig. 4.10) suggests that the peak maximum ΔP was only 167 Pa, below the limit where reports of window damage even in a dense urban area, might be expected (e.g. Clarkson and Mayes, 1972). This also compares favorably with a peak maximum ΔP of 140 Pa computed from the actual light curve.

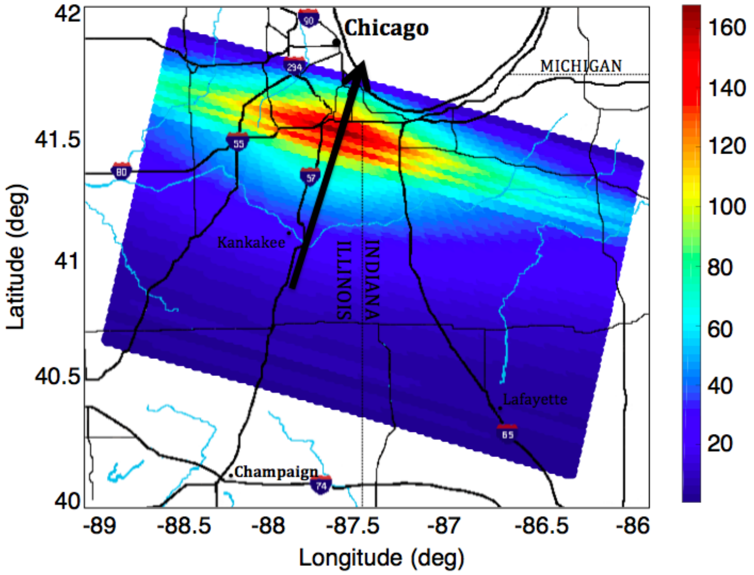

Figure 4.10: The predicted ground-level maximum weak shock ΔP (Pa) for the Park Forest fireball. The arrow represents the bolide trajectory from a height of 80 km to 18 km moving north-northeast. The colormap shows all the ground points that were accessible to the ballistic shock wave in this height interval. With the peak maximum ΔP of ~167 Pa, there is less than a 0.1% probability of breaking typical windows in urban areas.

The September 3, 2004 Antarctica Fireball

The optical light curve for this fireball was measured by Department of Energy space-based visible light sensors and showed two major fragmentation episodes at altitudes of 32 km and 25 km (Klekociuk et al., 2005). The observed light curve, converted to an equivalent edep curve (see Appendix B section B.3 for details) and compared with the TPFM model fit is shown in Fig. 4.11. The majority of our simulated runs produced about 4 times larger peak edep than that derived directly from the observed light curve. This might be interpreted as the meteoroid being stronger or undergoing less fragmentation than a typical meteoroid; it may also be related to its very low entry speed.

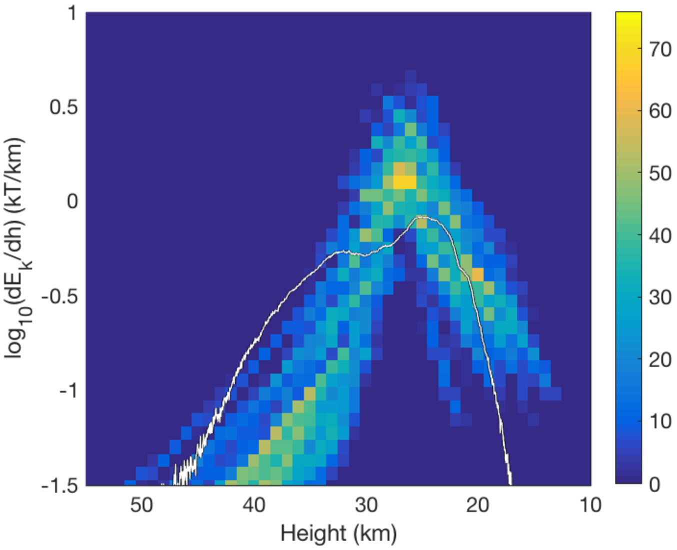

Figure 4.11: The TPFM model fit to the observed edep curve (white line) for the Antarctica fireball. Out of 1000 simulated runs, we found 38 runs that match all our empirical correlations and observational constrains. For the simulated runs, the average mass was $6.04 \pm 2.0 \times 10^5$ kg, the average radius was 3.9 ± 0.6 m, with the average energy of 12.2 kT. Our model result matches well with Klekociuk et al. (2005) who obtained a total initial energy of 13 kT corresponding to a mass of $6.5 \pm 0.5 \times 10^6$ kg by applying entry modelling of the light curve and trajectory data.

The ground footprint associated with the maximum weak shock model is shown in Fig. 4.12 with the $\Delta P(500)$ inside the dashed line. The modeled peak maximum ΔP is 585 Pa, noticeably higher than the ΔP of 340 Pa found using the actual light curve . The model $\Delta P(500)$ corresponding to the area that would have experienced window breakage is about 510 km^2. This fireball shows the greatest deviation between ΔP levels computed from the true light curve and edeps produced from our Monte Carlo modeling approach. It is also the lowest speed of all five of our calibration events. This emphasizes the potential limitations of our approach when applied to unusual or rare fireball populations, such as low speed events, which are not necessarily well represented in the population as a whole from which our empirical constraints are drawn.

We suggest this bias may reflect the fact that the true luminous efficiency is much lower at low speeds (Nemtchinov et al., 1997) than is assumed in the nominal JPL energy estimates when using the actual light curve. This is because the Brown et al. (2002a) formulation for luminous efficiency used to compute JPL energies does not explicitly account for changes in luminous efficiency at low speeds but uses population averages. Hence the ΔP computed from the light curve for such low speeds would actually be too small, as we see for the Antarctica event.

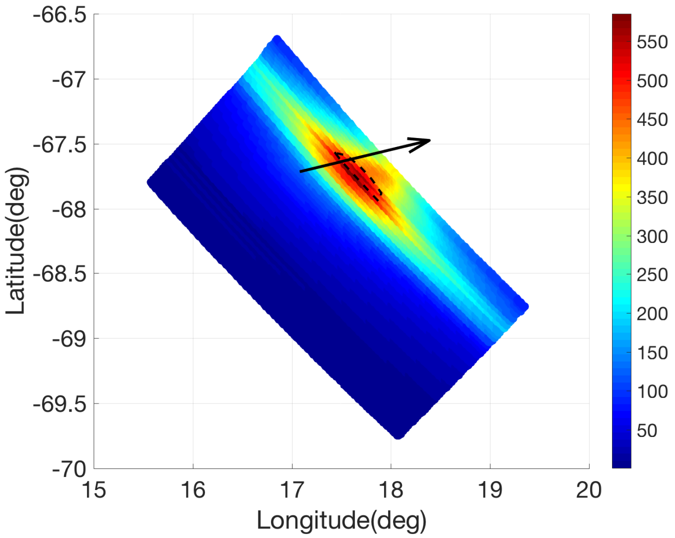

Figure 4.12: The predicted ground-level maximum weak shock ΔP (Pa) for the Antarctica fireball. The arrow represents the bolide trajectory from an altitude of 70 km to 16 km moving towards the east-northeast. The colormap shows all the ground points that were accessible by the cylindrical shock produced during ablation. The dashed line shows the boundary where the model maximum ΔP exceeds 500 Pa.

The July 23, 2008 Tajikistan Fireball

The satellite optical light curve from Konovalova et al. (2013) was digitized and used to produce an equivalent edep curve. The TPFM model runs are compared with the observed edep curve in Fig. 4.13. Our simulated runs only match the second and third flares of the observed edep curve at 26 and 24 km to within a factor of 2 - 3. The maximum edep from model runs and observations were in good agreement at a height of 35 km.

Fig. 4.14 shows the result from the weak shock model indicating a peak maximum ΔP of 65 Pa. The corresponding plot for a median of 35 Pa can be found in Appendix B.4.5 figure

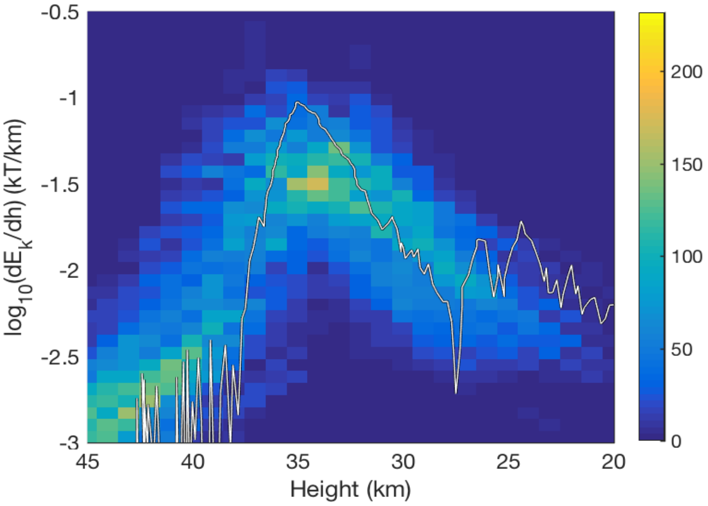

Figure 4.13: The TPFM model edep profiles compared to the observed edep curve for the Tajikistan superbolide. Out of 1000 simulated runs, we found 116 runs that match all of our empirical correlations and observational constrains. For the simulated runs, the average mass was found to be $1.4 \pm 0.4 \times 10^4$ kg, the average radius 1.1 ± 0.2 m while the average energy was 0.34 kT. Our model result shows a reasonable agreement with Konovalova et al. (2013) where they computed an initial mass of 20 – 25 tons based on the theoretical estimates of initial kinetic energy of 0.59 kT.

B.8(e). These peak maximum and median ΔP plots are similar to the 45 Pa computed from the light curve and in all instances clearly well below levels that could produce window damage.

Summary for Five Calibration Fireballs

The ΔP results from all five calibration events are summarized in Table 4.2. We compare the peak ΔP computed based on the observed light curves with median and maximum ΔP computed based on the modelled light curves. In all cases (except for the Antarctica event as discussed earlier) the light curve maximum ΔP lies between the median and maximum model ranges for ΔP.

We also show the computed ground footprint in terms of the area (km^2) above which the expected median and maximum ΔP exceeded the 200 Pa and 500 Pa limits and compare with area footprints computed from the observed light curves. In general, our light curve derived ΔP values and ground area footprints found from TPFM models which are selected on the basis

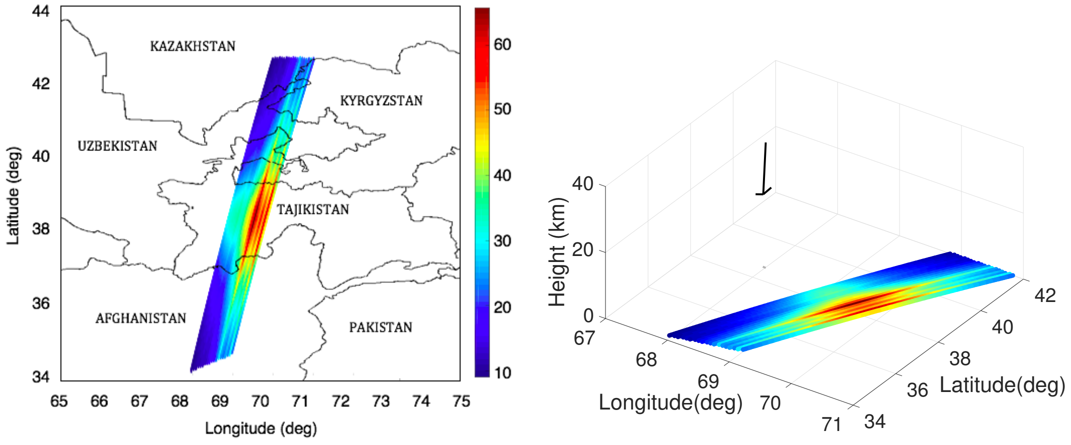

(a) (b)

Figure 4.14: The predicted maximum ground-level weak shock ΔP (Pa) for the Tajikistan superbolide. (a) Top down view. The short black horizontal line at 38.5°N, 68°E indicates the bolide trajectory moving towards west. As the fireball entered the atmosphere at a very steep angle (80° from the horizontal), the ground projected length of the trajectory was very short, only ~5.3 km. (b) 3D view. The arrow represents the bolide trajectory from a height of 38 km to 20 km.

of the empirical criteria fits discussed earlier are within a factor of several as compared to the values which would be found using the actual light curve, though in most cases these are all small areas.

On this basis, we believe that applying our generic Monte Carlo TPFM model approach constrained by empirical criteria to the entire suite of energetic JPL fireballs (all of which do not have available light curves) should yield reasonable limits on expected window breakage on the ground. We apply our formalism in the next section to this suite of bolides, examining both the expected peak maximum ΔP, and ground ΔP-Area footprints.

4.4.2 JPL Fireball Events

Having validated our method by analyzing five fireballs where light curves are known, we next examined a number of energetic bolide events (E > 2 kT) (Appendix B Table B.1) to estimate the characteristics of the resulting weak shock ΔP on the ground. As described earlier, for each event, we used the TPFM model to generate ranges of edep with height, consistent

Event name	Value	Using observed light curves	Median ΔP of simulations	Maximum ΔP of simulations
Marshall Islands	Peak ΔP	590	500	740
	$\Delta P(200)$	7200	5900	10000
	$\Delta P(500)$	260	9	1300
Tagish Lake	Peak ΔP	230	150	240
	$\Delta P(200)$	76	-	1200
	$\Delta P(500)$	-	-	-
Park Forest	Peak ΔP	140	92	167
	$\Delta P(200)$	-	-	-
	$\Delta P(500)$	-	-	-
Antarctica	Peak ΔP	340	380	585
	$\Delta P(200)$	3900	4800	13000
	$\Delta P(500)$	-	-	510
Tajikistan	Peak ΔP	45	35	65
	$\Delta P(200)$	-	-	-
	$\Delta P(500)$	-	-	-

Table 4.2: Comparison of peak ΔP (Pa) and threshold ΔP-areas (km^2) computed based on both the observed light curves and the simulated light curves for five calibration fireballs. Here $\Delta P(200)$ and $\Delta P(500)$ represent the ground-level areas where the ΔP exceeds 200 Pa and 500 Pa, respectively. For the simulation result, peak ΔP and threshold ΔP-areas were computed based on the median ΔP plot (see Appendix B section B.4) and the maximum ΔP plot (section 4.4.1), the latter providing an upper limit to the expected ΔP.

with the speed, height of peak brightness, entry angle and energy reported on the JPL website. A total of 10,000 realizations were run for each event and a sub-set of the runs consistent with our empirical criteria were retained. The resulting edep curves are then combined with the weak shock analytic model to compute ground ΔP. In all, 18 fireballs reported on the JPL web page over the last 25 years had sufficient information and were above our threshold energy (2 kT) to allow modelling with our approach. The predicted maximum ΔP plots for each of the 18 events can be found in Appendix B section B.5.

Fig. 4.15 shows the peak median and maximum ground ΔP as a function of JPL fireball energy, color coded by (a) height (km) at the peak brightness and (b) entry angle (°). The height at the peak brightness makes the largest difference in peak ΔP for events of similar energy, as expected. Fireballs having as little as 5 kilotons of energy, if they penetrate to low enough heights (< 26 km), can produce ΔP on the ground in the half kilopascal range. For low energy events in general, we obtain higher ΔP with shallower entry angles as expected. This is mainly because the minimum range to the ground for ballistic shocks is smaller than for steeper events, if all other quantities being the same.

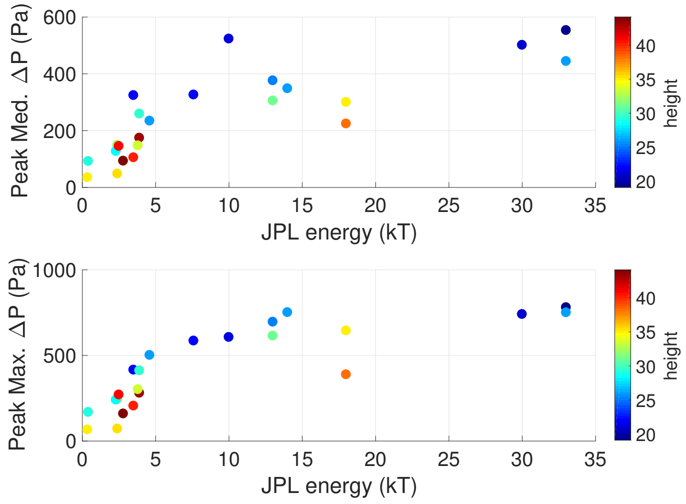

(a)

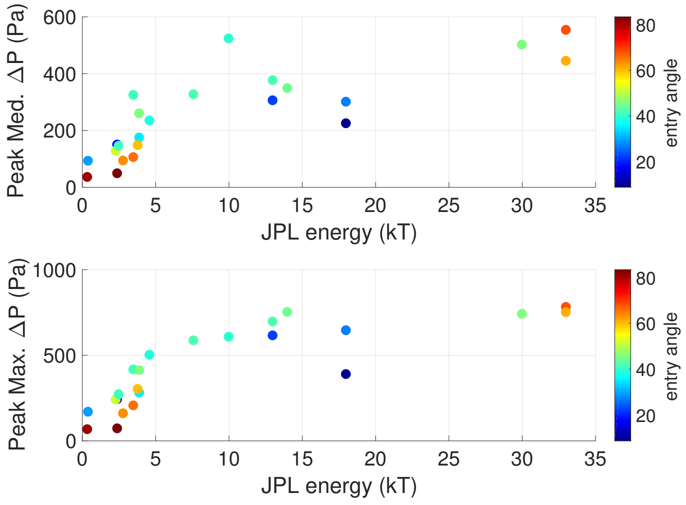

(b)

Figure 4.15: The predicted ground-level peak median and maximum ΔP for 18 of the most energetic JPL bolide events and 3 of our calibration fireballs having E > 2 kT as a function of energy. (a) Color represents the height (km) at peak brightness. (b) Color represents the entry angle with respect to the horizon.

We also calculated the total ground area (km^2) under the fireball trajectory where the maximum ΔP exceeded the 200 Pa and 500 Pa thresholds. Fig. 4.16 shows these ΔP-area footprints color coded by the fireball (a) height (km) at the peak brightness and (b) entry angle (°). It is clear that more energetic events affect larger areas. All bolides having E > 5 kT produced peak maximum ΔP greater than 500 Pa. However, one event (2009-11-21) with very high height at peak brightness (= 38 km) produced peak maximum ΔP of only 390 Pa, even though it had a total energy of 18 kT. Similarly, all events with E < 5 kT produced lower than 500 Pa ΔP, except one event (2003-09-27) that penetrated very deep into the atmosphere (height at the peak brightness = 26 km). This event had a maximum $\Delta P(500)$ of ~10 km^2.

4.5 Discussion

In the following we focus on the maximum ΔP produced by our simulations. This represents the largest computed ΔP at each ground point across all realizations for a particular event and provides an upper limit to the expected ΔP.

Examination of Fig. 4.15 and 4.16 shows that the effective threshold energy at which fireballs in our case study produce ΔP levels where window damage would be heavy and might be reported (should these occur over an urban area) is ~ 5 kT. That is, among the events we examined which occurred in the last quarter century globally, no fireball modeled with a JPL energy < 5 kT had significant maximum ground ΔP in excess of 500 Pa using our simulation scheme. Virtually all fireballs having larger energy than this threshold produced maximum ΔP in excess of 500 Pa.

We note that in practice, our approach to modeling of a 5 kT JPL energy fireball encompasses an energy range up to 10 kT (see Appendix B section B.2.2 for details), as we have adopted a factor of two uncertainty in individual luminous efficient estimates following Nemtchinov et al. (1997). It is these highest energy realizations for a particular event which produce the maximum ΔP on the ground. Hence a more realistic limit on the total fireball energy required to produce window damage is ~ 10 kT. Based on the energy - impact frequency ranges for bolides given in Brown et al. (2002a) and Brown et al. (2013), a 10 kT event impacts

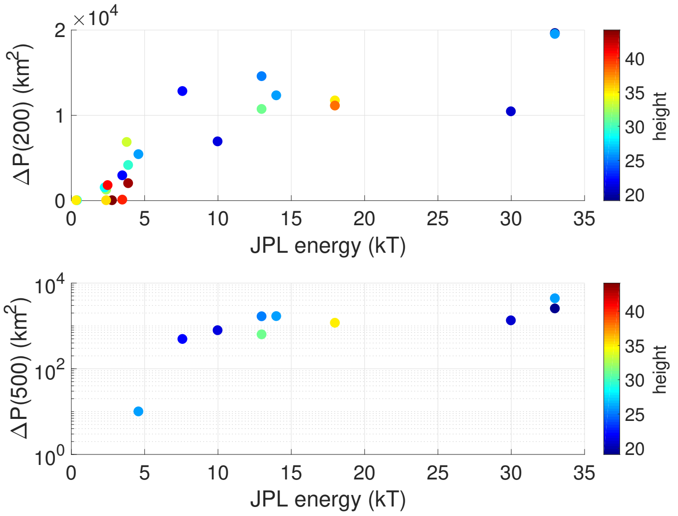

(a)

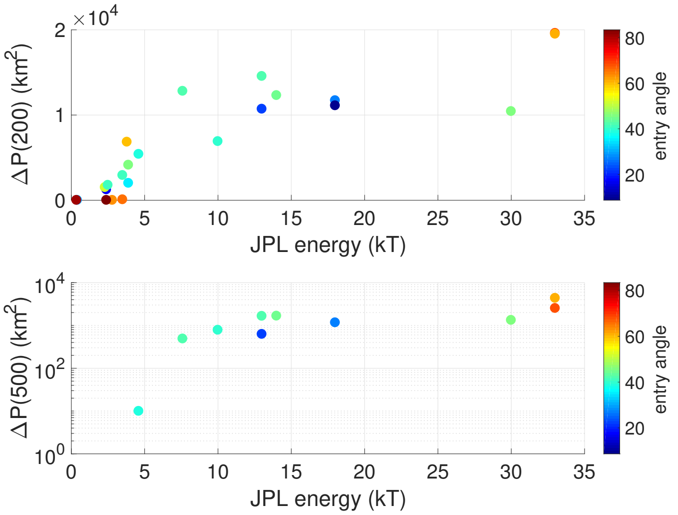

(b)

Figure 4.16: The calculated ground area (km^2) where the maximum ΔP exceeds 200 Pa and 500 Pa for 18 energetic bolide events and 3 calibration events (E > 2 kT) as a function of JPL energy. (a) Color represents the height (km) at the peak brightness. (b) Color represents the entry angle relative to the horizon.

the Earth every 1 - 2 years.

The individual $\Delta P(200)$ and $\Delta P(500)$ for all 18 JPL events and our five calibration events can be found in Appendix B Table B.8. As a reminder, our 200 Pa and 500 Pa were thresholds chosen for breaking a standard sized window (area of 0.5 - 1.5 m^2) with a probability of ~0.01 - 0.7% and 0.4 - 7% while a large window with area > 2m^2 would have a breakage probability of ~1.5% and 12% at 200 Pa and 500 Pa, respectively.

From our examination of these 23 energetic fireballs occurring over the last 25 years we find the total surface area of the Earth that has experienced a maximum ΔP greater than 200 Pa from fireball shock waves was 1.6×10^5 km^2. This translates approximately into an average annual affected area of 6.2×10^3 km^2. Similarly, the total affected ground area where maximum ΔP exceeded 500 Pa was 1.5×10^4 km^2, resulting in an average affected area of 580 km^2 every year (Table 4.3).

Med. ΔP(200)	Med. ΔP(500)	Max. ΔP(200)	Max. ΔP(500)
2.2×10^3	3.6	6.2×10^3	580

Table 4.3: Summary of total ground-level areas (km^2) where the median and maximum ΔP exceed the 200 Pa and 500 Pa thresholds for one year average.

However, our 23 fireballs does not include the February 15, 2013 Chelyabinsk fireball. This is the largest recorded airburst on Earth since the 1908 Tunguska event (Brown et al., 2013; Popova et al., 2013). Unfortunately, we cannot apply our method to model this event at all ground points, as some ground points nearly under the fireball have geometry such that at one blast radius of range the atmospheric pressure changes by a factor of several, violating one of the assumptions in the use of the ReVelle weak shock model. The peak ΔP below the Chelyabinsk fireball, for example, is not determined with our approach, though the weak shock approach is marginally applicable to downtown Chelyabinsk as it has a comparatively large slant range from the peak edep point on the trail.

Thus, we extracted the estimated ΔP(500) from Popova et al. (2013), where they used a numerical entry model to estimate the ΔP contours on the ground, and showed that ΔP(500) would be ~ 1.9×10^4 km^2. This is more total ground area having ΔP(500) than all other fireballs in the last 25 years combined. This brings the average annual ΔP(500) affected area (including Chelyabinsk) to ~10^3 km^2. For the lower ΔP limit of 200 Pa at larger slant ranges (where most of the ground area is located) we can make use of the weak shock model to produce an estimate for Chelyabinsk of ΔP(200), which we find to be ~ 4.5×10^4 km^2. This brings the total annual

$\Delta P(200)$ affected area (including Chelyabinsk) to ~8×10^3 km^2.

For the more significant $\Delta P(500)$, the majority of the risk for window damage is caused by the very largest events, notably Chelyabinsk in our study time frame. This is as one would expect and is similar to the distribution of risk in the overall impact hazard, wherein the largest events cause the majority of the damage over the longest timescale (cf. Boslough et al. 2015).

The fraction of the Earth's total surface area covered by urban area is approximately 1% (Liu et al., 2014). Taking this as the effective area with significant numbers of windows we have roughly 5×10^6 km^2 of earth's surface covered by buildings/windows. We can calculate the expected annual probability that a fireball will occur over an urban area capable of producing ground-level ΔP at our 200 or 500 Pa threshold by the ratio of the urban area to the total surface area of the Earth compared to the maximum $\Delta P(200)$ or $\Delta P(500)$ areas.

Using current values for global urbanization, we expect an urban area to be affected once per ~ 5000 years by a fireball producing $\Delta P(500)$ where a single standard sized window would break at the 0.4 - 7% probability level. Similarly, roughly every 600 years we expect a fireball over an urban area producing a $\Delta P(200)$ with a probability of individual window breakage 0.01 - 0.7%. How many windows are actually broken for a given event depends on the details of the geometry of the fireball path relative to the urban area and peak ΔP, but these values provide a guide to the expected time between window-breaking events. Window breakage from fireballs should be a very rare occurrence. Viewed in this context, Chelyabinsk is an even more extraordinary event.

4.6 Conclusions

In this chapter, we estimate how often fireballs produce window damage based on a case study of roughly two dozen energetic fireballs recorded in the last quarter century. This dataset consisted of 18 bolides ($E > 2$ kT) with limited flight data and 5 fireballs with light curves which we used to validate our entry model approach. Our Monte Carlo entry modeling was used to estimate energy deposition curves which produced ΔP for the five validation events differing by no more than a few tens of percent from values computed using the actual light curves. In four of the five cases examined, the peak ΔP computed from the observed light curve fell between our model median and maximum peak ΔP computed using our generic Monte Carlo modeling approach. For one calibration case (the Sep 3, 2004 Antarctica fireball) we suggest the larger difference in observed vs. model ΔP results from the very low speed of the event and the correspondingly lower luminous efficiency (and hence higher total energy) for this event compared to the nominal JPL computed energy.

Based on the overall relationship between ground ΔP and bolide energy from all 23 of our simulated fireballs, we found that energy plays the largest role in determining the ground-level ΔP with the height at the peak brightness and entry angle also affecting values. Given the same energy, bolides with lower height at the peak brightness produced higher ΔP, affecting larger areas on the ground. Similarly, higher ΔP was typically obtained with shallower entry angle.

We find that fireballs with E ~ 5 - 10 kT were needed to produce maximum ΔP greater than 500 Pa, which we would associate with heavy window damage on the ground in a dense urban area. At this ΔP level, window breakage occurs with a probability of 0.01 - 0.7% for standard sized windows (area of 0.5 - 1.5 m^2) and a probability of 0.4 - 7% for large windows (area > 2 m^2). This suggests that the effective threshold energy for fireballs to produce window damage is ~5 - 10 kT, such events happening every 1 - 2 years globally.

Calculation of the equivalent average annual $\Delta P(500)$ and $\Delta P(200)$ based on all major fireball events (including Chelyabinsk) detected in the last 25 years produced annualized affected areas of 10^3 and 8×10^3 km^2 respectively. This leads to an average recurrence interval for fireballs producing $\Delta P(500)$ over an urban area approximately once every 5000 years while the expected frequency of urban area exposure to fireballs producing $\Delta P(200)$ is every ~600 years.

During our case study interval (1992 - 2017) a total of 18 fireballs were recorded with E > 2 kT which had velocity, height and location information. The majority contribution to the total global areal ΔP footprint caused by their associated shocks producing $\Delta P(500)$ was from the Chelyabinsk fireball. The largest events dominated the long term damage at high ΔPs. In contrast, Chelyabinsk was responsible for only about 1/4 of the cumulative areal ground exposure at the lower $\Delta P(200)$. Smaller more frequent events (and particularly more deeply penetrating fireballs) are significant contributors at these lower ΔPs, near the threshold where sonic boom ΔPs historically begin producing window damage reports in urban areas.

In summary, we expect window breakage from fireballs to be a very rare occurrence with likely intervals between urban areas exposed to significant fireball ΔP, just capable of damaging windows, to be on the order of century timescales. The widespread window damage from Chelyabinsk is expected over an urban area on multi-millennium timescales (approaching once per 10,000 year event), further underscoring its uniqueness in the modern era.

Though these long average recurrence intervals are comforting, we also emphasize that our analysis suggests that the largest annually occurring bolides are capable of producing heavy window damage. Multi-kiloton bolide events (in the 5 - 10 kT range), should they occur over a major urban centre with large numbers of windows, can easily produce economically significant window damage.

Acknowledgements

The authors thank Natural Resources Canada, the Canada Research Chair program and the Natural Sciences and Engineering Research Council of Canada for funding support. This work was also supported through NASA co-operative agreement NNX15AC94A .

Bibliography

Aftosmis, M. J., Nemec, M., Mathias, D., and Berger, M. (2016). Numerical Simulation of Bolide Entry with Ground Footprint Prediction. In *54th AIAA Aerospace Sciences Meeting*, pages 1–18. American Institute of Aeronautics and Astronautics.

ANSI (1983). Estimating airblast characteristics for single point explosions in air, with a guide to evaluation of atmospheric propagation and effects. Technical report, American National Standards Institute.

Avramenko, M. I., Glazyrin, I. V., Ionov, G. V., and Karpeev, A. V. (2014). Simulation of the airwave caused by the chelyabinsk superbolide. *Journal of Geophysical Research: Atmospheres*, 119(12):7035–7050.

Boslough, M., Brown, P., and Harris, A. W. (2015). Updated population and risk assessment for airbursts from near-earth objects (NEOS). In : 2015 IEEE Aerospace Conference, Big Sky, Montana, pages 1–12.

Boslough, M. B. E. and Crawford, D. A. (1997). Shoemaker-Levy 9 and Plume-Forming Collisions on Earth. *Annals of the New York Academy of Sciences*, 822:236–282.

Boslough, M. B. E. and Crawford, D. A. (2008). Low-altitude airbursts and the impact threat. *International Journal of Impact Engineering*, 35:1441–1448.

Brown, P. (2016). Global detection and flux of superbolides. Meteoroids2016 conference, ESTEC, Noordwijk, Netherlands.

Brown, P., Pack, D., Edwards, W. N., ReVelle, D. O., Yoo, B. B., Spalding, R. E., and Tagliaferri, E. (2004). The orbit, atmospheric dynamics, and initial mass of the Park Forest meteorite. *Meteoritics and Planetary Science*, 39:1781–1796.

Brown, P., Spalding, R. E., ReVelle, D. O., Tagliaferri, E., and Worden, S. P. (2002a). The flux of small near-Earth objects colliding with the Earth. *Nature*, 420:294–296.

Brown, P., Wiegert, P., Clark, D., and Tagliaferri, E. (2016). Orbital and physical characteristics of meter-scale impactors from airburst observations. *Icarus*, 266:96–111.

Brown, P. G., Assink, J. D., Astiz, L., Blaauw, R., Boslough, M. B., Borovička, J., Brachet, N., Brown, D., Campbell-Brown, M., Ceranna, L., Cooke, W., de Groot-Hedlin, C., Drob, D. P., Edwards, W., Evers, L. G., Garces, M., Gill, J., Hedlin, M., Kingery, A., Laske, G., Le Pichon, A., Mialle, P., Moser, D. E., Saffer, A., Silber, E., Smets, P., Spalding, R. E., Spurný, P., Tagliaferri, E., Uren, D., Weryk, R. J., Whitaker, R., and Krzeminski, Z. (2013). A 500-kiloton airburst over Chelyabinsk and an enhanced hazard from small impactors. *Nature*, 503:238–241.

Brown, P. G., Hildebrand, A., Zolensky, M. E., Grady, M., Clayton, R. N., Mayeda, T. K., Tagliaferri, E., Spalding, R. E., Macrae, N. D., Hoffman, E. L., Mittlefehldt, D. W., Wacker, J., Bird, J. A., Campbell-Brown, M. D., Carpenter, R., Gingerich, H., Glatiotis, M., Greiner, E., Mazur, M. J., McCausland, P., Plotkin, H., and Mazur, T. R. (2000). The Fall , Recovery , Orbit , and Composition of the Tagish Lake Meteorite : A New Type of Carbonaceous Chondrite. *Science*, 290:320–325.

Brown, P. G., Revelle, D. O., Tagliaferri, E., and Hildebrand, A. R. (2002b). An entry model for the Tagish Lake fireball using seismic, satellite and infrasound records. *Meteoritics and Planetary Science*, 37:661–675.

Chapman, C. R. and Morrison, D. (1994). Impacts on the Earth by asteroids and comets: assessing the hazard. *Nature*, 367:33–40.

Chyba, C. F., Thomas, P. J., and Zahnle, K. J. (1993). The 1908 Tunguska explosion - Atmospheric disruption of a stony asteroid. *Nature*, 361:40–44.

Clancey, V. J. (1972). Diagnostic features of explosion damage. Sixth International Meeting of Forensic Sciences, Edinburgh.

Clarkson, B. L. and Mayes, W. H. (1972). Sonic Boom Induced Building Structure Responses Including Damage. *The Journal of the Acoustical Society of America*, 51(2C):742–757.

Collins, G. S., Lynch, E., McAdam, R., and Davison, T. M. (2017). A numerical assessment of simple airblast models of impact airbursts. *Meteoritics & Planetary Science*, 19:1–19.

Collins, G. S., Melosh, H. J., and Marcus, R. A. (2005). Earth Impact Effects Program: A Web-based computer program for calculating the regional environmental consequences of a meteoroid impact on Earth. *Meteoritics and Planetary Science*, 40:817–840.

Edwards, W. N. (2010). Meteor generated infrasound : Theory and observation. In *Infrasound Monitoring for Atmospheric Studies*, chapter 12, pages 361–414. Springer Science. Business Media B.V.

Few, A. A. (1969). Power spectrum of thunder. *Journal of Geophysical Research*, 74:6926–6934.

Fletcher, E. R., Richmond, D. R., and Yelverton, J. T. (1980). Glass fragment hazard from windows broken by airblast. Technical report, DNA 5593T.

Gilbert, S. M., Lees, F. P., and Scilly, N. S. (1994). *A model for the effects of a condensed phase explosion in a built-up area*. PhD thesis, Loughborough University.

Glasstone, S. and Dolan, P. (1977). *The effects of nuclear weapons*. U.S. Department of Defense, Washington, D.C. 3rd edition.

Harris, A. W. and D'Abramo, G. (2015). The population of near-Earth asteroids. *Icarus*, 257:302–312.

Hershey, R. L. and Higgins, T. H. (1976). Statistical Model of Sonic Boom Structural Damage. Final Report FAA-RD-76-87.

Hildebrand, A. R., McCausland, P. J. A., Brown, P. G., Longstaffe, F. J., Russell, S. D. J., Tagliaferri, E., Wacker, J. F., and Mazur, M. J. (2006). The fall and recovery of the Tagish Lake meteorite. *Meteoritics and Planetary Science*, 41:407–431.

Hills, J. G. and Goda, M. P. (1993). The fragmentation of small asteroids in the atmosphere. *Astronomical Journal*, 105:1114–1144.

Hills, J. G. and Goda, M. P. (1998). Damage from the impacts of small asteroids. *Planetary and Space Science*, 46:219–229.

Iverson, J. H. (1968). Summary of Existing Structures Evaluation,Pt II: Window Glass and Applications. Contract No. OCD-DAH20_67_C-0136. Final Repport. Stanford Research Institute, Menlo Park, CA.

Jones, D. L., Goyer, G. G., and Plooster, M. N. (1968). Shock wave from a lightning discharge. *Journal of Geophysical Research*, 73:3121–3127.

Kinney, G. and Graham, K. (1985). *Explosive shocks in air*. Springier, New York, 2nd edition.

Klekociuk, A. R., Brown, P. G., Pack, D. W., ReVelle, D. O., Edwards, W. N., Spalding, R. E., Tagliaferri, E., Yoo, B. B., and Zagari, J. (2005). Meteoritic dust from the atmospheric disintegration of a large meteoroid. *Nature*, 436:1132–1135.

Konovalova, N. A., Madiedo, J. M., and Trigo-Rodríguez, J. M. (2013). The Tajikistan superbolide of July 23, 2008. I. Trajectory, orbit, and preliminary fall data. *Meteoritics and Planetary Science*, 48:2469–2479.

Liu, Z., He, C., Zhou, Y., and Wu, J. (2014). How much of the world's land has been urbanized, really? A hierarchical framework for avoiding confusion. *Landscape Ecology*, 29(5):763–771.

Mathias, D. L., Wheeler, L. F., and Dotson, J. L. (2017). A probabilistic asteroid impact risk model: assessment of sub-300 m impacts. *Icarus*, 289:106–119.

Meier, M. M. M., Welten, K. C., Riebe, M. E. I., Caffee, M. W., Gritsevich, M., Maden, C., and Busemann, H. (2017). Park Forest (L5) and the asteroidal source of shocked L chondrites. *Meteoritics & Planetary Science*, 16(8):1388–1425.

Needham, C. E. (2010). *Blast Waves*. Springer Berlin Heidelberg, Berlin, Heidelberg, 1st edition.

Nemtchinov, I. V., Svetsov, V. V., Kosarev, I. B., Golub', A. P., Popova, O. P., Shuvalov, V. V., Spalding, R. E., Jacobs, C., and Tagliaferri, E. (1997). Assessment of Kinetic Energy of Meteoroids Detected by Satellite-Based Light Sensors. *Icarus*, 130:259–274.

Picone, J. M., Hedin, A. E., Drob, D. P., and Aikin, A. C. (2002). NRLMSISE-00 empirical model of the atmosphere: Statistical comparisons and scientific issues. *Journal of Geophysical Research: Space Physics*, 107(A12):15–16.

Popova, O., Borovička, J., Hartmann, W. K., Spurný, P., Gnos, E., Nemtchinov, I., and Trigo-Rodriguez, J. (2011). Very low strengths of interplanetary meteoroids and small asteroids. *Meteoritics & Planetary Science*, 46(10):1525–1550.

Popova, O. P., Jenniskens, P., Emel'yanenko, V., Kartashova, A., Biryukov, E., Khaibrakhmanov, S., Shuvalov, V., Rybnov, Y., Dudorov, A., Grokhovsky, V. I., Badyukov, D. D., Yin, Q.-Z., Gural, P. S., Albers, J., Granvik, M., Evers, L. G., Kuiper, J., Kharlamov, V., Solovyov, A., Rusakov, Y. S., Korotkiy, S., Serdyuk, I., Korochantsev, A. V., Larionov, M. Y., Glazachev, D., Mayer, A. E., Gisler, G., Gladkovsky, S. V., Wimpenny, J., Sanborn, M. E., Yamakawa, A., Verosub, K. L., Rowland, D. J., Roeske, S., Botto, N. W., Friedrich, J. M., Zolensky, M. E., Le, L., Ross, D., Ziegler, K., Nakamura, T., Ahn, I., Lee, J. I., Zhou, Q., Li, X.-H., Li, Q.-L., Liu, Y., Tang, G.-Q., Hiroi, T., Sears, D., Weinstein, I. A., Vokhmintsev, A. S., Ishchenko, A. V., Schmitt-Kopplin, P., Hertkorn, N., Nagao, K., Haba, M. K., Komatsu, M., Mikouchi, T., and the Chelyabinsk Airburst Consortium (2013).

Chelyabinsk Airburst, Damage Assessment, Meteorite Recovery, and Characterization. *Science*, 342:1069–1073.

Popova, O. P. and Nemtchinov, I. V. (2000). Estimates of Some Recent Satellite Registered Bolides. *Meteoritics and Planetary Science Supplement*, 35:A129.

Pritchard, D. K. (1981). Breakage of glass windows by explosions. *Journal of Occupational Accidents*, 3(2):69–85.

Reed, J. W. (1992). Airblast damage to windows. Technical report, Explosives Safety Board, Department of Defense Washington, DC, Minutes of Twenty-fifth Explosives Safety Seminar.

Register, P. J., Mathias, D. L., and Wheeler, L. F. (2017). Asteroid fragmentation approaches for modeling atmospheric energy deposition. *Icarus*, 284:157–166.

ReVelle, D. O. (1974). *Acoustics of meteors-effects of the atmospheric temperature and wind structure on the sounds produced by meteors*. PhD thesis, Michigan University, Ann Arbor.

ReVelle, D. O. (1976). On meteor-generated infrasound. *Journal of Geophysical Research*, 81:1217–1230.

ReVelle, D. O. (1979). A quasi-simple ablation model for large meteorite entry - Theory vs observations. *Journal of Atmospheric and Terrestrial Physics*, 41:453–473.

ReVelle, D. O. (2005). Recent Advances in Bolide Entry Modeling:A Bolide Potpourri. *Earth Moon and Planets*, 97:1–35.

ReVelle, D. O. (2007). NEO fireball diversity: energetics-based entry modeling and analysis techniques. In *Near Earth Objects, our Celestial Neighbors: Opportunity and Risk*, volume 236 of *IAU Symposium*, pages 95–106.

Robertson, D. K. and Mathias, D. L. (2017). Effect of yield curves and porous crush on hydrocode simulations of asteroid airburst. *Journal of Geophysical Research: Planets*, 122:599–613.

Rumpf, C. M., Lewis, H. G., and Atkinson, P. M. (2017). Asteroid Impact Effects And Their Immediate Hazards For Human Populations. *ArXiv e-prints*.

Sakurai, A. (1964). Blast wave theory. Technical report, Mathematics Research Center, United States Army University of Wisconsin.

Seaman, L. (1967). Response of windows to sonic booms. Technical report, SRI ETU-5897.

Shuvalov, V. V., Svettsov, V. V., and Trubetskaya, I. A. (2013). An estimate for the size of the area of damage on the Earth's surface after impacts of 10-300-m asteroids. *Solar System Research*, 47:260–267.

Shuvalov, V. V. and Trubetskaya, I. A. (2007). Aerial bursts in the terrestrial atmosphere. *Solar System Research*, 41:220–230.

Silber, E. A., Brown, P. G., and Krzeminski, Z. (2015). Optical observations of meteors generating infrasound: Weak shock theory and validation. *Journal of Geophysical Research: Planets*, 120:413–428.

Simon, S., Grossman, L., Clayton, R. N., Mayeda, T., Schwade, J., Sipiera, P., Wacker, J., and Wadhwa, M. (2004). The fall, recovery, and classification of the Park Forest meteorite. *Meteoritics & Planetary Science*, 39(4):625–634.

Tagliaferri, E., Spalding, R., Jacobs, C., and Ceplecha, Z. (1995). Analysis of the Marshall Islands Fireball of February 1, 1994. *Earth Moon and Planets*, 68:563–572.

Toon, O. B., Zahnle, K., Morrison, D., Turco, R., and Covey, C. (1997). Environmental Perturbations Caused by the Impacts of Asteroids and Comets. *Annals of the New York Academy of Sciences*, 822:401.

Tsikulin, M. A. (1970). Shock waves during the movement of large meteorites in the atmosphere (No.NIC-Trans-3148). Technical report, Naval Intelligence Command Alexandria VA Translation Div.

Zhang, X. and Hao, H. (2016). The response of glass window systems to blast loadings: An overview. *International Journal of Protective Structures*, 7(1):123–154.

Chapter 5

Summary, Conclusions, and Future Work

5.1 Summary and Conclusions

The major goals of this thesis were to examine infrasonic airwave signals produced by metre-sized meteoroids to refine their energy estimates and to investigate their airblast effects on the Earth by estimating the frequency of window damage caused by fireball shock waves at the ground.

In Chapter 3, 78 individual bolide events detected at 179 infrasound stations were examined to explore empirical correlations between measured infrasound parameters (particularly signal period) and bolide secondary characteristics (peak brightness height, entry angle, and velocity) reported on the NASA JPL fireball website.

It was found that two effects play a large role in causing the dispersion in signal periods: station noise levels and attenuation effects with range. High signal-to-noise ratio (SNR) points were more clustered along both the AFTAC period-yield relation and our regression to the bolide signal period directly weighed by signal-to-noise ratio. This trend was more clear as we increased the SNR cut-off value. The calculated sum of squared residuals (SSR) decreased as the SNR cut-off value increased.

A greater range from the bolide location to individual infrasound stations resulted in higher signal period, particularly for larger events (> 1 kT). I found no strong empirical correlation between individual station signal period and bolide secondary characteristics, suggesting that the location along the bolide trajectory where peak brightness occurs is not where the infrasonic periods dominantly emanate. I investigated three test cases in detail to determine the source height and to see if varying source height is causing the scatter in signal period. I applied the raytracing method and the ReVelle (1974) weak shock model to obtain self-consistent estimates of source height from each method. It was found that for short-range stations (< 1000 km), heights from raytracing and the weak shock model were generally in good agreement. However, for longer-range stations (> 1000 km), we were not able to isolate a unique source height from raytracing. Our investigation of three test cases indicated that source height may contribute to station period spreads, but our small number of cases precludes any strong statement about the magnitude of such an effect. The main goal of our case studies (to understand where infrasound emanates from along a bolide trajectory for a particular station) was inconclusive.

In Chapter 4, we estimated how often fireballs produce window damage on the ground based on a case study of 23 energetic fireballs recorded in the last 25 years. Based on the empirical relationship between ground overpressure (ΔP) and bolide energy, we found that energy plays the largest role in determining the ground-level ΔP, with the height at the peak brightness and entry angle also having an effect on ΔP values. It was found that a bolide with 5 kT energy can produce ground ΔP in the range of half kilopascal, if it penetrated to low enough heights (< 26 km). Higher ΔP was obtained with shallower entry angles particularly for low energy events. The effective threshold energy for fireballs to produce heavy window damage (ΔP above 500 Pa) was ~5 - 10 kT; such fireballs occur once every one to two years globally. The annual average affected ground area (km^2) where the maximum ΔP exceeded the 200 Pa and 500 Pa thresholds due to the bolide's shock waves was found to be 8×10^3 km^2 and 10^3 km^2 respectively. The corresponding estimated mean frequency of heavy window damage (ΔP above 500 Pa) occurring over urban areas was approximately once every 5000 years and light window damage (ΔP above 200 Pa) was every ~600 years.

5.2 Future Work

A future extension of this meteor generated infrasound study would be to investigate a large set of bolide events having known trajectories and energy deposition curves to validate the method for isolating the source height. An improved raytracing model for signal prediction should be considered.

Improvement of the bolide ablation entry model discussed in Chapter 4 including continuous fragmentation of the meteoroid during flight would also be useful. This improvement will help to provide more accurate estimates of the regional and global consequences of meteoroid impacts on Earth, particularly at our near threshold energies where ground damage might occur.

Additional future work includes updating the data set of infrasonic measurements of the JPL fireball events and quantitatively determining the IMS detectability for bolides. Another goal for such work would be to estimate the effectiveness of IMS detectability by examining the station signal noise and propagation characteristics for each bolide event at each station.

Finally, further expansion of the bolide database from the International Data Centre (IDC) Reviewed Event Bulletin (REB) is another area of future work. The REB provides all the sources of infrasound events recorded at the IMS infrasound network. Among all the events recorded, identifying the bolides events and analyzing their infrasound signal will provide a modern, independent estimate of the bolide flux expanding the earlier work of Silber et al. (2009).

Bibliography

ReVelle, D. O. (1974). *Acoustics of meteors-effects of the atmospheric temperature and wind structure on the sounds produced by meteors*. PhD thesis, Michigan University, Ann Arbor.

Silber, E. A., ReVelle, D. O., Brown, P. G., and Edwards, W. N. (2009). An estimate of the terrestrial influx of large meteoroids from infrasonic measurements. *Journal of Geophysical Research: Planets*, 114:E08006.

Appendix A

Supplementary Material for Chapter 3

A.1 Detailed Inframeasure Methodology

This section briefly describes the 7-step process (Edwards et al., 2006) with modified procedure improving the signal measurements quality (Ens et al., 2012) that was used to extract bolide infrasound signal characteristics.

1. From InfraTool, signal arrival time is determined by the start of a constant back azimuth and trace velocity.

2. Average signal back azimuth and trace velocity are calculated and taken to define a single back azimuth and velocity for the entire incoming wave.

3. Using average back azimuth and trace velocity, delay times are calculated for each waveform recorded at array element. These delay times are used to shift and phase align each waveform (Fig. A.1). After phase alignment, all waveforms are stacked to produce an "optimum waveform".

4. The stacked, raw waveform is bandpass filtered using a second-order Butterworth filter. To determine the most optimal frequency bandpass, a power spectral density (PSD) plot (Fig. A.2) is used. The lower cut-off and high cut-off frequencies are obtained where

the signal PSD drops down to the level of noise PSD for the first time and last time, respectively. Once filtered, the waveform's amplitude envelope is computed using Hilbert Transform (Fig. A.3).

5. The maximum amplitude is determined by taking the peak of the amplitude envelope (red circle on Fig. A.3). The maximum peak-to-peak (P2P) amplitude is obtained by selecting peak to peak points on the optimum waveform (pink squares on Fig. A.3).

6. The signal period at maximum amplitude is obtained using zero-crossing method. The signal period is measured by selecting the four zero-crossing periods near the peak amplitude and taking the average of signal duration A and B (Fig. A.3). This method is most analogous to the method used on chart records in the AFTAC data. Another approach used to determine the signal period is finding the inverse of the frequency at the maximum signal power spectral density (PSD) (Fig. A.2). The frequency at the maximum PSD is placed in between the lower cut-off and high cut-off frequencies.

7. Total integrated energy is determined by squaring and summing each sample of the optimum waveform. A similar procedure is performed for the stacked and filtered waveforms and these values are averaged to find the ambient background noise energy. Note that the ambient background noise level is assumed to be constant throughout the signal duration. Background noise energy is subtracted to obtain the amount of energy due to bolide airwave.

8. Integrated energy signal-to-noise ratio (SNR) is computed using the total integrated signal energy divided by the average background noise energy found in step 7.

9. At the end of each measurement, the following bolide infrasound signal characteristics are obtained:

   - Maximum amplitude (Pa)
   - Maximum P2P amplitude (Pa)
   - Period at maximum amplitude (s)

- Frequency at maximum PSD (Hz)
- Noise PSD (Pa^2/Hz)
- Integrated signal energy of total signal (Pa^2)
- Background noise integrated energy (Pa^2)
- Total signal energy of bolide (Pa^2)
- Integrated signal energy of total signal (Pa^2)
- Bolide P2P amplitude SNR
- Bolide integrated energy SNR
- Lower bandpass frequency(Hz)
- Higher bandpass frequency(Hz)
- Signal back azimuth (°)
- Signal trace velocity (km/s)
- Signal arrival time (HH:MM:SS)
- Signal duration (s)

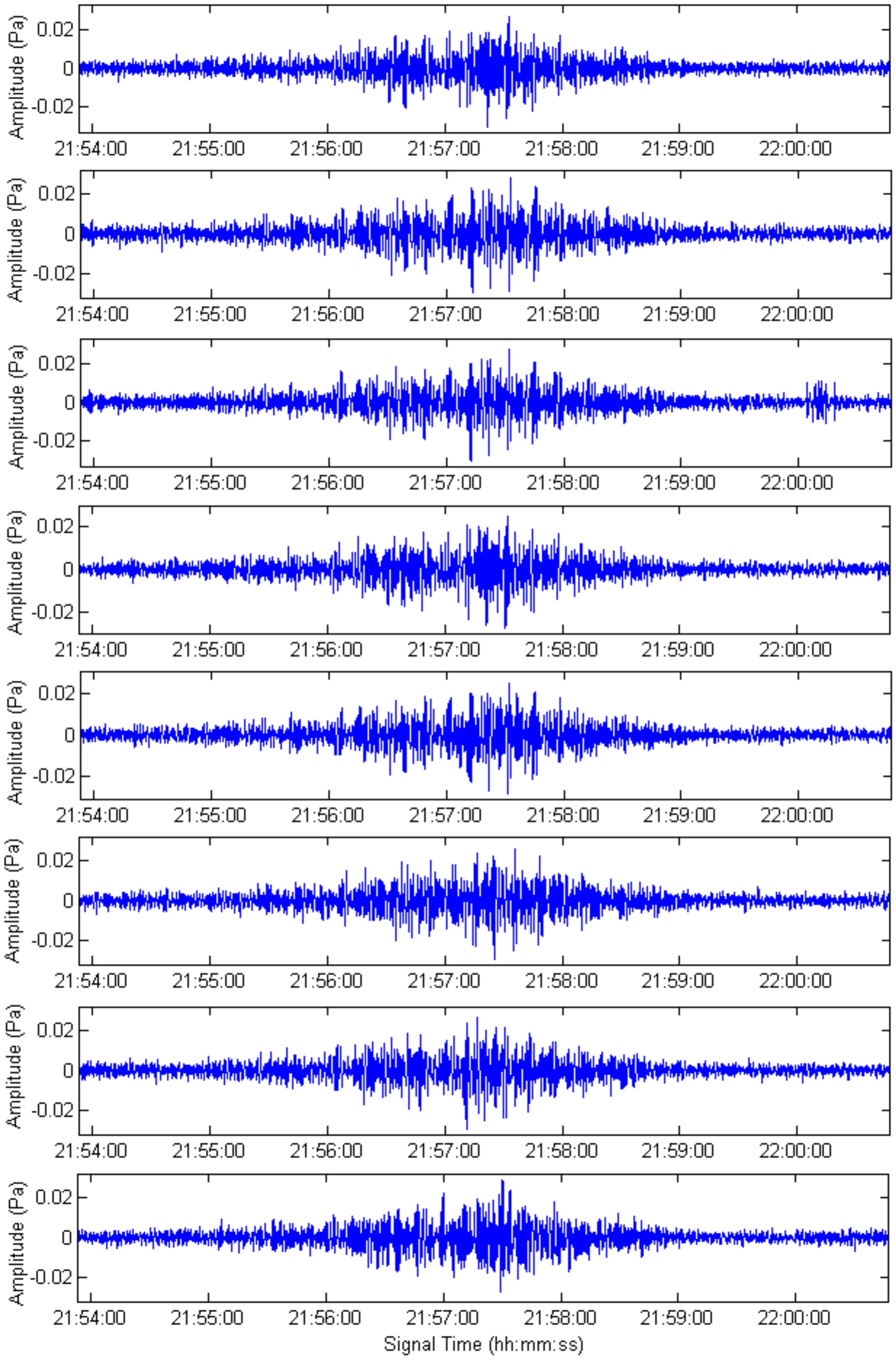

Figure A.1: Second order Butterworth filtered (0.3 - 4 Hz) waveforms recorded at each array element at IS31 for the Turkey fireball (September 2, 2015).

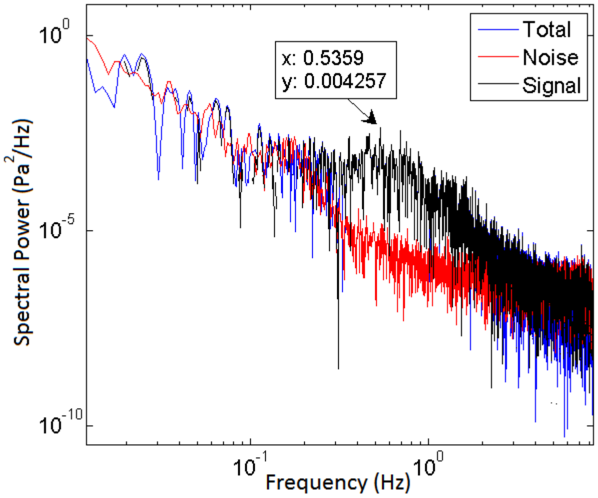

Figure A.2: Power spectral density (PSD) plot for the entire IS31 array for the Turkey fireball (September 2, 2015). The blue curve is the PSD measurement of the total signal and the red curve is the PSD of the noise. The black curve shows the PSD of the bolide signal alone, which was calculated after noise subtraction. The arrow points to the dominant frequency of the signal (x = 0.5359 Hz) which is defined to be the frequency at the maximum PSD of the signal.

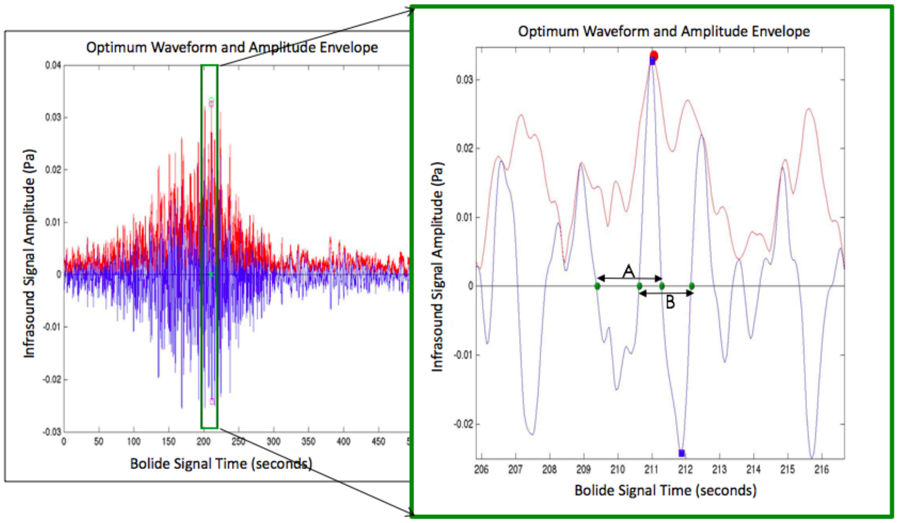

Figure A.3: Inframeasure analysis of the infrasound signal for the Turkey fireball (September 2, 2015) detected at IS31. Blue waveform is the optimum waveform generated after phase alignment of all signal waveforms detected at each array element. Red shows the amplitude envelope computed using Hilbert Transform. The zoomed in portion shows the peak of the envelope which represents the maximum amplitude. The average of signal duration A and B represents the signal period.

A.2 Infrasound Signal Dataset

Table A.1: Summary of infrasound signal characteristics from 78 individual bolide events detected at 179 infrasound stations between 2006 to 2015 following the bolide infrasound analysis of Edwards et al., (2006) and Ens et al., (2012). The table shows for each detection; bolide date/time from the JPL webpage, infrasound station, signal arrival time, signal duration, range from the bolide location to station, theoretical back azimuth (Az), observed back azimuth (Az), JPL energy measured by U.S. government sensors, peak-to-peak (P2P) amplitude, period at maximum amplitude computed using the zero crossings method (Edwards et al., 2006), period from inversion of frequency at the maximum power spectral density (PSD), bolide integrated energy signal to noise ratio (SNR) and bandpass used for measurements. The highlighted events are common with Ens et al. (2012).

Date/ [Time]	**Station**	**Arrival time (UT)**	**Duration (s)**	**Range (km)**	**Theo. Az (deg)**	**Obs. Az (deg)**	**JPL Energy (kT)**	**P2P Amp (Pa)**	**Period @Max Amp (s)**	**Period @Max PSD (s)**	**Bolide Integ. Energy SNR**	**Bandpass (Hz)**
19-Feb-16 [08:15:02]	I17CI	09:10:08	356	1000	229	230	0.56	0.15	3.58	4.40	3.33	0.08-2.5
	I50GB	09:08:03	439	1009	18	14	0.56	0.39	2.19	3.26	2.37	0.5-4
06-Feb-16 [13:55:09]	I49GB	15:23:34	120	1425	298	296	13	0.11	5.87	7.31	1.11	0.25-1.5
	I27DE	18:06:14	360	4601	337	334	13	1.50	6.61	6.94	33.08	0.02-3.5
	I11CV	18:51:18	142	5083	183	158	13	0.06	2.42	2.35	1.44	0.4-1.2
21-Dec-15 [02:32:48]	I39PW	03:28:07	519	951	101	100	0.26	0.28	3.18	3.71	1.75	0.2-4
13-Oct-15 [12:23:08]	I08BO	14:16:08	160	1959	64	41	0.082	0.03	1.60	1.45	0.65	0.4-2
08-Sep-15 [13:46:42]	I32KE	14:49:15	259	1138	318	315	0.073	0.06	1.64	1.51	7.32	0.5-2.5
07-Sep-15 [01:41:19]	I45RU	06:08:06	174	4545	234	236	3.9	0.01	1.99	1.69	1.12	0.5-1.5
	I46RU	05:54:31	505	4555	159	160	3.9	0.04	3.34	3.44	2.65	0.2-1.2
	I04AU	07:03:19	672	5762	338	336	3.9	0.05	1.15	1.07	2.87	0.8-2
	I53US	10:42:44	534	9596	297	300	3.9	0.02	2.97	2.80	2.80	0.2-1.5
2-Sep-15 [20:10:30]	I31KZ	21:53:55	463	1879	233	232	0.13	0.06	1.71	1.87	15.25	0.3-4
	I48TN	22:45:14	336	2736	73	72	0.13	0.01	1.72	1.86	2.17	0.5-1.5
	I46RU	23:36:04	323	3712	262	257	0.13	0.02	2.67	2.59	3.57	0.25-1.5
	I32KE	11:34:16	480	963	292	291	0.41	0.08	1.16	1.18	5.01	0.5-4

09-Jan-15

[10:41:11]	I19DJ	12:36:20	132	1903	237	237	0.41	0.08	2.01	1.99	1.75	0.45-1.2
07-Jan-15	I26DE	02:09:25	412	1053	104	105	0.4	0.32	2.85	2.79	14.31	0.3-6
[01:05:59]	I43RU	02:22:15	888	1417	215	214	0.4	0.18	3.24	2.95	2.49	0.3-4
13-Dec-14	I18DK	04:15:28	201	1428	345	337	0.15	0.08	1.68	1.81	2.70	0.4-2
[02:53:52]	I53US	05:11:39	631	2440	358	5	0.15	0.04	1.32	1.12	4.42	0.7-3
12-Dec-14	I30JP	07:15:02	227	466	114	108	0.11	0.11	1.56	1.31	4.30	0.7-3
[06:48:11]	I45RU	08:23:05	425	1629	133	128	0.11	0.07	2.08	2.06	2.18	0.4-1.5
28-Nov-14 [11:47:18]	I36NZ	12:07:02	349	364	126	130	1.7	4.06	2.74	2.75	44.19	0.01-9
	I05AU	14:34:08	988	3150	111	112	1.7	0.24	9.69	10.11	3.32	0.05-4
	I22FR	14:48:58	749	3212	150	150	1.7	0.12	2.85	3.03	2.57	0.25-1.5
	I55US	15:06:37	270	3654	26	337	1.7	0.03	3.00	2.79	4.87	0.3-2
	I07AU	17:02:22	265	5590	134	133	1.7	0.07	3.41	3.36	1.79	0.25-1.1
26-Nov-14	I27DE	18:16:24	129	668	287	285	0.32	0.04	1.62	1.74	10.62	0.5-7.5
04-Nov-14	I45RU	21:17:01	631	1305	270	272	0.45	0.30	2.66	2.90	6.54	0.2-1
14-Oct-14	I39PW	12:48:17	590	2006	239	318	0.1	0.03	1.25	1.52	1.54	0.6-2.5
23-Aug-14	I05AU	08:42:45	463	2358	200	193	7.6	0.21	2.57	2.58	5.70	0.35-4
16-May-14	I36NZ	12:45:17	120	39	144	135	0.82	5.49	3.23	3.72	155.22	0.1-3
08-May-14	I04AU	21:57:32	401	2625	256	255	2.4	0.20	3.00	2.71	1.67	0.3-1.5
29-Mar-14 [13:45:41]	I07AU	15:15:05	490	1623	231	230	0.13	0.05	1.90	1.62	4.83	0.5-2
	I05AU	16:20:48	352	2802	295	294	0.13	0.02	1.89	1.63	2.61	0.5-1.8
	I06AU	16:34:18	778	3150	130	129	0.13	0.03	1.96	1.60	1.76	0.6-3
12-Jan-14 [16:00:48]	I19DJ	18:20:49	821	2526	111	113	0.24	0.12	3.42	4.01	3.87	0.2-6
	I33MG	18:49:41	141	3071	39	34	0.24	0.07	1.82	1.68	1.51	0.4-1.2
	I32KE	18:46:00	1059	3099	81	84	0.24	0.13	1.76	1.96	3.33	0.4-5
	I47ZA	21:09:43	369	5453	57	57	0.24	0.02	1.78	1.47	1.11	0.6-4
08-Jan-14	I39PW	18:39:41	427	1750	124	124	0.11	0.04	1.77	1.91	1.82	0.5-1.5
[17:05:34]	I07AU	19:25:07	276	2525	37	34	0.11	0.07	1.46	2.44	1.34	0.4-2.5
23-Dec-13 [08:30:57]	I48TN	08:56:43	309	764	305	308	0.43	0.34	1.41	1.58	3.73	0.45-7
	I26DE	09:49:37	239	1394	226	214	0.43	0.24	2.31	2.17	5.14	0.4-2
	I31KZ	12:31:58	176	4459	277	276	0.43	0.03	1.73	1.93	1.94	0.3-1

08-Dec-13 [03:10:09]	I59US	04:47:17	258	1730	330	333	0.2	0.04	1.68	1.54	2.47	0.6-2
21-Nov-13 [01:50:35]	I43RU	03:05:28	262	1343	187	175	0.23	0.13	2.03	2.19	1.30	0.3-2.5
	I31KZ	03:35:04	72	1812	258	256	0.23	0.06	1.65	2.05	2.32	0.25-3
12-Oct-13 [16:06:45]	I50GB	17:33:37	992	1690	222	221	3.5	0.65	4.81	5.98	4.66	0.1-5
	I17CI	19:26:10	820	3617	217	218	3.5	0.35	5.92	7.77	10.36	0.05-1.8
	I35NA	20:15:49	498	4461	263	253	3.5	0.06	10.44	8.81	1.42	0.05-1
	I32KE	22:48:03	764	7011	249	250	3.5	0.15	6.76	6.35	4.06	0.05-2
31-Jul-13 [03:50:14]	I05AU	05:15:23	354	1512	318	323	0.22	0.11	1.52	1.85	6.02	0.5-4
27-Jul-13 [08:30:36]	I39PW	10:52:51	544	2532	108	103	0.36	0.10	3.24	3.01	1.83	0.3
	I22FR	11:03:19	360	2754	334	336	0.36	0.09	1.98	2.00	4.16	0.4
30-Apr-13 [08:40:38]	I42PT	09:05:32	486	460	212	216	10	1.27	6.77	8.03	10.89	0.2-8
21-Apr-13 [06:12:12]	I41PY	07:00:42	600	747	253	251	2.5	3.21	6.16	5.06	32.84	0.07-8
	I08BO	07:41:05	163	1380	164	163	2.5	0.01	0.75	0.98	1.44	1-3
	I09BR	08:20:53	1076	2198	228	226	2.5	0.90	4.91	4.88	11.92	0.04-4
	I02AR	09:10:49	276	2953	5	4	2.5	0.05	1.79	1.16	2.20	0.6-3
	I11CV	12:32:59	469	6566	223	226	2.5	0.08	4.12	4.71	1.29	0.3-2
	I31KZ	03:48:08	1026	530	22	29	440	12.24	37.99	45.51	76.90	0.01-4
	I43RU	05:02:09	2142	1502	88	97	440	1.58	38.48	30.06	13.67	0.01-3
	I46RU	04:44:29	701	1532	283	268	440	2.52	21.08	16.72	35.76	0.02-4
	I34MN	06:14:55	924	3185	301	230	440	0.50	22.79	30.34	4.40	0.03-2
	I26DE	07:10:31	812	3257	60	56	440	0.97	28.98	29.26	2.89	0.03-3
	I18DK	08:17:13	1948	4893	39	17	440	2.73	49.99	69.72	13.75	0.01-3
	I45RU	07:55:27	887	5022	310	305	440	1.34	38.45	21.01	1.07	0.02-3
	I44RU	08:50:55	1471	5798	314	302	440	0.90	19.28	60.68	4.03	0.02-3
	I53US	09:36:30	1660	6481	341	339	440	12.62	25.69	19.74	165.14	0.02-4
	I10CA	11:29:57	1107	8147	14	355	440	2.75	32.53	36.41	5.55	0.01-1
	I33MG	11:20:35	720	8311	8	12	440	1.94	47.96	43.12	2.07	0.01-0.2
	I56US	11:35:08	1621	8554	1	352	440	1.59	29.45	30.91	7.61	0.015-3
	I57US	13:10:00	2000	10182	1	2	440	1.59	28.45	27.31	3.42	0.01-1

	I59US	13:42:44	377	11030	339	316	440	0.39	84.70	81.92	2.48	0.01-0.1
	I27DE	17:50:43	830	14983	49	61	440	1.86	45.15	44.28	3.76	0.01-0.1
20-Nov-12 [20:37:31]	I32KE	21:24:19	452	905	297	299	0.089	0.18	1.24	1.11	43.34	0.2-6
	I19DJ	22:14:13	391	1799	237	238	0.089	0.01	2.37	2.28	3.21	0.4-2.5
18-Sep-12 [19:34:39]	I09BR	21:21:14	388	1928	346	348	0.67	0.02	2.75	2.53	2.43	0.3-1.5
	I08BO	22:03:23	115	2633	44	42	0.67	0.03	0.90	0.91	2.04	1-1.8
10-Sep-12 [01:03:32]	I02AR	03:34:48	435	2757	215	215	0.082	0.09	2.23	1.01	1.52	0.5-2.5
26-Aug-12 [14:55:47]	I39PW	16:55:05	270	1980	285	282	0.68	0.02	1.40	1.11	2.44	0.6-2.5
12-Mar-12 [06:40:44]	I39PW	07:25:22	86	807	134	136	0.3	0.05	1.71	1.44	1.32	0.5-2
	I30JP	09:58:59	140	3648	181	238	0.3	0.42	2.03	1.81	37.04	0.5-3
04-Feb-12 [14:42:51]	I48TN	15:33:22	95	929	249	248	0.43	0.07	1.43	1.38	1.08	0.6-5.5
15-Jan-12 [12:26:20]	I55US	14:39:53	207	2422	276	272	0.076	0.01	0.92	1.02	1.51	0.9-3
25-May-11 [05:40:02]	I35NA	08:05:51	444	2619	351	353	4.8	0.08	2.31	1.78	1.72	0.4-2
06-Apr-11 [08:30:55]	I18DK	09:24:54	593	1051	121	116	0.43	0.45	3.15	3.90	9.57	0.3-3
01-Mar-11 [10:37:54]	I34MN	11:16:27	186	658	345	315	0.13	0.10	2.48	2.77	2.47	0.3-1
21-Feb-11 [05:07:03]	I31KZ	07:45:50	562	2946	210	207	0.13	0.31	3.04	3.28	27.48	0.2-6
	I30JP	00:59:24	560	1603	74	72	33	0.59	6.61	6.88	0.79	0.2-2
	I44RU	00:58:16	544	1680	179	178	33	0.61	2.76	3.14	4.82	0.3-3
	I45RU	01:33:35	610	2276	99	93	33	0.74	3.37	3.26	8.06	0.25-3
	I39PW	03:39:50	649	4127	31	36	33	2.32	12.49	11.70	1.88	0.06-1
	I34MN	03:28:44	769	4257	85	15	33	0.02	1.90	2.34	1.09	0.4-3
	I53US	03:41:02	594	4572	256	256	33	2.02	8.35	8.19	35.92	0.1-3
	I56US	05:46:23	309	6625	295	295	33	0.78	15.63	15.17	3.43	0.01-1.3
	I18DK	05:40:26	1075	6758	318	308	33	0.49	11.32	11.38	7.04	0.07-2

25-Dec-10

[23:24:00]

	I10CA	06:41:36	677	7837	307	308	33	0.52	9.88	9.75	3.43	0.1-1.5
	I55US	11:33:45	737	12885	352	347	33	0.13	18.44	15.46	4.54	0.04-1
	I08BO	13:48:06	212	14887	308	156	33	0.10	7.91	7.06	1.11	0.1-0.8
03-Sep-10 [12:04:58]	I55US	13:59:19	562	2005	326	339	3.8	0.42	7.54	7.73	7.54	0.1-6
	I05AU	14:04:10	202	2059	182	184	3.8	0.07	1.86	1.88	1.49	0.5-2.5
	I04AU	15:55:58	841	3642	153	142	3.8	0.12	13.43	13.11	4.75	0.05-0.1
	I07AU	16:42:03	250	4668	171	166	3.8	0.08	11.60	9.10	1.22	0.03-0.15
08-Mar-10 [22:02:07]	I10CA	01:21:20	299	2041	172	246	0.85	0.01	0.81	1.10	3.22	0.7-3
28-Feb-10 [22:24:50]	I26DE	23:04:18	111	534	89	88	0.44	0.36	2.68	2.73	2.55	0.3-1.5
	I43RU	23:38:58	559	1404	238	235	0.44	0.68	2.49	2.59	6.61	0.3-3
	I31KZ	00:45:11	1139	2651	280	276	0.44	0.32	2.15	2.51	22.70	0.35-3.5
	I46RU	02:29:27	833	4320	289	274	0.44	0.13	2.98	3.11	2.49	0.3-2
15-Jan-10 [19:17:54]	I32KE	20:35:00	488	1342	234	231	1.2	0.07	2.07	2.31	4.88	0.4-3.5
	I35NA	20:40:38	596	1581	41	35	1.2	0.48	3.08	3.85	36.82	0.2-3.5
	I47ZA	21:27:37	241	2267	5	2	1.2	0.06	1.76	1.93	2.61	0.4-2
21-Nov-09 [20:53:00]	I35NA	21:58:54	568	1249	107	107	18	0.48	3.47	3.98	27.22	0.2-8
	I49GB	00:56:30	60	4312	79	76	18	3.17	12.02	10.24	1.70	0.05-1
	I17CI	01:29:58	109	4892	132	132	18	0.01	1.35	1.37	1.33	0.6-1.5
08-Oct-09 [02:57:00]	I39PW	04:50:53	151	2024	230	274	33	1.12	6.23	6.40	0.48	0.08-1.5
	I07AU	04:56:20	925	2296	318	317	33	1.13	3.18	3.25	2.73	0.4-6
	I04AU	05:59:50	954	3408	8	9	33	0.20	3.60	2.66	9.26	0.3-6
	I30JP	07:37:47	457	4851	209	211	33	0.11	1.79	1.68	2.19	0.5-1.5
	I05AU	07:48:12	411	5030	320	317	33	0.31	3.88	3.53	2.50	0.2-2.5
	I22FR	07:50:18	649	5362	285	286	33	0.14	4.06	3.79	1.66	0.1-2
	I45RU	08:11:17	755	5500	195	197	33	1.18	10.46	9.87	5.85	0.05-2
	I44RU	09:50:22	914	7254	222	222	33	0.62	6.58	7.55	20.65	0.1-1.5
	I55US	10:58:30	475	8620	312	315	33	0.12	6.14	6.16	2.31	0.1-1
	I53US	12:50:45	551	10503	270	270	33	0.43	11.78	12.60	7.00	0.05-1
	I18DK	14:19:35	671	11816	350	338	33	0.48	11.50	11.54	3.24	0.08-1
	I56US	15:04:50	645	12693	293	319	33	0.76	13.83	12.80	33.55	0.05-1.5

04-Sep-09 [02:23:18]	I34MN	17:06:08	484	653	153	86	2.3	0.10	7.50	7.45	1.23	0.08-1
23-Aug-09	I27DE	22:31:17	380	1092	85	85	0.75	0.13	2.44	3.15	13.33	0.35-3
10-Apr-09	I47ZA	20:22:29	87	1788	179	174	0.73	0.02	1.90	2.18	1.46	0.4-1.5
07-Feb-09 [19:51:32]	I46RU	20:41:53	562	994	293	296	3.5	0.29	1.93	2.37	56.58	0.4-3
	I34MN	22:15:51	342	2641	305	250	3.5	0.38	3.32	2.56	11.62	0.1-2
	I45RU	23:53:50	580	4446	311	296	3.5	0.06	2.38	2.07	3.27	0.4-1.5
	I18DK	00:31:39	813	4817	32	23	3.5	0.09	3.59	2.81	4.24	0.3-2
	I44RU	00:58:43	339	5246	311	304	3.5	0.05	2.11	1.52	1.35	0.5-2
	I53US	01:46:14	397	6137	3352	336	3.5	0.31	6.90	7.06	3.54	0.1-2
21-Nov-08 [00:26:44]	I56US	01:13:27	159	740	41	42	0.41	0.28	3.73	3.66	1.40	0.1-1.66
	I10CA	01:17:40	420	1009	294	291	0.41	1.57	3.95	3.66	48.24	0.1-2
	I18DK	03:27:19	658	3177	235	225	0.41	0.47	4.56	5.46	15.83	0.15-3.8
07-Oct-08 [02:45:45]	I32KE	05:08:16	266	2532	347	347	1	0.03	3.31	4.18	2.54	0.2-0.8
	I31KZ	06:22:36	556	4024	225	222	1	0.13	3.39	3.47	1.36	0.2-3
23-Jul-08 [14:45:25]	I31KZ	16:03:25	569	1530	145	146	0.36	0.16	3.12	2.45	8.84	0.2-5.8
	I46RU	16:42:09	381	2130	224	227	0.36	0.05	2.45	3.01	2.60	0.3-0.85
08-Jul-08 [15:55:30]	I53US	18:25:22	298	2594	318	319	0.21	0.01	3.27	3.20	1.35	0.3-1.2
01-Jul-08	I53US	21:22:51	151	3737	130	141	0.12	0.03	1.69	1.40	3.62	0.4-3
27-Jun-08	I49GB	03:04:07	449	1240	335	339	0.49	0.41	2.74	2.12	4.73	0.3-1.5
17-Feb-08 [12:19:16]	I18DK	12:40:01	287	334	201	191	0.33	0.11	3.05	3.18	2.44	0.3-2.5
09-Jan-08 [03:53:15]	I02AR	05:03:59	564	1359	180	177	0.14	0.19	1.67	1.65	4.42	0.5-5
12-Oct-07 [09:14:03]	I18DK	10:42:15	217	1528	359	355	0.11	0.08	2.20	2.38	1.46	0.4-2
	I53US	11:49:39	520	2815	357	358	0.11	0.23	4.89	4.48	11.61	0.1-3.5
22-Sep-07 [17:57:12]	I02AR	19:09:41	341	1379	288	296	0.65	1.57	2.51	3.06	36.95	0.3-5
18-Apr-07 [12:44:23]	I55US	13:27:05	373	754	160	156	0.33	1.43	6.89	6.83	69.60	0.05-9

17-Mar-07 [06:48:35]	I17CI	07:43:53	262	990	87	88	0.13	0.11	1.64	1.59	4.53	0.2-2
22-Jan-07 [07:24:56]	I31KZ	07:52:34	265	651	213	206	0.24	2.19	3.22	3.33	11.41	0.3-9
	I46RU	09:28:05	514	2421	260	261	0.24	0.41	3.02	2.48	19.84	0.2-2
09-Dec-06 [06:31:12]	I26DE	09:09:11	251	2733	153	150	14	0.39	5.37	4.88	2.42	0.05-1
	I35NA	11:15:33	1350	5129	11	133	14	0.16	5.49	4.89	1.80	0.2-1.5
14-Oct-06 [18:10:49]	I53US	20:22:29	661	2340	236	236	0.7	0.04	2.87	2.16	3.11	0.4-1.5
02-Sep-06 [04:26:15]	I04AU	06:34:36	761	2404	341	342	2.8	1.67	7.14	6.61	33.96	0.05-6
	I07AU	07:06:08	433	2760	280	277	2.8	0.17	1.55	1.77	2.04	0.4-4
	I22FR	10:20:04	256	6137	268	261	2.8	0.23	10.68	10.78	3.30	0.07-0.2
15-Jul-06 [23:55:45]	I55US	02:41:20	239	2660	184	188	0.26	0.07	2.86	2.88	3.49	0.3-3
07-Jun-06 [00:06:28]	I26DE	02:09:44	504	2313	9	8	0.19	0.03	2.95	2.38	3.50	0.2-2
	I31KZ	02:46:15	429	2806	331	335	0.19	0.02	4.73	4.71	2.31	0.1-1.5
28-Jan-06 [03:33:48]	I47ZA	06:59:36	210	3637	144	144	1.8	0.02	1.54	1.37	1.09	0.5-1.5
	I33MG	07:04:01	372	3721	170	171	1.8	0.09	2.16	2.24	2.07	0.5-2

Table A.2: Summary of bolides infrasound signal measurements of 50 individual bolide events as detected from 88 infrasound stations from Ens et al. (2012), not included in Table A.1. These measurements are strictly from Ens et al. (2012) except for two events September 3, 2004 and March 27, 2003 where we have independently repeated the inframeasure analysis.

Date/ [Time]	**Station**	**Arrival time (UT)**	**Dur-ation (s)**	**Range (km)**	**Theo. Az (deg)**	**Obs. Az (deg)**	**Satellite Energy (kT)**	**P2P Amp (Pa)**	**Period @Max Amp (s)**	**Period @Max PSD (s)**	**Bolide Integ. Energy SNR**	**Band-pass (Hz)**
22-Jul-08 [19:34:00]	IS09BR	23:32:06	765	4384	261	248	0.25	0.12	6.69	7.25	2.29	0.08-0.65
07-Apr-08 [01:02:28]	IS41PY	1:35:41	248	618	191	192	0.08	0.17	1.69	2.38	4.99	0.31-9.8
	IS09BR	3:00:34	413	2087	209	209	0.08	0.11	4.28	3.85	2.19	0.13-1.8
10-Mar-08 [17:16:08]	IS56US	19:38:11	62	2724	75	82	0.05	0.1	1.2	1.74	2.88	0.3-3.5

26-Dec-07 [06:46:20]	IS05AU	10:19:02	432	4066	140	131	0.4	0.11	4.32	4.63	0.95	0.2-0.7
07-Nov-07 [22:31:27]	IS33MG	1:20:26	219	3023	36	35	0.05	0.02	3.11	2.77	1.62	0.25-1.13
24-Oct-07 [20:28:29]	IS52GB	21:52:43	198	1497	38	31	0.02	0.08	3.13	3.72	1.05	0.2-1.8
22-Oct-07 [20:10:30]	IS31KZ	23:34:32	418	3711	313	305	0.04	0.05	2.51	2.08	1.99	0.32-1.6
28-May-07 [20:46:39]	IS46RU	22:15:15	192	1524	30	7	0.05	0.07	2.72	2.38	1.08	0.28-1.5
	IS31KZ	23:11:19	390	2950	41	30	0.05	0.03	2.16	2.37	5.24	0.21-3
16-May-07 [16:20:58]	IS39PW	18:50:16	1863	2866	243	242	0.16	0.07	2.18	2.99	1.93	0.3-2.5
16-May-07 [21:28:54]	IS26DE	22:14:31	296	788	79	83	0.02	0.17	0.87	1.08	3.7	0.18-7.5
09-Feb-02 [19:50:26]	IS07AU	20:20:07	277	384	92	77	0.16	1.65	1.71	3.2	6.51	0.09-9.9
17-Jan-07 [09:50:46]	IS35NA	13:18:06	66	3768	77	80	1.36	0.11	3.11	3.3	0.94	0.2-2
	IS33MG	10:57:45	183	1212	18	14	1.36	0.45	3.16	3.59	2.63	0.16-0.9
	IS32KE	11:20:59	593	1757	118	121	1.36	0.64	2.74	3.62	6.24	0.17-8
06-Dec-06 [07:51:07]	IS07AU	9:19:05	40	1370	226	232	0.02	0.05	2.11	3.41	3.12	0.09-1.3
	IS04AU	8:45:58	261	1036	54	48	0.02	0.14	2.17	2.59	5.79	0.2-8
1-Dec-06 [06:09:25]	IS47ZA	7:48:59	199	1784	19	18	0.21	0.12	1.96	1.39	2.6	0.4-1.9
	IS35NA	7:30:50	280	1540	68	65	0.21	0.17	1.71	2.93	2.44	0.44-1.9
	IS32KE	7:34:03	513	1511	206	208	0.21	0.06	3.5	4.68	1.49	0.16-2.6
02-Oct-06 [19:10:27]	IS33MG	22:35:52	958	3725	10	11	0.25	0.12	3.27	3.51	3.94	0.08-1.4
	IS32KE	21:31:54	582	2467	46	45	0.25	0.07	5.39	4.12	3.3	0.11-1.8
11-Sep-06 [12:41:22]	IS53US	13:27:13	398	841	243	237	0.09	0.18	1.79	2.17	15.15	0.16-4.5
17-Aug-06 [10:43:34]	IS39PW	14:25:06	485	4029	121	114	0.63	0.07	1.7	1.57	2.36	0.48-2.2
	IS22FR	11:51:16	243	1221	357	353	0.63	0.26	3.22	2.73	1.7	0.3-4

15-Aug-06 [10:52:24]	IS32KE	12:16:43	708	1575	64	67	0.16	0.07	2.05	2.16	0.03	0.305-3
09-Aug-06 [04:30:44]	IS33MG	5:12:52	556	804	128	124	2.32	1.32	5.98	6.11	1.9	0.09-0.7
	IS32KE	7:16:13	798	3037	144	147	2.32	0.2	5.12	4.58	5.63	0.04-2.3
	IS26DE	12:47:43	595	8929	143	146	2.32	0.05	10.72	8.9	0.6	0.072-0.45
16-Jul-06 [23:55:45]	IS55US	2:41:43	116	2660	187	189	0.27	0.12	3.61	4.02	2.07	0.15-1
21-May-06 [07:51:11]	IS50GB	9:02:04	537	1283	251	251	0.6	0.39	3.96	3.05	2.04	0.3-4
	IS17CI	10:35:47	3218	3055	228	228	0.6	0.2	4.21	8.45	5.87	0.07-2.5
	IS09BR	10:18:27	69	2475	82	78	0.6	0.03	3.15	5.39	2.73	0.16-2.3
14-Mar-06 [03:21:06]	IS08BO	5:47:47	389	2664	9	11	0.3	0.09	3.74	4.93	7.74	0.18-0.4
06-Feb-06 [01:57:37]	IS35NA	5:39:16	674	3923	179	177	2.93	0.09	9.29	7.95	2.73	0.05-0.3
09-Nov-05 [07:33:08]	IS22FR	9:43:27	851	2291	240	237	0.66	0.09	9.81	8.07	1.85	0.1-0.9
	IS07AU	9:07:59	319	1689	139	141	0.66	0.23	2.53	2.51	1.41	0.31-3.2
	IS05AU	8:43:53	402	1291	354	352	0.66	0.09	2.73	2.41	3.26	0.29-1.3
26-Oct-05 [21:30:47]	IS41PY	23:44:51	728	2460	237	237	0.43	0.1	6.45	6.45	4.09	0.1-1.1
	IS14CL	21:48:21	318	334	177	206	0.43	0.97	4.8	6.02	7.9	0.1-9.3
	IS08BO	23:53:54	447	2532	207	205	0.43	0.16	4.27	3.86	3.17	0.11-1.2
04-Sep-05 [23:04:36]	IS49GB	0:38:42	297	1862	277	274	0.14	0.35	1.89	1.55	4.52	0.3-4
	IS09BR	1:23:16	448	2514	144	140	0.14	0.12	2.25	2.02	2.9	0.28-3.5
15-Apr-05 [06:54:59]	IS41PY	9:02:14	594	2446	213	225	0.08	0.04	2.07	1.87	2.21	0.36-2.2
06-Mar-05 [14:12:23]	IS35NA	14:57:40	358	835	27	25	0.09	0.14	1.08	1.28	4.53	0.29-4.9
	IS32KE	16:18:16	455	2148	234	244	0.09	0.06	3	2.69	2.8	0.21-0.7
01-Jan-05 [03:44:09]	IS31KZ	7:34:08	241	4191	260	254	0.94	0.12	3.38	3.76	2.13	0.2-1.8
29-Dec-04 [07:11:45]	IS22FR	9:34:35	586	2743	61	58	0.15	0.15	3.58	5.29	2.51	0.21-3.6

11-Dec-04 [15:36:51]	IS34MN	16:50:12	379	1437	190	182	0.09	0.2	3.06	3.1	4.74	0.218-5
05-Dec-04 [17:14:11]	IS07AU	19:18:22	684	2187	127	125	0.07	0.16	1.92	2.07	2.99	0.22-2.6
	IS05AU	18:24:01	270	1382	23	35	0.07	0.08	2.77	2.82	1.7	0.31-4.5
07-Oct-04 [13:14:43]	IS55US	20:03:44	471	7189	263	270	18.42	0.25	11.43	14.12	4.17	0.05-0.6
	IS52GB	15:15:33	857	2218	181	177	18.42	0.28	8.96	9.81	1.26	0.089-2
	IS26DE	23:07:07	4230	10221	131	127	18.42	0.13	15.9	17.86	1.51	0.03-0.2
	IS10CA	6:20:13	2374	17256	27	24	18.42	0.09	15.71	10.08	0.02	0.04-0.2
03-Sep-04 [12:07:24]	IS27DE	13:18:45	1150	1088	85	91	13	0.82	45.72	40.96	19.53	0.015-0.08
	IS55US	15:54:02	1119	3716	201	213	13	0.91	20.66	21.85	43.79	0.04-3
	IS35NA	17:18:04	1212	5394	180	173	13	0.21	13.14	14.5	1.96	0.02-3
11-Jun-04 [10:51:17]	IS08BO	12:17:42	311	1576	251	242	0.06	0.05	2.93	1.38	1.8	0.298-3
03-Jun-04 [09:40:12]	IS57US	11:13:47	307	1671	345	342	0.14	0.07	4.09	3.15	3.75	0.14-2.9
	IS56US	9:59:13	161	378	267	264	0.14	0.05	2.97	2.73	3.53	0.2-2
	IS53US	12:04:01	222	2417	130	143	0.14	0.03	1.13	1.97	3.16	0.45-2.7
22-Apr-04 [21:19:55]	IS33MG	22:18:00	59	930	65	66	0.37	0.1	2.95	3.41	2.95	0.3-3.14
17-Aug-03 [13:16:07]	IS55US	19:33:41	239	6664	226	237	1.62	0.04	3.93	5.69	1.64	0.18-1.5
	IS33MG	15:35:40	206	2565	207	205	1.62	0.16	3.65	4.65	1	0.16-1.1
27-Mar-03 [05:50:26]	IS10CA	6:56:00	450	1143	136	151	0.15	0.14	2	2.21	7.95	0.3-3
10-Nov-02 [22:13:54]	IS59US	23:18:19	362	1142	252	250	1.17	4.13	5.12	6.61	123.79	0.015866-9.9
09-Oct-02 [12:00:35]	IS59US	14:49:31	635	3427	223	212	0.19	0.1	5.18	4.68	1.73	0.08-4
14-Aug-02 [07:48:32]	SSG0	12:38:59	504	5056	198	207	0.27	0.06	3.78	4.76	1.7	0.1-2.2
	nSts	12:34:10	381	4943	195	199	0.27	0.06	2.61	2.45	1.98	0.15-1.3
	IS59US	11:51:53	574	4387	130	130	0.27	0.13	3.29	4.1	3.87	0.08-1.5
25-Jul-02 [15:57:32]	IS33MG	16:56:29	236	1078	183	178	0.69	0.25	4.08	4.76	3.56	0.17-3

13-Jun-02 [15:29:38]	IS07AU	17:45:05	293	2417	252	250	0.56	0.05	3.89	3.5	2.59	0.25-2.3
06-Jun-02 [04:28:30]	IS26DE	5:59:48	2081	1757	157	160	7.58	1.66	13.33	13.16	14.29	0.025-6.2
09-Mar-02 [01:20:24]	PSDI	6:20:20	372	5431	234	250	0.61	0.47	5	4.93	2.83	0.08-2.2
	nSts	5:31:42	428	4583	232	241	0.61	0.22	4.48	4.43	1.82	0.15-4
	IS59US	2:58:00	489	1689	147	146	0.61	0.36	8.51	10.24	3.92	0.052-5
23-Jul-01 [22:19:00]	EC1	22:37:47	267	323	354	11	2.87	1.62	2.82	2.77	8.61	0.1-39
23-Apr-01 [06:12:00]	SSG0	8:09:42	442	2039	248	252	8.97	1.1	4.11	5.12	27.72	0.05-7.5
	NSV0	7:53:05	454	1752	235	237	8.97	6.23	4.67	5.18	20.68	0.05-5
	nSts	7:55:25	863	1835	245	241	8.97	1.19	3.77	8.62	22.49	0.03-6.5
	IS59US	8:21:55	779	2526	62	61	8.97	0.55	4.96	4.22	7.56	0.02-9.3
	IS57US	7:49:04	400	1670	254	255	8.97	19.07	4.27	4.14	25.45	0.03-9.3
	IS26DE	16:22:12	781	10810	331	324	8.97	0.09	7.5	6.83	1.98	0.07-0.8
	DSLI	8:40:06	934	2627	259	261	8.97	0.26	4.01	4.46	2.59	0.1-2
25-Aug-00 [01:12:25]	DSLI	3:25:16	809	2382	179	185	3.15	0.07	6.77	5.61	9.74	0.04-2.5
19-Jul-00 [17:40:25]	WSRA	21:36:46	208	4231	266	262	0.37	0.38	3.51	3.1	0.16	0.18-1.5

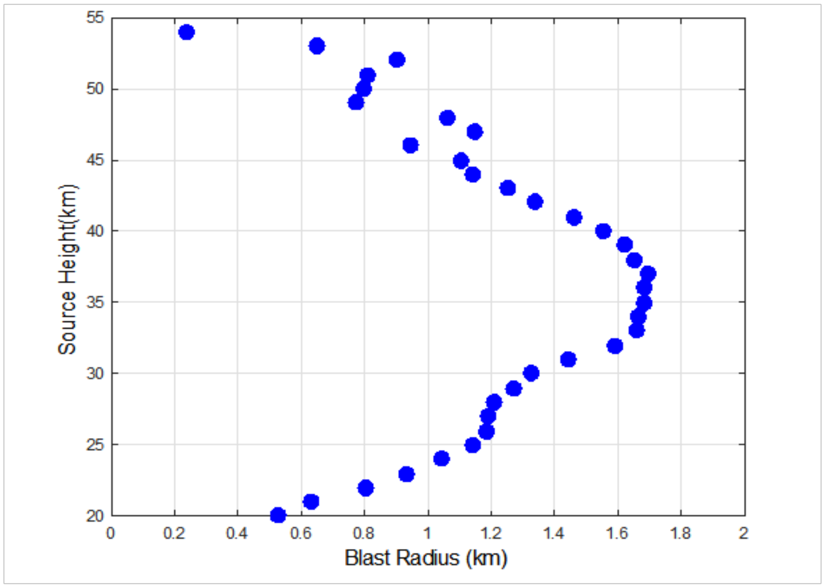

Figure A.4: Blast radius plot for the Park Forest meteorite dropping fireball of March 23, 2004.

Appendix B

Supplementary Material for Chapter 4

B.1 Summary of the 18 fireball events and three calibration events (E > 2 kT)

Table B.1 summarizes 21 fireball events (E > 2 kT) that were used in chapter 4 analysis. The table provides time, location, height and velocity at the peak brightness, entry angle from the horizontal line, and JPL energy.

B.2 Triggered Progressive Fragmentation Model (TPFM)

B.2.1 TPFM Model Code

The original TPFM code, **tpfm-mod4f** in FORTRAN was developed by D. O. ReVelle at Los Alamos National Laboratory from May 2001 to June 2003. In December 2015, E. Stokan updated the FORTRAN code and wrote the Monte Carlo wrapper code in MATLAB. Fig. B.1 is a screen shot of the first few lines of MATALB code showing an example of input parameters for the Marshall Islands fireball. The MATLAB wrapper code calls the original FORTRAN code and produces 5 output files: **AFTAC.TXT**, **BOL.TXT**, **EFFCNCY.TXT**, **IO.TXT** and **LCRV.TXT**. IO.TXT provides a summary of the simulation settings, verifying that input parameters were correctly used. Details on the other four output files are given in Table B.2 - B.5.

Table B.1: Summary of the 18 energetic fireball events (E > 2 kT) and three of the five calibration events (highlighted in grey): the Marshall Islands fireball (February 1, 1994), the Tagish Lake fireball (January 18, 2000), the Antarctica fireball (September 3, 2004) as taken from NASA JPL fireball website. Of all JPL fireball events that are > 2 kT, we selected only events that have data on velocity as well as height and geographic location at peak brightness. For the three calibration fireball events which had E > 2 kT, the height and velocity were taken from Tagliaferri et al. (1995), Brown et al. (2002b), and Klekociuk et al. (2005), respectively. The energy estimated on the JPL site follows the procedure described in Brown et al. (2002a). Entry angle is from the horizontal.

Date (yyyy/mm/dd) / Time (UT)	Latitude (°N)	Longitude (°E)	Height (km)	Velocity (km/s)	Entry angle (°)	Energy (kT)
1994-02-01 / 22:30	2.7	164.1	21	25	45	30
2000-01-18 / 16:43	60.3	-134.6	32	15.8	17.8	2.4
2003-09-27 / 12:59	21	86.6	26	18.2	38.5	4.6
2004-06-05 / 20:34	1.3	-174.4	43	19.5	34.5	3.9
2004-09-03 / 12:07	-67.7	18.8	25	13	41.9	13
2004-10-07 / 13:14	-27.3	71.5	35	19.2	27.2	18
2006-09-02 / 04:26	-14	109.1	44.1	14.2	63.1	2.8
2009-02-07 / 19:51	56.6	69.8	40	15.4	65.7	3.5
2009-09-04 / 02:23	42.5	110	28.3	24	50.9	2.3
2009-10-08 / 02:57	-4.2	120.6	19.1	19.2	67.5	33
2009-11-21 / 20:53	-22	29.2	38	32.1	8.6	18
2010-07-06 / 23:54	-34.1	-174.5	26	15.7	43.9	14
2010-09-03 / 12:04	-61	146.7	33.3	12.3	59.6	3.8
2010-12-25 / 23:24	38	158	26	18.1	60.9	33
2013-04-21 / 06:23	-28.1	-64.6	40.7	14.9	40.8	2.5
2013-04-30 / 08:40	35.5	-30.7	21.2	12.1	39.5	10
2013-10-12 / 16:06	-19.1	-25	22.2	12.8	40.9	3.5
2014-05-08 / 19:42	-36.9	87.3	35.4	19	83.4	2.4
2014-08-23 / 06:29	-61.7	132.6	22.2	16.2	42.1	7.6
2015-09-07 / 01:41	14.5	98.9	29.3	21	45.4	3.9
2016-02-06 / 13:55	-30.4	-25.5	31	15.6	21.9	13

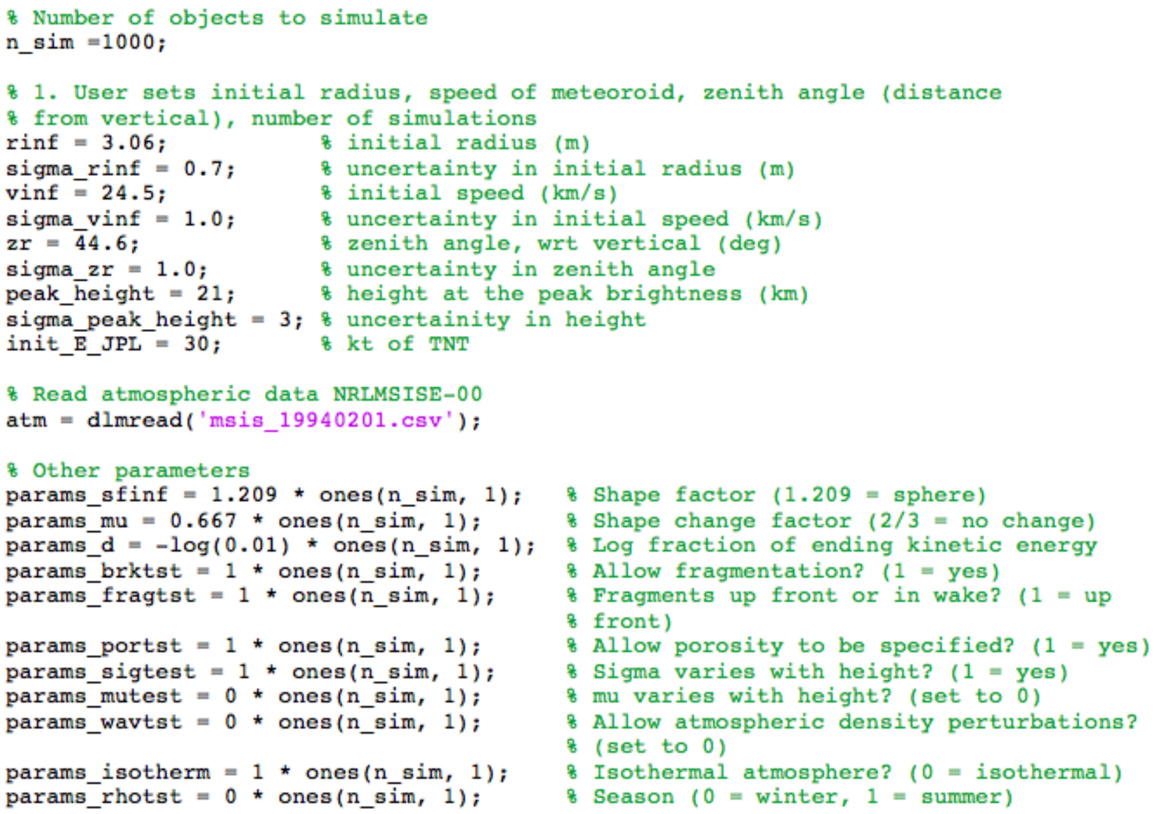

```
% Number of objects to simulate
n_sim =1000;

% 1. User sets initial radius, speed of meteoroid, zenith angle (distance
% from vertical), number of simulations
rinf = 3.06;           % initial radius (m)
sigma_rinf = 0.7;      % uncertainty in initial radius (m)
vinf = 24.5;           % initial speed (km/s)
sigma_vinf = 1.0;      % uncertainty in initial speed (km/s)
zr = 44.6;             % zenith angle, wrt vertical (deg)
sigma_zr = 1.0;        % uncertainty in zenith angle
peak_height = 21;      % height at the peak brightness (km)
sigma_peak_height = 3; % uncertainity in height
init_E_JPL = 30;       % kt of TNT

% Read atmospheric data NRLMSISE-00
atm = dlmread('msis_19940201.csv');

% Other parameters
params_sfinf = 1.209 * ones(n_sim, 1);    % Shape factor (1.209 = sphere)
params_mu = 0.667 * ones(n_sim, 1);       % Shape change factor (2/3 = no change)
params_d = -log(0.01) * ones(n_sim, 1);   % Log fraction of ending kinetic energy
params_brktst = 1 * ones(n_sim, 1);       % Allow fragmentation? (1 = yes)
params_fragtst = 1 * ones(n_sim, 1);      % Fragments up front or in wake? (1 = up
                                          % front)
params_portst = 1 * ones(n_sim, 1);       % Allow porosity to be specified? (1 = yes)
params_sigtest = 1 * ones(n_sim, 1);      % Sigma varies with height? (1 = yes)
params_mutest = 0 * ones(n_sim, 1);       % mu varies with height? (set to 0)
params_wavtst = 0 * ones(n_sim, 1);       % Allow atmospheric density perturbations?
                                          % (set to 0)
params_isotherm = 1 * ones(n_sim, 1);     % Isothermal atmosphere? (0 = isothermal)
params_rhotst = 0 * ones(n_sim, 1);       % Season (0 = winter, 1 = summer)
```

Figure B.1: An example of input parameters for the Marshall Islands fireball written in MATLAB.

Table B.2: Contents of AFTAC.TXT.

Column	Variable	Description
1	TT (s)	Time
2	LOGLGHT (W)	Base 10 logarithm of meteor light output
3	LIGHT (W)	Meteor light output

Table B.3: Contents of BOL.TXT. *Theoretical* outputs are computed with no fragmentation and negligible deceleration.

Column	Variable	Description
1	TT (s)	Time
2	LIGHT (W)	Meteor light output
3	ZZ (km)	Height
4	TAUSEP (%)	Differential luminous efficiency
5	IOIM	*Theoretical* normalized meteor light output
6	MAG	Meteor absolute magnitude
7	SIG (s^2/km^2)	Ablation coefficient
8	KEKT (kT)	Meteoroid kinetic energy
9	PSTAG (Pa)	Stagnation pressure of flow around meteoroid
10	DIDT (d(IOIM)/dt, s^{-1})	*Theoretical* normalized change in meteor light
11	VELO (km/s)	Meteoroid speed

Table B.4: Contents of EFFCNCY.TXT. Note that all the efficiencies here (except ACEFF) are differential (i.e. instantaneous) and fractional.

Column	Variable	Description
1	TT (s)	Time
2	KEKT (kT)	Meteoroid kinetic energy
3	KE (J)	Meteoroid kinetic energy
4	ZZ (km)	Height
5	DHEFF	Heating efficiency
6	TAUSEP	Luminous efficiency
7	DACEFF	Acoustic efficiency
8	DIEFF	Ionization efficiency
9	CHECKSUM	Sum of differential efficiencies (≈ 1)
10	DDISS	Dissociation efficiency
11	DLTA	Relative difference between current σ to initial value
12	ACEFF	Integrated acoustic efficiency

Table B.5: Contents of LCRV.TXT.

Column	Variable	Description
1	TT (s)	Time
2	MZ (kg)	Mass of each meteoroid fragment
3	MZSB (kg)	*Theoretical* meteoroid mass
4	ZZ (km)	Height
5	PSTAG (Pa)	Stagnation pressure of flow around meteoroid
6	TSTRNGTH (Pa)	Meteoroid strength
7	TAUSEP (%)	Differential luminous efficiency
8	RSB (m)	*Theoretical* meteoroid radius
9	RADZ (m)	Meteoroid radius
10	ACEFF	Acoustic efficiency, fractional
11	DACEFF	Differential acoustic efficiency, fractional
12	MAG	Meteor absolute panchromatic magnitude
13	LIGHT (W)	Meteor light output
14	NUMBPIEC	Number of fragments
15	SIG (s^2/km^2)	Ablation coefficient
16	VELO (km/s)	Meteoroid speed
17	KN (mean free path/radius)	Knudsen number
18	PSTARZ (Pa)	Ballistic parameter
19	PSTARZSB (Pa)	*Theoretical* ballistic parameter
20	AREAZ (m^2)	Meteoroid cross sectional area
21	RZERO (m)	Line source blast wave radius
22	DVDT (m/s^2)	Meteoroid deceleration
23	KE (J)	Meteoroid kinetic energy
24	DEKDT (W)	Change in meteoroid kinetic energy per unit time

B.2.2 TPFM Physical Concepts

For each simulated fireball event, the initial velocity, entry angle, and initial kinetic energy were taken from the published online JPL dataset. The simulations allowed the fireball energy to vary by up to a factor of two compared to the JPL-reported value following the theoretical arguments about variation in luminous efficiency in Nemtchinov et al. (1997). This distribution was assumed to be uniform. Based on this range of kinetic energy and our known velocity, the corresponding mass range was computed. The simulations had porosity variations from 0 - 95% (uniformly and randomly distributed) to cover all possible types of meteoroids, except for the Tagish Lake meteorite/fireball, where we used 40 - 95% porosity, the lower limit determined from the recovered meteorites (Hildebrand et al., 2005). The initial radius was computed using an assumed grain density of 3500 kg/m^3 together with the previously chosen porosity and mass as estimated from the Monte Carlo energy and known velocity. These initial parameters were then used as input to the TPFM model. The full range explored in these parameters for our five calibration fireball events are shown in Table B.2. A similar process was used for the remaining 18 fireballs we later simulated, except, of course, in those cases no light curves are available.

For each of the five calibration fireballs, we simulated 1000 runs based on the initial parameters given in Table B.2. We then down selected to only model runs that match our observational constraints: namely simulations which have peak energy deposition within 3 km of the observed height at peak brightness (Fig. B.2(a)), are within factor of two of the total reported energy (Fig. B.2(b)) and show a peak magnitude which correlates with the total energy as given in Fig. 4.3 in Chapter 4. The resulting range of parameters is summarized in Table B.3.

Table B.6: Summary of initial parameters used in TPFM model for five calibration fireball events. For the remaining 18 fireballs simulated later the same generic parameters/ranges were used as starting points in the simulation (i.e. shape factor, amount of kinetic energy remaining at the end of the simulation, type of atmosphere, wake mode, porosity range and allowable number of fragments) while the event specific data (energy, velocity, height at peak brightness) are extracted from the JPL fireball table. The range of energy, porosity, strength, and number of fragments are generated randomly and are uniformly distributed within the given range.

	Marshall	Tagish Lake	Park Forest	Antarctica	Tajikistan
Total energy (kT)	30	2.4	0.41	13	0.36
Energy range (kT)	15-60	1.2-4.8	0.25-1.0	6.5-26	0.18-0.72
Velocity (km/s)	24.5	15.8	19.5	13	14.3
Entry angle (°E)	45.4	17.8	61	41.9	80
Height at peak brightness (km)	21	32	29	25	35
Porosity (%)	0 - 95	40 - 95	0 - 95	0 - 95	0 - 95
Strength (MPa)	0.001-0.73	0.005-0.24	0.006-0.30	0.0005-0.12	0.006-0.15
# of fragments	1 - 1024				
Shape factor	1.209 (Sphere)				
Amount of E_k remaining at end height	1%				
Atmosphere	Non-isothermal				
Wake mode	Collective wake				

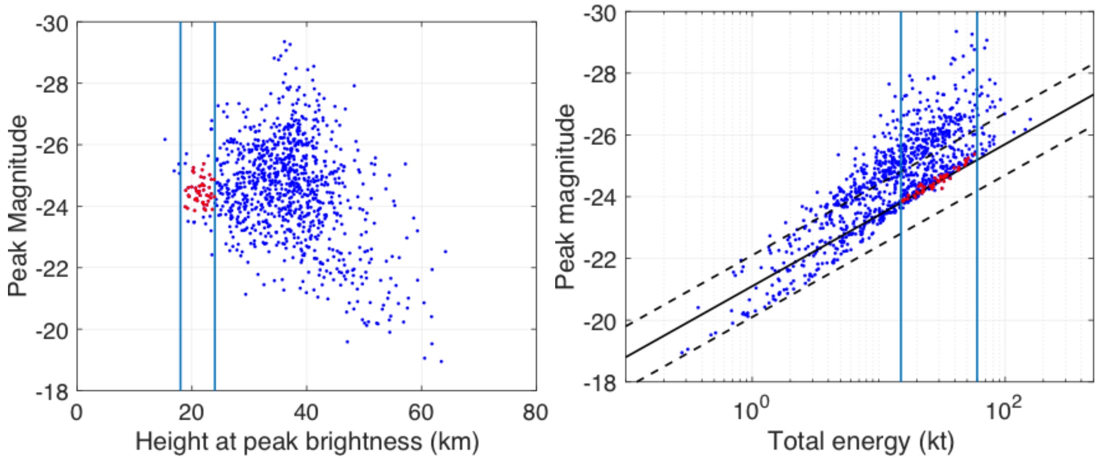

(a) (b)

Figure B.2: An example of TPFM runs that are filtered according to the observational constraints for the Marshall Islands fireball. Blue circles are our 1000 simulated runs based on the initial parameters from Table B.6 while red circles are those runs filtered to match our observational constraints. The blue vertical solid lines show the range used for the observational constraints: (a) for the height at peak brightness of 18 - 24 km (nominal of 21 +/- 3 km) and (b) the total energy range of 15 - 60 kT (nominal 30 kT). The black diagonal solid and dashed lines are the regression fit and the 2σ prediction intervals from the population as a whole for the correlation of peak brightness with total energy (Brown et al., 2016), as shown in Chapter 4 as Fig. 4.3.

Table B.7: The range of parameters for the TPFM model runs which produce light curves that match our observational constraints and the empirical relations as described in the text. The uncertainty in speed and entry angle was taken from the associated reference shown in Chapter 4 as Table 4.1. Later, for the 18 JPL events (E > 2 kT), an uncertainty in speed of 0.5 km/s and uncertainty in entry angle of 1.0° were used. Compare to the full range of explored parameter space shown in Table B.6.

	Marshall	Tagish Lake	Park Forest	Antarctica	Tajikistan
Velocity (km/s)	21.5 - 26.7	14.6 - 16.9	18.7 - 20.1	12.8 - 13.3	12.8 - 15.8
Entry angle (°E)	43.9 - 47.7	14.6 - 21.9	26.4 - 31.7	40.0 - 44.0	76.7 - 82.7
Porosity (%)	2 - 55	40 - 75	1 - 67	1 - 71	1 - 83
Strength (MPa)	0.001 - 0.66	0.03 - 0.18	0.07 - 0.30	0.008 - 0.12	0.006 - 0.09
# of fragments	1 - 4	4 - 1024	2 - 1024	1 - 1024	4 - 1024

B.3 Conversion from the Light Curve to Energy Deposition Curve

For our five calibration fireball events, the raw data for the optical light curve was extracted from published figures in the references shown in Table 4.1 in Chapter 4 and converted to energy deposition using following process:

1. Convert the power digitized from the light curve to the energy per unit length:

$$E_l = \frac{4\pi P}{v} \tag{B.1}$$

where E_l is the optical energy per unit trail length (J/m), P is the power (W/ster), and v is the velocity (m/s).

2. Compute the total impact energy per unit length by dividing the optical energy per unit length by the energy efficiency, τ (Brown et al., 2002a):

$$\tau = (0.1212 \pm 0.0043) E_o^{0.115 \pm 0.075} \tag{B.2}$$

where E_o is the total optical radiant energy in kT (1 kT = 4.185×10^{12} J) provided from the JPL fireball dataset.

3. Calculate the total impact energy per unit height (J/m) by dividing the total impact energy per unit length (J/m) by the sine of the meteoroid entry angle.

The raw data of digitized light curve [time (sec) vs. power (W/ster)] and energy deposition curve [time(sec) vs. energy per unit height (kT/km)] for these five calibration events can be found here. More details concerning the instruments and analysis process can be found in Tagliaferri et al. (1994); Brown et al. (1995), Nemtchinov et al. (1997) and references therein.

B.4 Details of the TPFM and the Weak Shock Model Results for Calibration Events

We present detailed plots showing our filtered model runs for all five calibration fireball events. These detailed model solutions are our primary means of validating our generic approach to estimating the energy deposition as a function of height for our complete suite of fireballs (where light curves are generally not available).

B.4.1 The Marshall Islands Fireball

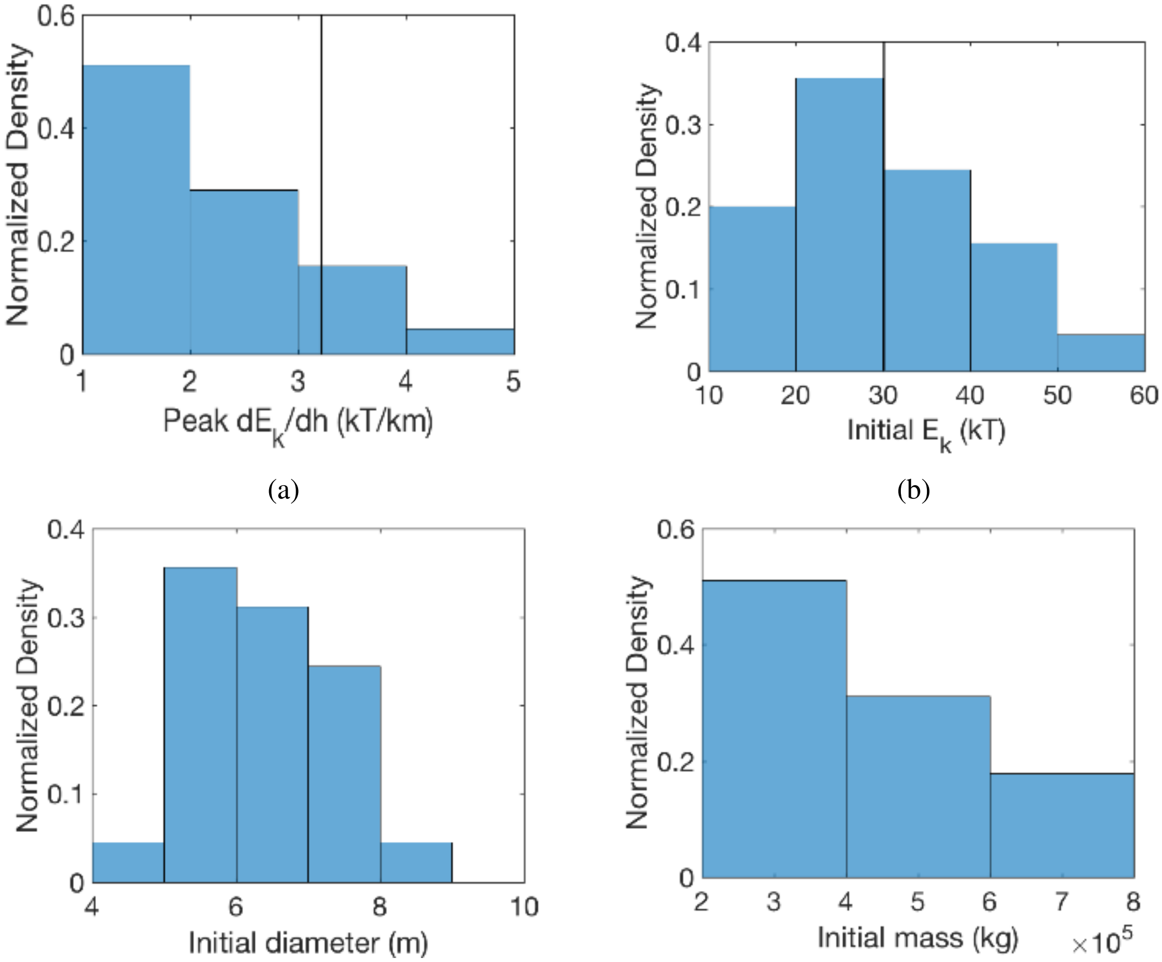

(a) (b)

(c) (d)

Figure B.3: (a-d) Histograms showing the distribution of filtered TPFM model runs for 4 different parameters: (a) peak energy deposition per unit height, (b) initial kinetic energy, (c) initial diameter, and (d) initial mass. The vertical solid line corresponds to the observed quantity. The average of the peak energy deposition for the simulated runs is 2.1 kT/km and the observed peak energy deposition is 3.1 kT/km. The average of the initial kinetic energy for the ensemble of filtered model runs of (29.98 kT) was in a good agreement with the estimated JPL initial kinetic energy, (30 kT).

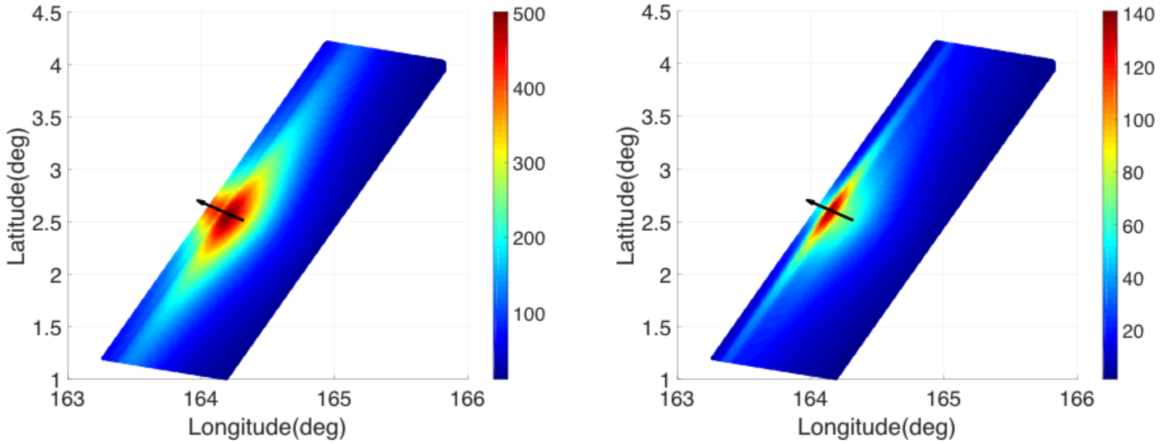

(e)

(f)

Figure B.3: (e-f) The resulting overpressure predicted by the weak shock model based on the energy deposition curves produced from the filtered TPFM models. Shown are the median (e) and standard deviation (f) of the weak shock overpressure (Pa) for the Marshall Islands fireball. The arrow represents the bolide trajectory from 60 km to 10 km altitude moving northwest.

B.4.2 The Tagish Lake Fireball

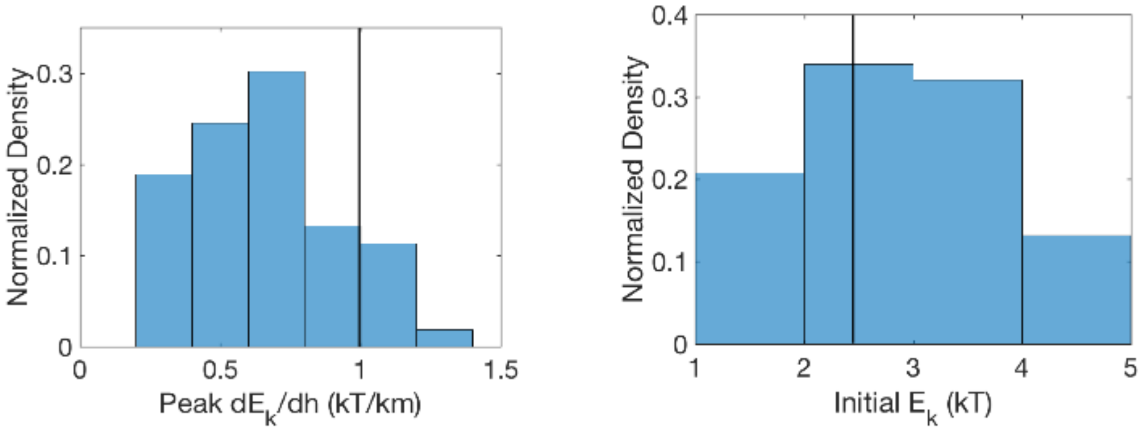

(a)

(b)

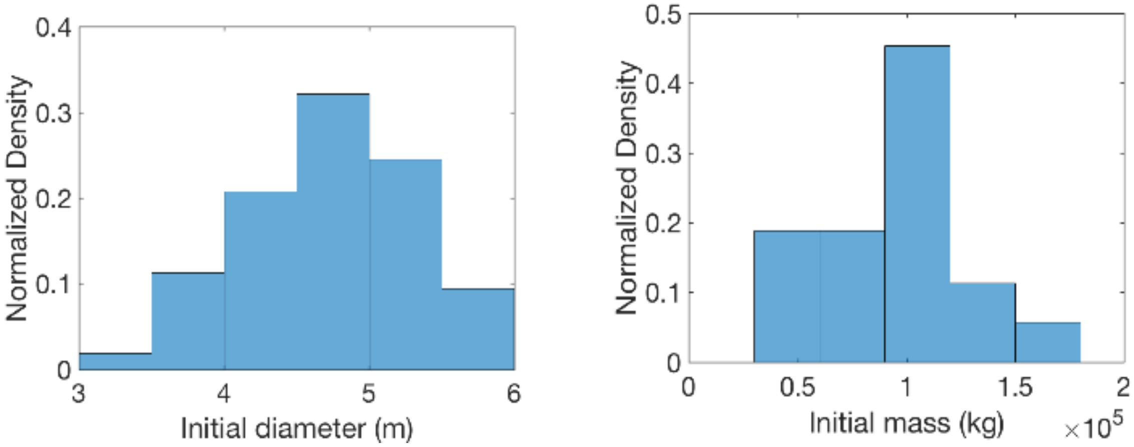

(c) (d)

Figure B.4: (a-d) Histograms showing the distribution of TPFM model runs for 4 different parameters: (a) peak energy deposition per unit height, (b) initial kinetic energy, (c) initial diameter, and (d) initial mass. The vertical solid line corresponds to the observed quantity. The average of the peak energy deposition per unit height for the simulated runs is 0.7 kT/km and the observed peak energy deposition is 1kT/km. The average of model runs of initial kinetic energy is 2.8 kT and the estimated JPL initial kinetic energy is 2.4 kT.

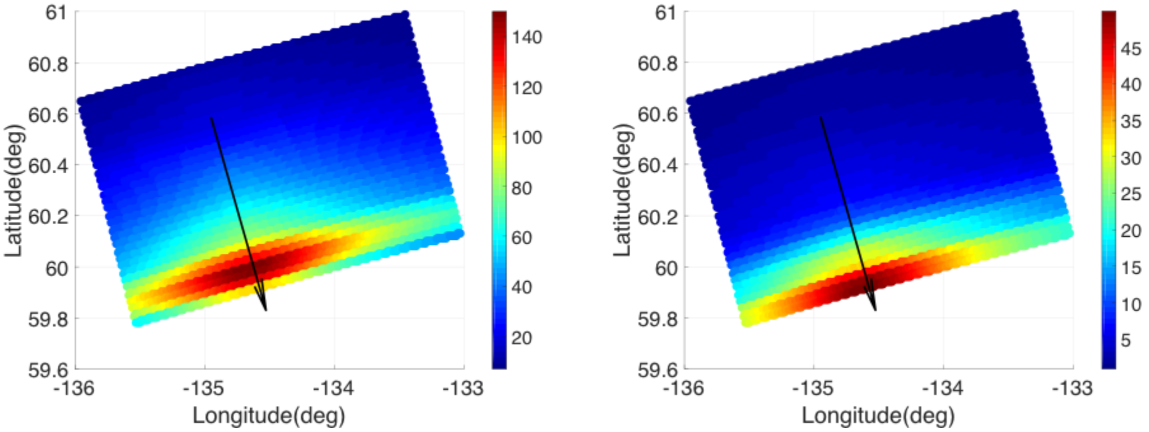

(e) (f)

Figure B.4: (e-f) The result of weak shock modeling showing the median (e) and standard deviation (f) of weak shock overpressure (Pa) for the Tagish Lake fireball. The arrow represents the bolide trajectory from 60 km to 29 km moving southeast.

B.4.3 The Park Forest Fireball

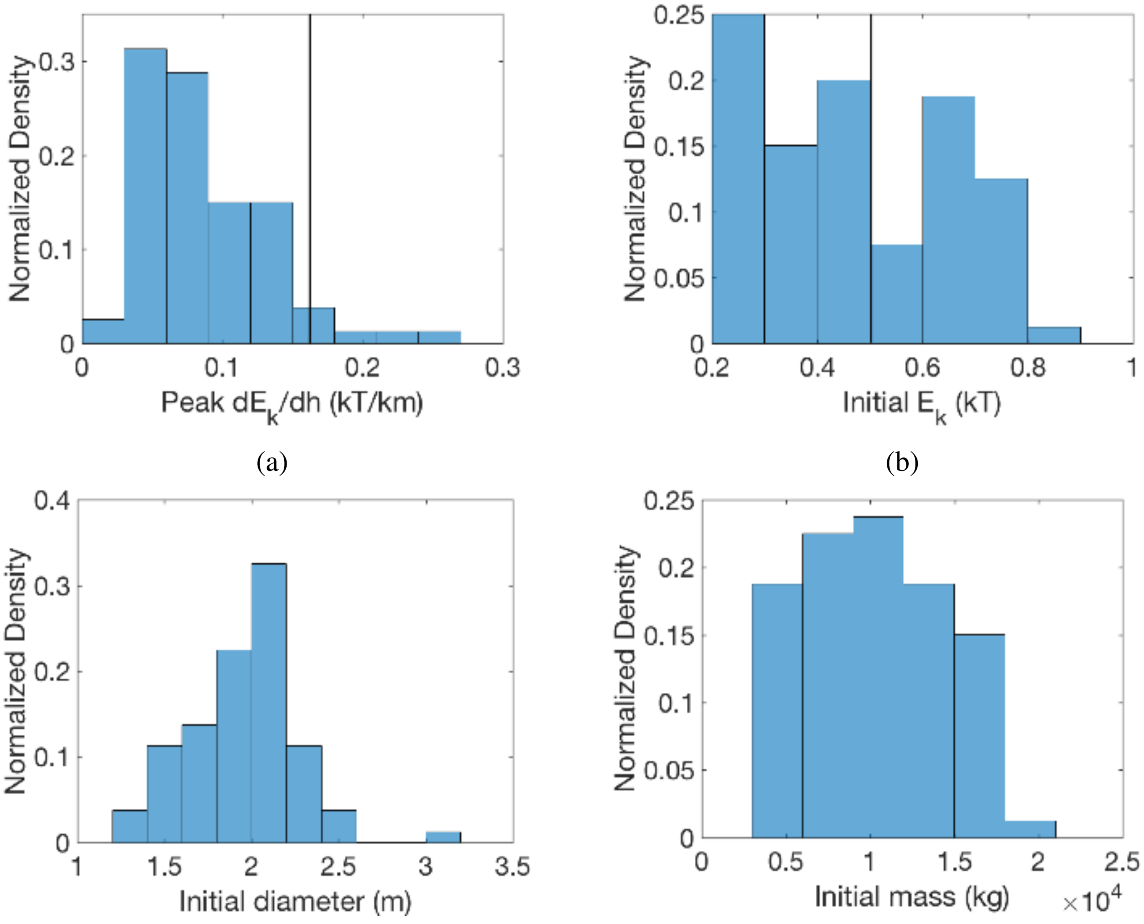

(a) (b)

(c) (d)

Figure B.5: (a-d) Histograms showing the distribution of TPFM model runs for 4 different parameters: (a) peak energy deposition per unit height, (b) initial kinetic energy, (c) initial diameter, and (d) initial mass. The vertical solid line corresponds to the observed quantity. The average of the peak energy deposition per unit height for the simulated runs is 0.087 kT/km and the observed peak energy deposition is 0.17 kT/km. The average of model runs of initial kinetic energy is 0.47 kT and the estimated JPL kinetic energy is 0.41 kT.

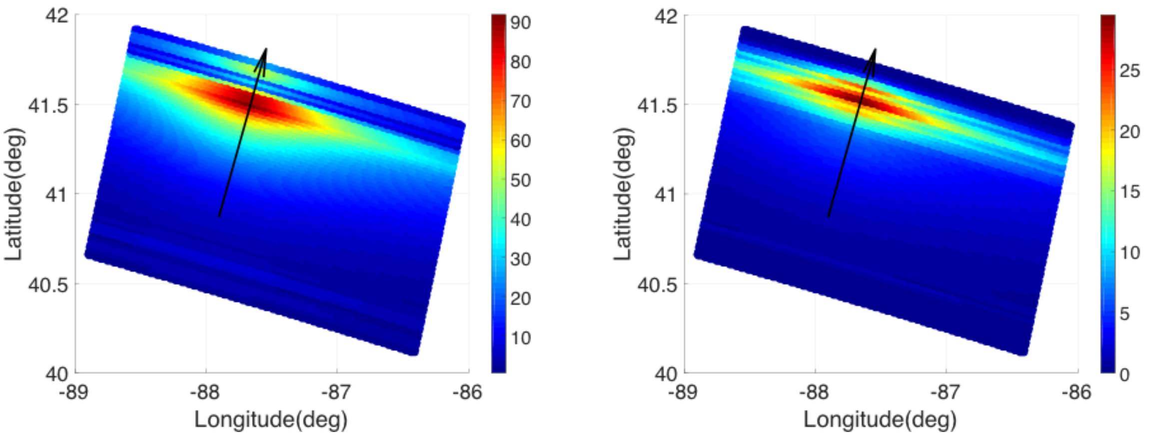

(e)

(f)

Figure B.5: (e-f) The result of weak shock model showing the median (e) and standard deviation (f) of weak shock overpressure (Pa) for the Park Forest fireball. The arrow represents the bolide trajectory from an altitude of 80 km to 18 km moving north-northeast.

B.4.4 The Antarctica Fireball

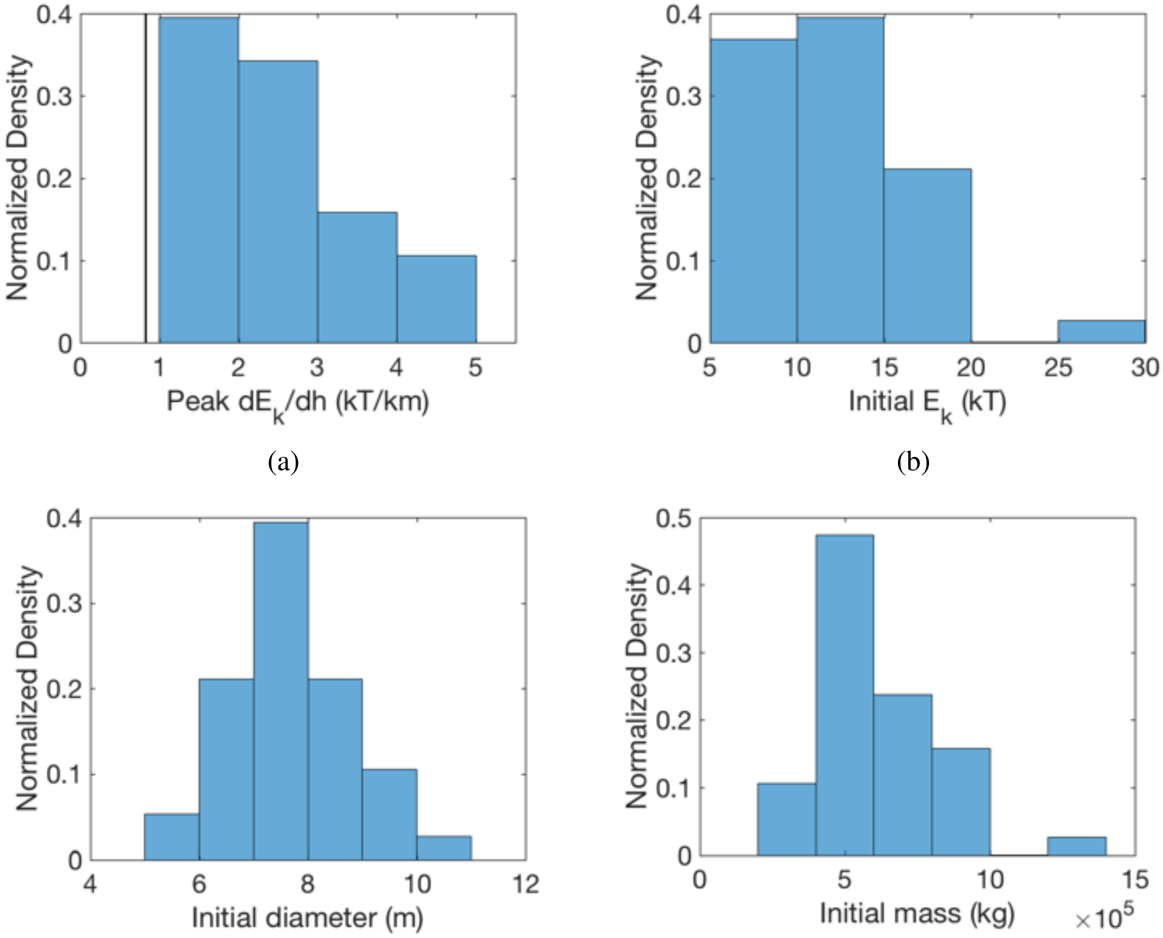

(a)

(b)

(c)

(d)

Figure B.7: (a-d)Histograms showing the distribution of TPFM model runs for 4 different parameters: (a) peak energy deposition per unit height, (b) initial kinetic energy, (c) initial diameter, and (d) initial mass. The vertical solid line corresponds to the observed quantity. The average of the peak energy deposition per unit height for the simulated runs (2.5 kT/km) was not in good agreement with the observed peak energy deposition (0.9 kT/km), as the majority of our simulated runs showed about 4 times larger peak energy deposition than the observation. The average of model runs of initial kinetic energy is 12.2 kT and the estimated JPL kinetic energy is 13 kT.

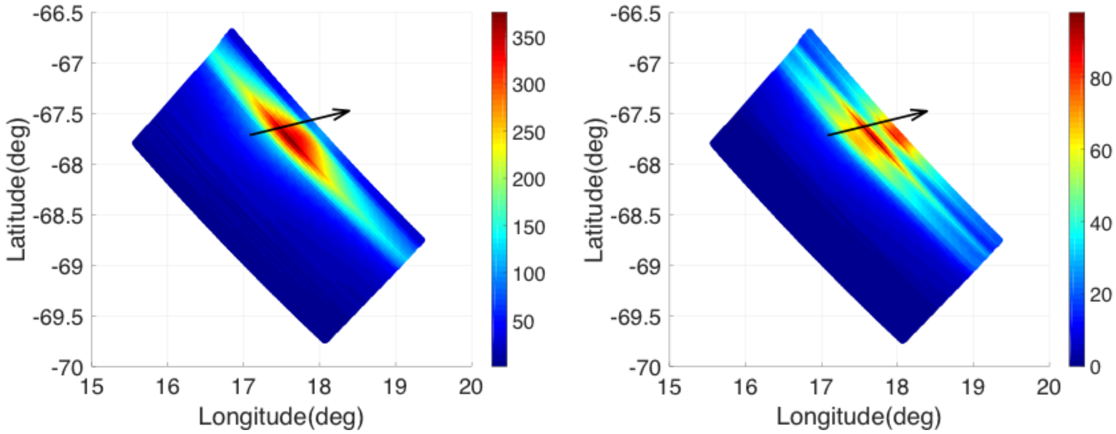

(a) (b)

Figure B.7: (e-f) The result of weak shock model showing the median (f) and standard deviation (g) of weak shock overpressure (Pa) for the Antarctic fireball. The arrow represents the bolide trajectory from 70 km to 16 km moving east-northeast.

B.4.5 The Tajikistan Superbolide

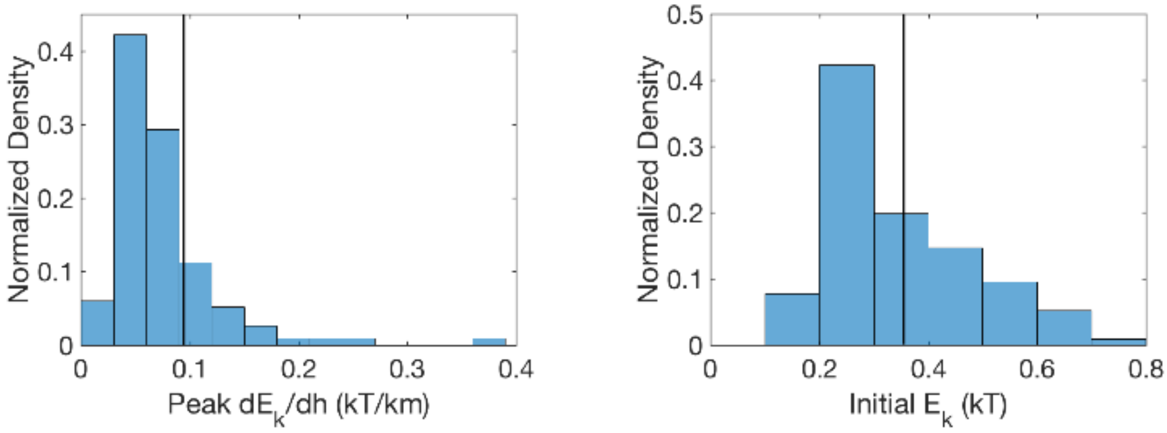

(a) (b)

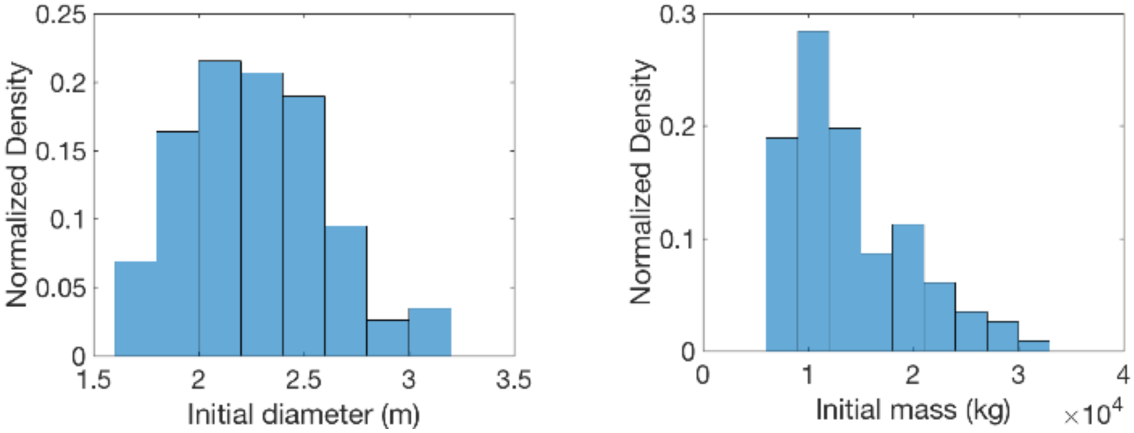

(c) (d)

Figure B.8: (a-d)Histograms showing the distribution of TPFM model runs for 4 different parameters: (a) peak energy deposition per unit height, (b) initial kinetic energy, (c) initial diameter, and (d) initial mass. The vertical solid line corresponds to the observed quantity. The average of the peak energy deposition per unit height for the simulated runs is 0.075 kT/km and the observed peak energy deposition is 0.09 kT/km. The average of model runs of initial kinetic energy is 0.34 kT and the estimated JPL initial kinetic energy is 0.36 kT.

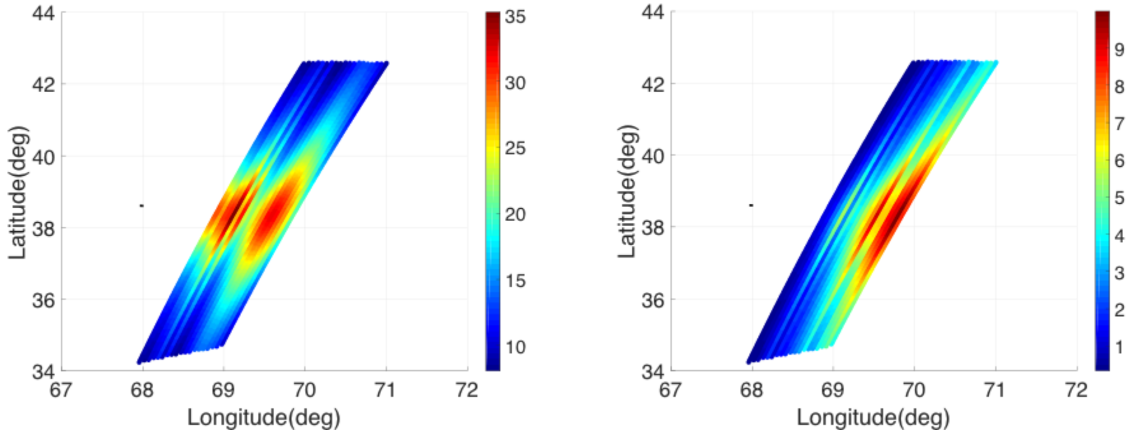

(e) (f)

Figure B.8: (e-f) The result of weak shock model showing the median (e) and standard deviation (f) of weak shock overpressure (Pa) for the Tajikistan superbolide. A short black horizontal line at 38.3N, 68E indicates the bolide trajectory from 38 km to 20 km moving west.

B.5 Weak Shock Model Results for 18 JPL Fireball Events

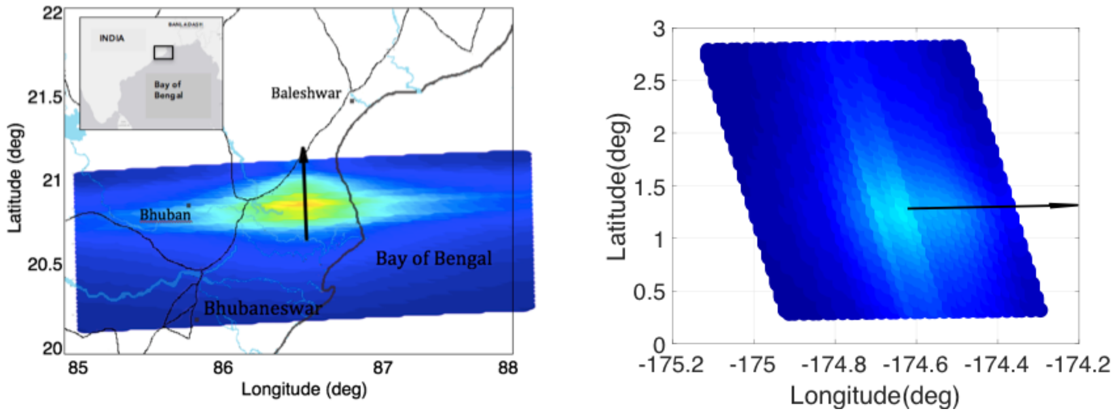

(a) 2003-09-27, India (4.6kT)

(b) 2004-06-05, N. Pacific Ocean (3.9kT)

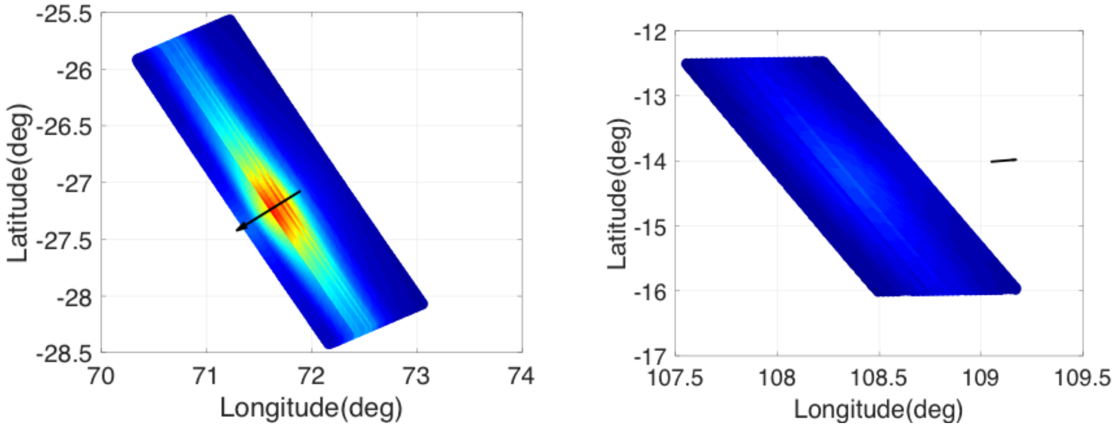

(c) 2004-10-07, Indian Ocean (18kT)

(d) 2006-09-02, Indian Ocean (2.8kT)

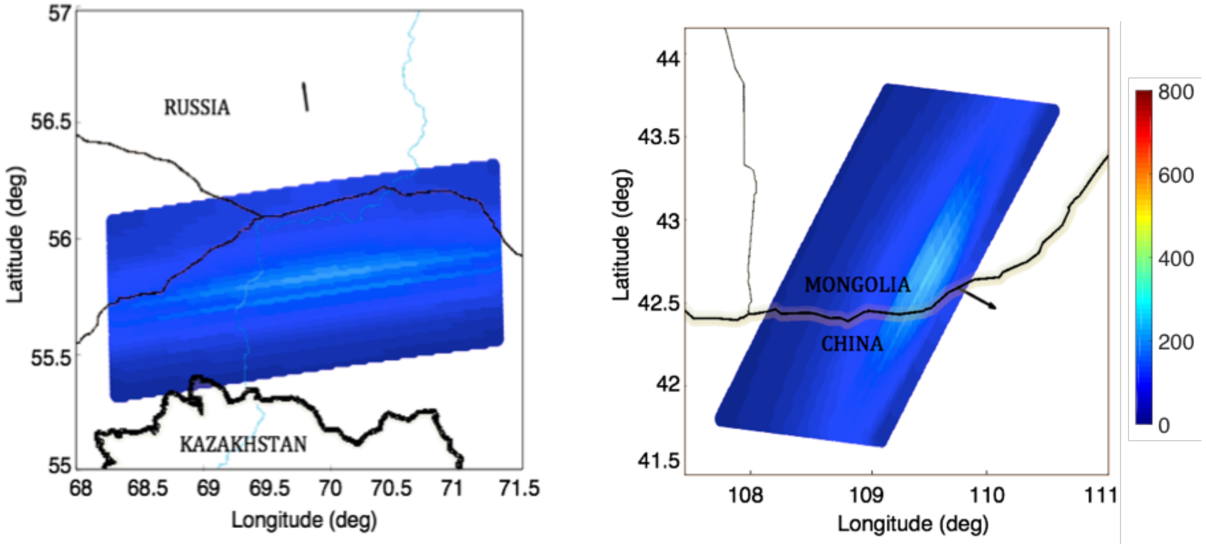

(e) 2009-02-07, Russia (3.5kT)

(f) 2009-09-04, China (2.3kT)

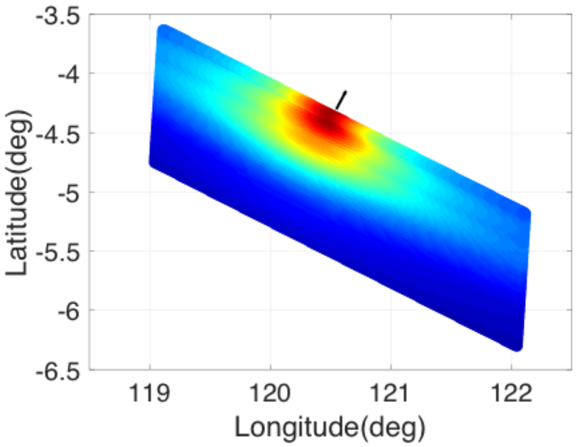

(g) 2009-10-08, Banda Sea (33kT)

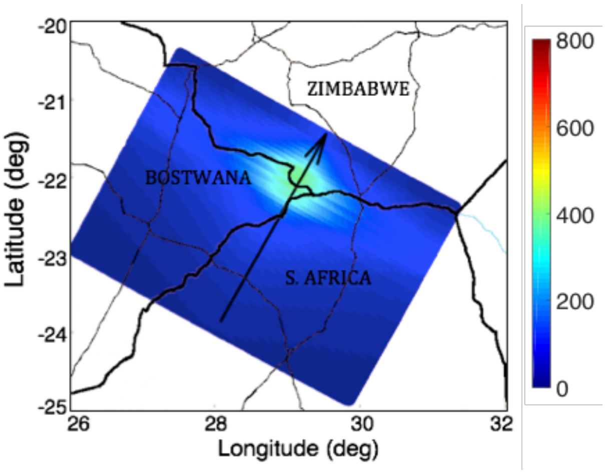

(h) 2009-11-21, Zimbabwe (18kT)

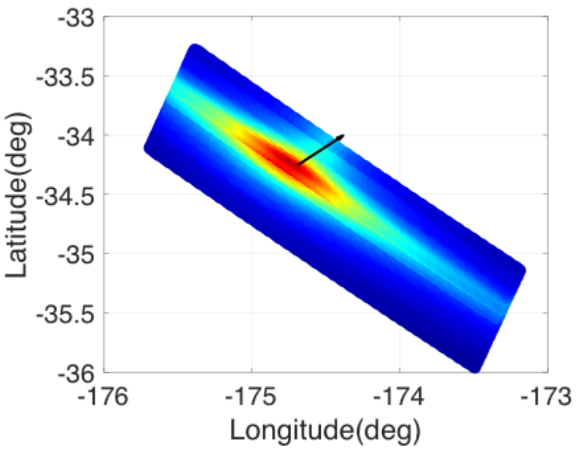

(i) 2010-07-06, S. Pacific Ocean (14kT)

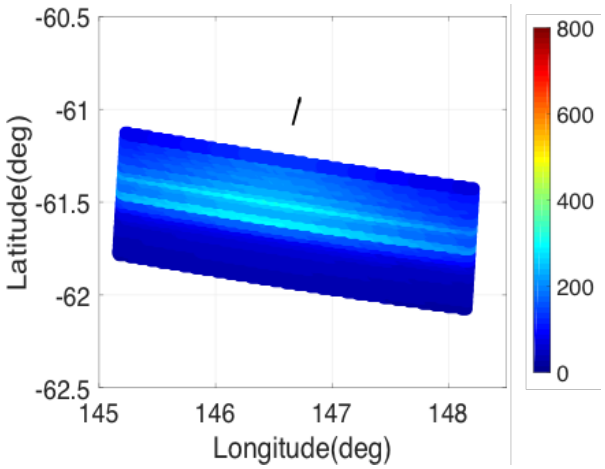

(j) 2010-09-03, Southern Ocean (3.8kT)

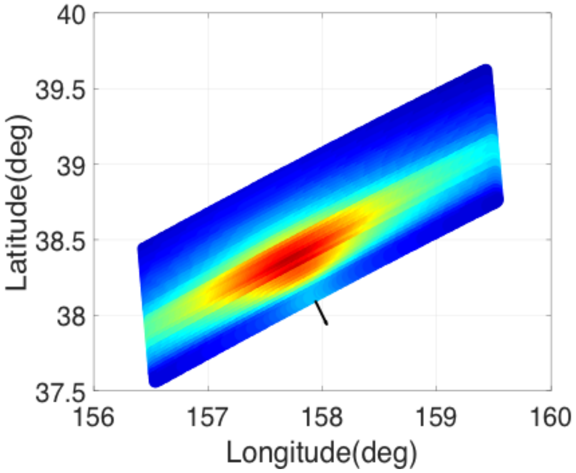

(k) 2010-12-25, N. Pacific Ocean (33kT)

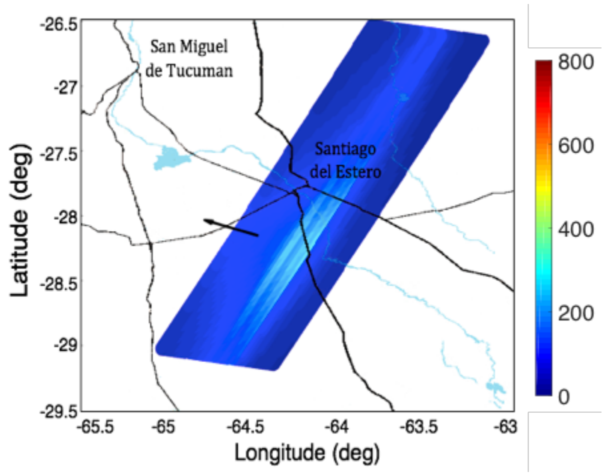

(l) 2013-04-21, Argentina (2.5kT)

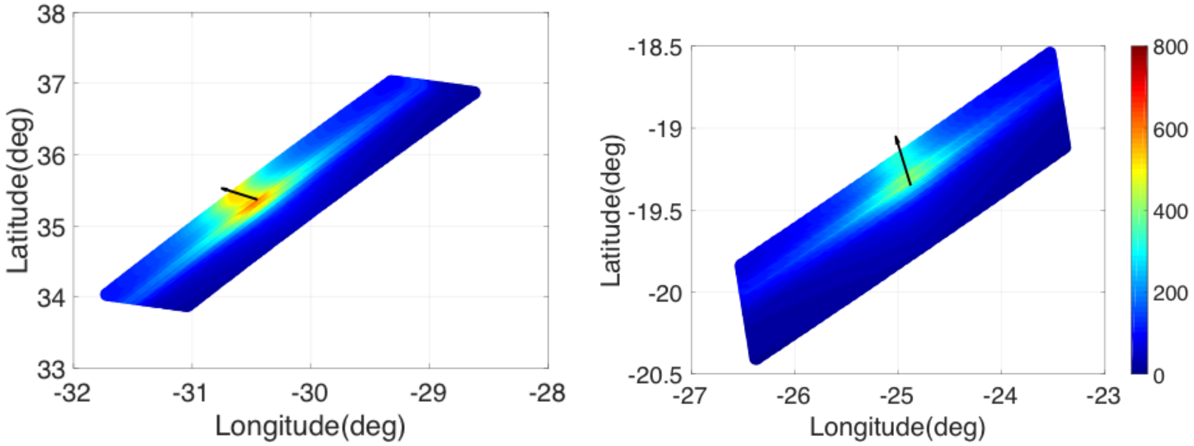

(m) 2013-04-30 , N. Pacific Ocean (10kT)

(n) 2013-10-12, S. Atlantic Ocean (3.5kT)

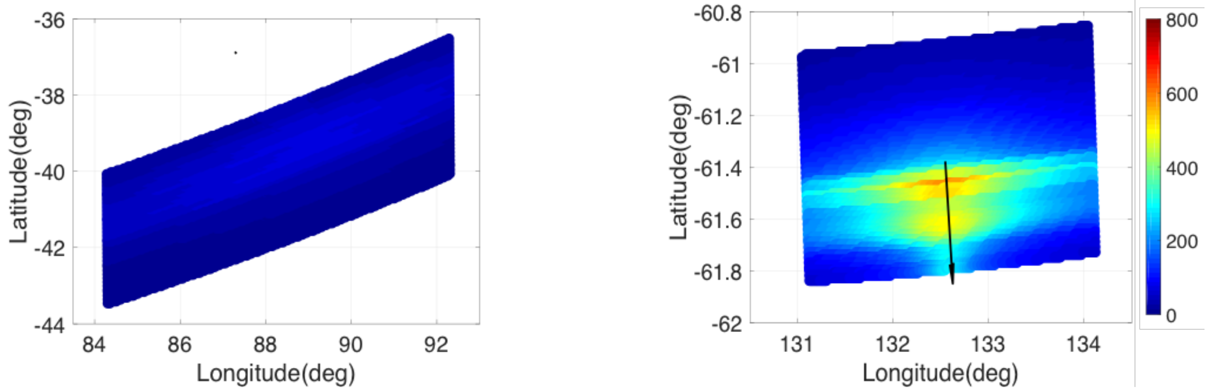

(o) 2014-05-08, Indian Ocean (2.4kT)

(p) 2014-08-23, Southern Ocean (7.6kT)

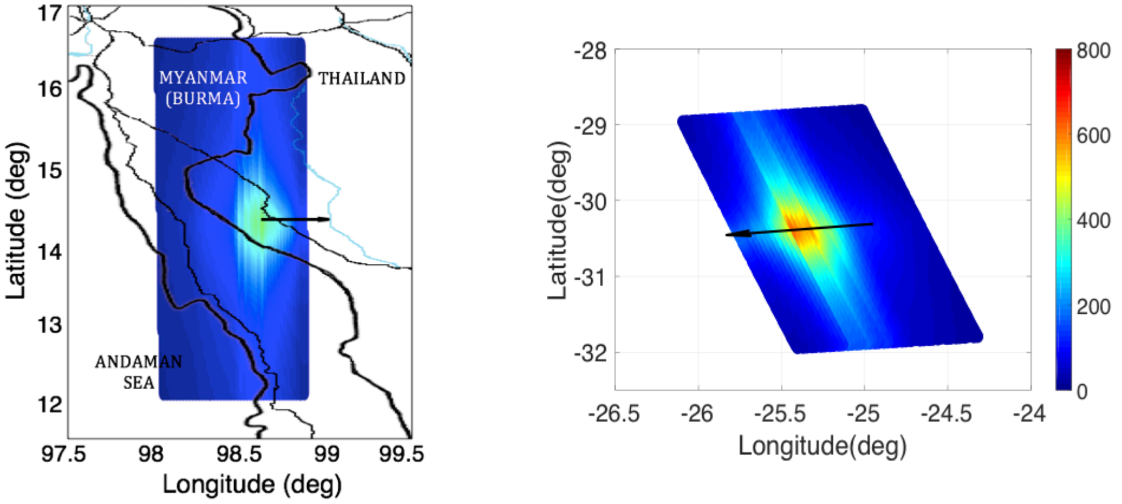

(q) 2015-09-07, Thailand (3.9kT))

(r) 2016-02-06, S. Atlantic Ocean (13kT)

Figure B.9: The result of weak shock model showing the maximum overpressure (Pa) for 18 JPL fireball events. The arrow represents the bolide trajectory. The map was overlaid for the events that occurred over the land. Country border line (thick black line) with major roads/highways (thin black line) and major rivers (blue line) are shown.

Table B.8: Summary of ground-level areas (10^3 km^2) under the fireball where the median and maximum ΔP exceeded the 200 Pa and 500 Pa thresholds for 18 JPL fireball events and 5 calibration events (highlighted in grey). Max. $\Delta P(200)$ of the February 15, 2013 Chelyabinsk fireball (second last row) was computed following our modelling approach based on the energy deposition profile given by Brown et al. (2013), while Max. $\Delta P(500)$ was extracted from Popova et al. (2013).

Date	Height (km)	Energy (kT)	Med. $\delta P(200)$	Med. $\delta P(500)$	Max $\delta P(200)$	Max $\delta P(500)$
1994-02-01	21	30	5.9	0.01	10	1.3
2000-01-08	32	2.4	-	-	1.2	-
2003-03-27	29	0.41	-	-	-	-
2003-09-27	26	4.6	0.95	-	5.4	0.01
2004-06-05	43	3.9	-	-	2	-
2004-09-03	25	13	4.8	-	13	0.51
2004-10-07	35	18	3	-	12	1.2
2006-09-02	44.1	2.8	-	-	-	-
2008-07-23	35	0.36	-	-	-	-
2009-02-07	40	3.5	-	-	0.07	-
2009-09-04	28.3	2.3	-	-	1.5	-
2009-10-08	19.1	33	10	0.01	20	2.5
2009-11-21	38	18	1	-	11	-
2010-07-06	26	14	4.5	-	12	1.7
2010-09-03	33.3	3.8	-	-	6.8	-
2010-12-25	26	33	11	-	19	4.3
2013-04-21	40.7	2.5	-	-	1.8	-
2013-04-30	21.2	10	3.7	0.07	6.9	0.78
2013-10-12	22.2	3.5	1.4	-	2.9	-
2014-05-08	35.4	2.4	-	-	-	-
2014-08-23	22.2	7.6	5.7	-	13	0.49
2015-09-07	29.3	3.9	0.66	-	4.1	-
2016-02-06	31	13	2.5	-	11	0.62
SUM	-	-	55	0.09	155	13
2013-02-15	*29.5*	*500*	-	-	*45*	*19*
TOTAL	-	-	-	-	200	32

ELSEVIER LICENSE
TERMS AND CONDITIONS

Aug 01, 2017

This Agreement between The University of Western Ontario -- Nayeob Gi ("You") and Elsevier ("Elsevier") consists of your license details and the terms and conditions provided by Elsevier and Copyright Clearance Center.

License Number	4159451114805
License date	Jul 31, 2017
Licensed Content Publisher	Elsevier
Licensed Content Publication	Planetary and Space Science
Licensed Content Title	Refinement of bolide characteristics from infrasound measurements
Licensed Content Author	Nayeob Gi, Peter Brown
Licensed Content Date	Available online 29 April 2017
Licensed Content Volume	n/a
Licensed Content Issue	n/a
Licensed Content Pages	1
Start Page	
Type of Use	reuse in a thesis/dissertation
Portion	full article
Format	electronic
Are you the author of this Elsevier article?	Yes

Will you be translating?	No
Title of your thesis/dissertation	Using bolide airwaves to estimate meteoroid source characteristics and window damage potential
Expected completion date	Jul 2017
Estimated size (number of pages)	150
Requestor Location	The University of Western Ontario 1151 Richmond st. London, ON N6A3K7 Canada Attn: The University of Western Ontario
Billing Type	Invoice
Billing Address	The University of Western Ontario 1151 Richmond st. London, ON N6A3K7 Canada Attn: The University of Western Ontario
Total	0.00 CAD

Terms and Conditions

INTRODUCTION

1. The publisher for this copyrighted material is Elsevier. By clicking "accept" in connection with completing this licensing transaction, you agree that the following terms and conditions apply to this transaction (along with the Billing and Payment terms and conditions established by Copyright Clearance Center, Inc. ("CCC"), at the time that you opened your Rightslink account and that are available at any time at http://myaccount.copyright.com).

GENERAL TERMS

2. Elsevier hereby grants you permission to reproduce the aforementioned material subject to the terms and conditions indicated.

3. Acknowledgement: If any part of the material to be used (for example, figures) has appeared in our publication with credit or acknowledgement to another source, permission must also be sought from that source. If such permission is not obtained then that material may not be included in your publication/copies. Suitable acknowledgement to the source must be made, either as a footnote or in a reference list at the end of your publication, as follows:

"Reprinted from Publication title, Vol /edition number, Author(s), Title of article / title of chapter, Pages No., Copyright (Year), with permission from Elsevier [OR APPLICABLE SOCIETY COPYRIGHT OWNER]." Also Lancet special credit - "Reprinted from The

Lancet, Vol. number, Author(s), Title of article, Pages No., Copyright (Year), with permission from Elsevier."
4. Reproduction of this material is confined to the purpose and/or media for which permission is hereby given.

5. Altering/Modifying Material: Not Permitted. However figures and illustrations may be altered/adapted minimally to serve your work. Any other abbreviations, additions, deletions and/or any other alterations shall be made only with prior written authorization of Elsevier Ltd. (Please contact Elsevier at permissions@elsevier.com). No modifications can be made to any Lancet figures/tables and they must be reproduced in full.

6. If the permission fee for the requested use of our material is waived in this instance, please be advised that your future requests for Elsevier materials may attract a fee.

7. Reservation of Rights: Publisher reserves all rights not specifically granted in the combination of (i) the license details provided by you and accepted in the course of this licensing transaction, (ii) these terms and conditions and (iii) CCC's Billing and Payment terms and conditions.

8. License Contingent Upon Payment: While you may exercise the rights licensed immediately upon issuance of the license at the end of the licensing process for the transaction, provided that you have disclosed complete and accurate details of your proposed use, no license is finally effective unless and until full payment is received from you (either by publisher or by CCC) as provided in CCC's Billing and Payment terms and conditions. If full payment is not received on a timely basis, then any license preliminarily granted shall be deemed automatically revoked and shall be void as if never granted. Further, in the event that you breach any of these terms and conditions or any of CCC's Billing and Payment terms and conditions, the license is automatically revoked and shall be void as if never granted. Use of materials as described in a revoked license, as well as any use of the materials beyond the scope of an unrevoked license, may constitute copyright infringement and publisher reserves the right to take any and all action to protect its copyright in the materials.

9. Warranties: Publisher makes no representations or warranties with respect to the licensed material.

10. Indemnity: You hereby indemnify and agree to hold harmless publisher and CCC, and their respective officers, directors, employees and agents, from and against any and all claims arising out of your use of the licensed material other than as specifically authorized pursuant to this license.

11. No Transfer of License: This license is personal to you and may not be sublicensed, assigned, or transferred by you to any other person without publisher's written permission.

12. No Amendment Except in Writing: This license may not be amended except in a writing signed by both parties (or, in the case of publisher, by CCC on publisher's behalf).

13. Objection to Contrary Terms: Publisher hereby objects to any terms contained in any purchase order, acknowledgment, check endorsement or other writing prepared by you, which terms are inconsistent with these terms and conditions or CCC's Billing and Payment terms and conditions. These terms and conditions, together with CCC's Billing and Payment terms and conditions (which are incorporated herein), comprise the entire agreement between you and publisher (and CCC) concerning this licensing transaction. In the event of any conflict between your obligations established by these terms and conditions and those established by CCC's Billing and Payment terms and conditions, these terms and conditions shall control.

14. Revocation: Elsevier or Copyright Clearance Center may deny the permissions described in this License at their sole discretion, for any reason or no reason, with a full refund payable to you. Notice of such denial will be made using the contact information provided by you. Failure to receive such notice will not alter or invalidate the denial. In no event will Elsevier or Copyright Clearance Center be responsible or liable for any costs, expenses or damage incurred by you as a result of a denial of your permission request, other than a refund of the amount(s) paid by you to Elsevier and/or Copyright Clearance Center for denied permissions.

LIMITED LICENSE

The following terms and conditions apply only to specific license types:

15. **Translation**: This permission is granted for non-exclusive world **English** rights only unless your license was granted for translation rights. If you licensed translation rights you may only translate this content into the languages you requested. A professional translator must perform all translations and reproduce the content word for word preserving the integrity of the article.

16. **Posting licensed content on any Website**: The following terms and conditions apply as follows: Licensing material from an Elsevier journal: All content posted to the web site must maintain the copyright information line on the bottom of each image; A hyper-text must be included to the Homepage of the journal from which you are licensing at http://www.sciencedirect.com/science/journal/xxxxx or the Elsevier homepage for books at http://www.elsevier.com; Central Storage: This license does not include permission for a scanned version of the material to be stored in a central repository such as that provided by Heron/XanEdu.
Licensing material from an Elsevier book: A hyper-text link must be included to the Elsevier homepage at http://www.elsevier.com . All content posted to the web site must maintain the copyright information line on the bottom of each image.

Posting licensed content on Electronic reserve: In addition to the above the following clauses are applicable: The web site must be password-protected and made available only to bona fide students registered on a relevant course. This permission is granted for 1 year only. You may obtain a new license for future website posting.

17. **For journal authors:** the following clauses are applicable in addition to the above:
Preprints:
A preprint is an author's own write-up of research results and analysis, it has not been peer-reviewed, nor has it had any other value added to it by a publisher (such as formatting, copyright, technical enhancement etc.).
Authors can share their preprints anywhere at any time. Preprints should not be added to or enhanced in any way in order to appear more like, or to substitute for, the final versions of articles however authors can update their preprints on arXiv or RePEc with their Accepted Author Manuscript (see below).
If accepted for publication, we encourage authors to link from the preprint to their formal publication via its DOI. Millions of researchers have access to the formal publications on ScienceDirect, and so links will help users to find, access, cite and use the best available version. Please note that Cell Press, The Lancet and some society-owned have different preprint policies. Information on these policies is available on the journal homepage.
Accepted Author Manuscripts: An accepted author manuscript is the manuscript of an article that has been accepted for publication and which typically includes author-incorporated changes suggested during submission, peer review and editor-author communications.
Authors can share their accepted author manuscript:

- immediately
  - via their non-commercial person homepage or blog
  - by updating a preprint in arXiv or RePEc with the accepted manuscript
  - via their research institute or institutional repository for internal institutional uses or as part of an invitation-only research collaboration work-group
  - directly by providing copies to their students or to research collaborators for their personal use
  - for private scholarly sharing as part of an invitation-only work group on commercial sites with which Elsevier has an agreement
- After the embargo period
  - via non-commercial hosting platforms such as their institutional repository
  - via commercial sites with which Elsevier has an agreement

In all cases accepted manuscripts should:

- link to the formal publication via its DOI
- bear a CC-BY-NC-ND license - this is easy to do
- if aggregated with other manuscripts, for example in a repository or other site, be shared in alignment with our hosting policy not be added to or enhanced in any way to appear more like, or to substitute for, the published journal article.

Published journal article (JPA): A published journal article (PJA) is the definitive final record of published research that appears or will appear in the journal and embodies all value-adding publishing activities including peer review co-ordination, copy-editing, formatting, (if relevant) pagination and online enrichment.

Policies for sharing publishing journal articles differ for subscription and gold open access articles:
Subscription Articles: If you are an author, please share a link to your article rather than the full-text. Millions of researchers have access to the formal publications on ScienceDirect, and so links will help your users to find, access, cite, and use the best available version.
Theses and dissertations which contain embedded PJAs as part of the formal submission can be posted publicly by the awarding institution with DOI links back to the formal publications on ScienceDirect.
If you are affiliated with a library that subscribes to ScienceDirect you have additional private sharing rights for others' research accessed under that agreement. This includes use for classroom teaching and internal training at the institution (including use in course packs and courseware programs), and inclusion of the article for grant funding purposes.

Gold Open Access Articles: May be shared according to the author-selected end-user license and should contain a CrossMark logo, the end user license, and a DOI link to the formal publication on ScienceDirect.
Please refer to Elsevier's posting policy for further information.

18. **For book authors** the following clauses are applicable in addition to the above: Authors are permitted to place a brief summary of their work online only. You are not allowed to download and post the published electronic version of your chapter, nor may you scan the printed edition to create an electronic version. **Posting to a repository:** Authors are permitted to post a summary of their chapter only in their institution's repository.

19. **Thesis/Dissertation**: If your license is for use in a thesis/dissertation your thesis may be submitted to your institution in either print or electronic form. Should your thesis be published commercially, please reapply for permission. These requirements include permission for the Library and Archives of Canada to supply single copies, on demand, of the complete thesis and include permission for Proquest/UMI to supply single copies, on demand, of the complete thesis. Should your thesis be published commercially, please reapply for permission. Theses and dissertations which contain embedded PJAs as part of the formal submission can be posted publicly by the awarding institution with DOI links back to the formal publications on ScienceDirect.

Elsevier Open Access Terms and Conditions
You can publish open access with Elsevier in hundreds of open access journals or in nearly 2000 established subscription journals that support open access publishing. Permitted third party re-use of these open access articles is defined by the author's choice of Creative Commons user license. See our open access license policy for more information.
Terms & Conditions applicable to all Open Access articles published with Elsevier:
Any reuse of the article must not represent the author as endorsing the adaptation of the article nor should the article be modified in such a way as to damage the author's honour or reputation. If any changes have been made, such changes must be clearly indicated.

The author(s) must be appropriately credited and we ask that you include the end user license and a DOI link to the formal publication on ScienceDirect.
If any part of the material to be used (for example, figures) has appeared in our publication with credit or acknowledgement to another source it is the responsibility of the user to ensure their reuse complies with the terms and conditions determined by the rights holder.
Additional Terms & Conditions applicable to each Creative Commons user license:
CC BY: The CC-BY license allows users to copy, to create extracts, abstracts and new works from the Article, to alter and revise the Article and to make commercial use of the Article (including reuse and/or resale of the Article by commercial entities), provided the user gives appropriate credit (with a link to the formal publication through the relevant DOI), provides a link to the license, indicates if changes were made and the licensor is not represented as endorsing the use made of the work. The full details of the license are available at http://creativecommons.org/licenses/by/4.0.
CC BY NC SA: The CC BY-NC-SA license allows users to copy, to create extracts, abstracts and new works from the Article, to alter and revise the Article, provided this is not done for commercial purposes, and that the user gives appropriate credit (with a link to the formal publication through the relevant DOI), provides a link to the license, indicates if changes were made and the licensor is not represented as endorsing the use made of the work. Further, any new works must be made available on the same conditions. The full details of the license are available at http://creativecommons.org/licenses/by-nc-sa/4.0.
CC BY NC ND: The CC BY-NC-ND license allows users to copy and distribute the Article, provided this is not done for commercial purposes and further does not permit distribution of the Article if it is changed or edited in any way, and provided the user gives appropriate credit (with a link to the formal publication through the relevant DOI), provides a link to the license, and that the licensor is not represented as endorsing the use made of the work. The full details of the license are available at http://creativecommons.org/licenses/by-nc-nd/4.0. Any commercial reuse of Open Access articles published with a CC BY NC SA or CC BY NC ND license requires permission from Elsevier and will be subject to a fee.
Commercial reuse includes:

- Associating advertising with the full text of the Article
- Charging fees for document delivery or access
- Article aggregation
- Systematic distribution via e-mail lists or share buttons

Posting or linking by commercial companies for use by customers of those companies.

20. **Other Conditions**:

v1.9

Questions? customercare@copyright.com or +1-855-239-3415 (toll free in the US) or +1-978-646-2777.

Curriculum Vitae

Name:	Nayeob(Caroline) Gi
Post-Secondary Education and Degrees:	MSc. Geophysics, 2015-2017 The University of Western Ontario London, Ontario
	BSc. Atmospheric Science, 2009-2014 The University of British Columbia Vancouver, British Columbia
Honors and Awards:	NSERC Undergraduate Student Research Award, 2013 President's Entrance Scholarship, 2009
Related Work Experience:	Graduate Teaching Assistant, 2015-2017 The University of Western Ontario London, Ontario
	Research Assistant, 2014-2015 University of New Brunswick Fredericton, New Brunswick
	Undergraduate Research Assistant, 2013-2014 The University of British Columbia Vancouver, British Columbia

Publications:

Gi, N. and Brown, P. (2017) Refinement of Bolide Characteristics from Infrasound measurements, *Planetary and Space Science*. 143:169-181. doi:10.1016/j.pss.2017.04.021.

Gi, N. and Brown, P. (2017) The frequency of window damage caused by bolide airbursts, *Meteoritics* & *Planetary Science*, Manuscript ID: MAPS-2805 (submitted).